Inaugural – Dissertation

submitted to the
Combined Faculties for the Natural Sciences and for Mathematics
of the Ruperto-Carola University of Heidelberg, Germany
for the degree of
Doctor of Natural Sciences

Put forward by
Sebastian Peter Flassbeck, M.Sc.
Born in: Berlin, Germany
Oral examination: Mai 8th, 2019

On the Simultaneous Quantification of Flow Velocities and Relaxation Constants Through Magnetic Resonance Fingerprinting

Referees : Prof. Dr. Peter Bachert
Prof. Dr. Lothar Schad

"That's all it takes really... Pressure and time... That, and big goddamn poster."

The Shawshank Redemption

On the Simultaneous Quantification of Flow Velocities and Relaxation Constants Through Magnetic Resonance Fingerprinting

In this thesis, the development of a novel magnetic resonance imaging (MRI) pulse sequence based on magnetic resonance fingerprinting (MRF) is presented. The proposed technique, termed "Flow-MRF", allows time-resolved velocities and relaxation constants to be quantified simultaneously, in shorter acquisition times than conventional MR-based velocimetry. The simultaneous quantification of both sets of parameters was achieved by formulating the combined problem in the MRF framework. An MRF pattern was designed to create minimal coupling between the relaxometric and velocimetric parameter encoding.

Flow-MRF was validated and tested in simulations, phantom experiments, and an in vivo study targeting the popliteal artery and the gastrocnemius muscle. In each investigation, Flow-MRF quantified relaxation constants and flow velocities in strong agreement with literature and reference measurements. Furthermore, the use of high velocity encoding moments ($\Delta m_1 = 60\,\mathrm{mT/m \cdot ms^2}$) was demonstrated while maintaining a range of correctly quantifiable velocities beyond 800 cm/s. In the volunteer study, Flow-MRF determined an average longitudinal relaxation time of (1384 ± 75) ms and a transverse relaxation time of (26 ± 4) ms in the gastrocnemius muscle. The average velocity deviation over all three volunteers between Flow-MRF and the reference was (-2.6 ± 5.2) cm/s. Lastly, the potential to quantify the complete Reynolds stress tensor with Flow-MRF was investigated and shown in a stenotic flow phantom experiment.

Flow-MRF presents a novel method of quantifying velocities in up to fourfold shorter measurement times than conventional velocity mapping techniques, while simultaneously providing relaxometric maps of static tissue. These improvements can potentially be helpful in the assessment of pathologies such as arteriosclerosis.

Über die simultane Quantifizierung von Strömungsgeschwindigkeiten und Relaxationszeiten mit Hilfe von Magnetic Resonance Fingerprinting

In dieser Arbeit wird die Entwicklung einer neuen magnetresonanztomographischen Bildgebungssequenz basierend auf Magnetic Resonance Fingerprinting (MRF) vorgestellt. Die entwickelte Technik namens „Flow-MRF“ erlaubt die simultane Quantifizierung von zeitaufgelösten Strömungsgeschwindigkeiten und Relaxationszeiten in verkürzter Messdauer verglichen zu konventioneller, MR-basierter Geschwindigkeitsquantifizierung. Durch die Formulierung des kombinierten Quantifizierungsproblems im Rahmen des MRF-Konzepts wurde die gleichzeitige Bestimmung beider Parameter ermöglicht. Dafür wurde ein MRF-Muster entworfen, welches eine minimale Kopplung zwischen der Kodierung der Geschwindigkeiten und den relaxometrischen Parametern verursacht.
Flow-MRF wurde in Simulationen, Phantom-Experimenten und in einer In Vivo Studie, zur Untersuchung der Kniekehlarterie und des zweibäuchigen Wadenmuskels, getestet. Alle Untersuchungen zeigen eine hohe Übereinstimmung der mit Flow-MRF quantifizierten Geschwindigkeiten und Relaxationszeiten mit Literaturwerten und Referenzmessungen. Des Weiteren wurde die Kodierung der Geschwindigkeit mit hohen Momenten ($\Delta m_1 = 60\,\mathrm{mT/m \cdot ms^2}$) demonstriert und der Bereich der korrekt quantifizierbaren Geschwindigkeiten auf über 800 cm/s bestimmt. In der Probandenstudie wurde im Wadenmuskel eine longitudinale Relaxationszeit von (1384 ± 75) ms und eine transversale Relaxationszeit von (26 ± 4) ms bestimmt. Die mittlere Abweichung der bestimmten Geschwindigkeiten über alle Probanden zwischen Flow-MRF und der Referenz beträgt (-2.6 ± 5.2) cm/s. Schließlich wurde die Möglichkeit, mit Flow-MRF den vollständigen Reynoldsschen Spannungstensors zu quantifizieren, in einer Messung mit stenotischen Fließbedingungen untersucht und gezeigt.
Flow-MRF stellt eine neue Methode zur simultanen Quantifizierung von Strömungsgeschwindigkeiten dar und ermöglicht dabei eine bis vierfach verkürzte Messdauer als konventionelle Methoden. Zusätzlich werden bei Flow-MRF die Relaxationszeiten von statischem Gewebe bestimmt. Diese Neuerungen sind potenziell hilfreich bei der Untersuchung von Pathologien wie Arteriosklerose.

Contents

1 Introduction

Medical imaging has become a cornerstone of medical diagnostics in the last decades. Among all medical imaging modalities, MRI holds a unique list of benefits: an excellent soft tissue contrast, insight into physiological processes, and highly resolved spatiotemporal morphology, to name a few, while avoiding any exposure to ionizing radiation. These characteristics qualify MRI based diagnostics as the medical imaging modality of choice in many clinical questions. The majority of the clinical MR images, however, are qualitative in their contrast, unlike many other imaging modalities. No quantitative value can be assigned to each voxel in the final image, despite the inherently quantitative amplitude of the MR signal, due to multitude of scaling factors during the acquisition, digitization, and reconstruction.

The qualitative or weighted images do not represent a prohibitive drawback in current radiology because the diagnosis is based on the expertise and knowledge of highly trained physicians capable of coping with varying contrast and signal levels. The steadily increasing number of MRI examinations over the last decade in Germany (185 %-fold increase) [1], however, might indicate that in the future, the radiologists might need to be assisted by automated diagnostic tools based on machine learning techniques. These techniques thrive on consistent and quantitative input data. Furthermore, ever-larger multi-center studies can strongly benefit from consistent imaging parameters and identical imaging hardware. This, however, is often not feasible due to different coil availability, varying gradient hardware or even different MRI-vendors. Truly quantitative imaging would immediately alleviate all problems of inter-site variability as the fundamental properties of the biological sample are measured. Large databases of normal and abnormal relaxation times, for example, could provide the basis for radiological reporting systems, allowing comprehensible, standardized and objective evaluations of the MRI data. The potential advantages of these reporting systems have been successfully demonstrated by the Prostate Imaging Reporting and Data System (PI-RADS), for example [2].

The quantification of relaxometric constants can provide an optimal image contrast compared to weighted images, and allow synthetic images with pure contrast to be generated. Many fast imaging sequences generate mixed contrasts based on both T_1 and T_2. Disfavorable combinations of these parameters can result in low contrast as can be seen in fluid-attenuated inversion recovery (FLAIR) sequences at 7 T [3].

The native T_2-FLAIR contrast is up to twofold lower at 7 T than at 1.5 T [3], largely negating the advantage of the higher signal. The inhomogeneity of the transmit field poses one of the major challenges at main magnetic fields of 7 T and above [4]. Relaxometric mapping inherently eliminates the variability in the image signal caused by the inhomogeneous transmit field, because the underlying physical properties of the tissue are displayed. This does not mean that transmit variability has no influence on quantitative methods, but its variation can be estimated alongside the relaxometric parameters [5, 6] or be included in the mapping process as prior knowledge.
The increasing need and performance of automated medical image processing, alongside the increasing availability of ultra high-field MRI systems, creates a higher necessity for quantitative imaging than ever.

Magnetic Resonance Fingerprinting (MRF) [7] is a promising technique capable of achieving rapid quantification of tissue parameters, mainly relaxation constants, in clinically feasible timescales. This can be realized by a highly undersampled acquisition of the temporal signal behavior in non-steady state conditions. It was shown that this transient signal evolution can provide quantitative information on T_1, T_2, B_0, B_1, and others [7, 6, 8, 9]. The set of quantifiable parameters is dependent on the choice of MRF pattern, i.e., the excitation, gradients, and timing pattern.
The temporal evolution of the signal inherently encodes the information of multiple parameters *simultaneously*. Conventionally, the quantification of MR measurable parameters is performed sequentially, as in DESPOT 1 & 2 [10], for example. The acquisition time, however, is limited by the time needed to encode each parameter. This encoding process includes the spatial encoding but also time needed to prepare the signal, such as the inversion time in inversion recovery experiments. In MRF, the problem of sequential encoding is transferred to a problem of separability or informational decoding. Every parameter needs to have a unique temporal influence on the measured signal for it to be quantifiable with MRF. The separability problem has tremendous benefits in multi-parameter quantification as, in theory, increasing the number of quantified parameters does not necessarily reduce the fidelity with which every other parameter is determined. In a sequential encoding scheme time dedicated to the quantification of every other parameter needs to be reduced, to make time of the additionally measured quantities. A reduction in the time invested for each parameter must result in a decrease of their fidelity, assuming no idle time is wasted in the respective sequences. Augmenting the number of simultaneously quantified parameters, inevitability increases the efficiency of MRF compared to sequential encoding schemes, as long as a good separability between parameters is given. These assessments motivate the observations presented within this work, where the additional quantification of flow velocities alongside the established relaxometric parameters has nearly no negative influence for the determination of other parameter

within the same measurement time. This effect can be ascribed to the conscious design of an MRF sequence where the influences of the velocity quantification on the relaxometry, and vice versa, are minimized.

The time-resolved quantification of flow velocities is used in clinical routines in investigating a multitude of cardiovascular diseases [11]. These sequences, however, are inherently limited by long acquisition times, constraining their application to single slices or low spatial or temporal resolutions. The phase-based quantification sets an upper bound on the quantifiable velocities due to the 2π dynamic range. An estimate of the expected maximum velocity has to be made before the measurement to determine the amplitude of the velocity encoding moments. A smaller velocity encoding moment increases the quantifiable range of velocities but at the cost of an increased velocity noise. The encountered velocities in patients can exceed those of healthy volunteers many-fold [12]. This usually enforces a large overestimation of the maximum velocity, in turn reducing the efficiency of the measurement. The MRF based quantification aims to tackle the long acquisitions times and the limited range of quantifiable velocities while using velocity encoding moments largely exceeding those of conventional velocimetry.

The simultaneous measurement of flow velocities and relaxometric parameters is especially interesting for the diagnosis and treatment of diseases such as arteriosclerosis, where plaque builds up inside of an artery. It is known that severe cases of atherosclerosis can result in coronary artery disease, stroke, and other cardiovascular problems [13]. Likewise, the diagnostic value of T_1 and T_2 weighted contrasts in the characterization of plaque was established [14]. The flow information is helpful in determining the severity of the stenosis [15] and allows the determination of the forces acting on the plaque [16]. Simultaneously acquiring quantitative information on all of these parameters, in a competitive measurement time with conventional sequences, could provide high diagnostic value. This prospect, at heart, is driving the development of the presented techniques in this work.

2 Theory

2.1 Nuclear Magnetic Resonance

2.1.1 Nuclear Spin and Macroscopic Magnetization

Every nucleon, the building blocks of all atoms, inherently posse a quantized angular momentum, called nuclear spin. The existence of quantized angular momentum was first observed by Stern and Gerlach in 1922 [17]. The fundamental nucleonic property of spin can persist in atoms, given the vector sum of all spins in the nucleus does not cancel out. A finite total angular momentum $\vec{J}$ gives rise to a magnetic moment $\vec{\mu}$, linked by the following equation:

$$\hat{\vec{\mu}} = \gamma \hat{\vec{J}}, \tag{2.1}$$

with γ the gyromagnetic ratio, a nucleus-specific constant and which can be expressed in the following manner:

$$\gamma = g\frac{\mu_K}{\hbar} \quad \text{with} \quad \mu_K = \frac{q}{2m_r}\hbar. \tag{2.2}$$

Here, g is the Landé g-factor, μ_k the nuclear magneton and $\hbar$ the reduced Plank constant. For the ${}^1_1\mathrm{H}$ hydrogen nucleus, γ is determined as $267.522 \cdot 10^6$ rad/sT.

For the angular momentum operator $\hat{\vec{J}}$ the following eigenvalue equations and commutator relations are valid:

$$\hat{\vec{J}}^2 \left|j, m\right\rangle = \hbar^2 j(j+1) \left|j, m\right\rangle \tag{2.3}$$

$$\hat{J}_z = m\hbar \left|j, m\right\rangle . \tag{2.4}$$

$$\left[\hat{J}_a, \hat{J}_b\right] = i\epsilon_{abc}\hbar\hat{J}_c \tag{2.5}$$

$$\left[\hat{J}_a, \hat{\vec{J}}^2\right] = 0 \tag{2.6}$$

Here, $|j, m\rangle$ is the angular momentum state vector with j and m the primary and secondary spin quantum numbers. The vanishing commutator between $\hat{\vec{J}}^2$ and any

component of $\hat{\vec{J}}$ means that both the absolute value and one direction of the angular momentum (usually chosen to be $\hat{J}_z$) can be simultaneously measured. In general, j can take integer or half-integer values, while m may be any of the $2j+1$ values between $-j, j+1, ..., j-1, j$. For the ${}^1_1$H hydrogen nucleus, consisting of a single proton, $j = \frac{1}{2}$ and m may take on two possible values.
The application of an external magnetic field $\vec{B}$ leads to an energy interaction, called Zeeman effect, which can be described by the following Hamilton operator:

$$\hat{\mathcal{H}} = -\hat{\vec{\mu}} \cdot \vec{B}. \tag{2.7}$$

Assuming, without loss of generality, the $\vec{B}$ field along the z-direction yields:

$$\hat{\mathcal{H}} = -\gamma \hbar B_0 \hat{J}_z \tag{2.8}$$

This equation shows that $\hat{\mathcal{H}}$ is equal to $\hat{J}_z$ save the scalar factor γB_0. The eigenstates of the Hamiltonian are thus the eigenstates of $\hat{J}_z$ scaled by the previous factor. The allowed energies, according to the time-independent Schrödinger equation, therefore are:

$$E_m = -\gamma \hbar B_0 m \quad m = -j, j+1, ..., j-1, j. \tag{2.9}$$

In the following, only the case of the ${}^1_1$H hydrogen nucleus is considered. In this case, only two energy states are possible, and their energy difference is:

$$\Delta E = -\gamma \hbar B_0 \tag{2.10}$$

Transitions from one energy state to the other can be induced through interaction with oscillating magnetic fields perpendicular to the main field B_0. The energy of the interacting photon has to equal the energy difference. The frequency of the oscillating field is thus determined by the gyromagnetic ratio of and the main magnetic field:

$$\hbar\omega = \Delta E = \gamma \hbar B_0 \tag{2.11}$$

$$\omega = \gamma B_0. \tag{2.12}$$

This frequency is further referred to as the Larmor frequency (ω_L).
In MRI, the usual spatial resolutions are in the order of cubic-millimeter, the spin signal is thus averaged over a large number of spins. The occupation of the two possible energy states can be described statistically for this large number of spins. The ${}^1_1$H hydrogen nuclei are Fermions as they possess a half-integer spin, their occupation numbers thus following Fermi-Dirac statistics. The energy differences between states are small in MRI compared to the thermal energy at room temperature. For a main magnetic field of 7 T for example:

$$\Delta E_{7T} = 1.22 \cdot 10^{-6}\,\text{eV} \tag{2.13}$$

$$E_{Thermal} = k_B T \approx 25 \cdot 10^{-3}\,\text{eV} \quad \text{at } T = 300\,\text{K}, \tag{2.14}$$

with k_B the Boltzmann constant and T the temperature of the probe. In this *high-temperature* regime, the Fermi-Dirac statistic can be approximated by a Boltzmann distribution:

$$P(E_m) = \frac{e^{-E_m/k_BT}}{Z} \tag{2.15}$$

$$Z = \sum_m e^{-E_m/k_BT}. \tag{2.16}$$

The energy of each state E_m was defined in eq. (2.9). The ratio of the occupation numbers between the energetically favorable and disfavorable state is termed η and be expressed as:

$$\eta = \tanh \frac{\gamma\hbar B_0}{2k_BT} \tag{2.17}$$

$$\approx \frac{\gamma\hbar B_0}{2k_BT} \tag{2.18}$$

For typical in vivo temperatures and clinical MRI system with a main magnetic field strength of 1.5-7 T, this ratio is in the order of $1 \cdot 10^{-6}$ to $1 \cdot 10^{-5}$. This observation on the small polarization indicates in part why measured signals in NMR are inherently small and why great care has to taken detect and digitize these signal efficiently.
The detected NMR signal is the superposition of all of all magnetic moments of the probe and within this process of averaging the quantum mechanical properties of the system vanish, allowing a semi-classical description of the system. This behavior is termed the *correspondence principle*. The emerging macroscopic magnetization can thus be written as:

$$\vec{M} = \sum_i^n \langle\hat{\vec{\mu}}_i\rangle \tag{2.19}$$

$$= \sum_i^n \gamma\langle\hat{\vec{J}}_i\rangle \tag{2.20}$$

Only the J_z component has on average a finite expectation value, thus:

$$M_z = \frac{N\gamma^2\hbar^2 B_0}{4k_BT} \tag{2.21}$$

This macroscopic z-magnetization in thermal equilibrium will in the following be referred to as M_0.

2.1.2 Equation of Motion

The previous section motivated that averaging over all magnetic moments within a volume yields a macroscopic magnetization vector. The equation of motion for the macroscopic magnetization vector can be written and understood in a semi-classical manner. The equation of motion of a non-interacting magnetization vector is described by:

$$\frac{\partial \vec{M}}{\partial t} = \vec{M} \times \gamma \vec{B}. \tag{2.22}$$

This description is congruent with the quantum mechanical von Neumann equation:

$$\frac{\partial \langle \hat{\vec{\mu}} \rangle}{\partial t} = \langle -\frac{i}{\hbar} [\hat{\vec{\mu}}, \hat{\mathcal{H}}] \rangle. \tag{2.23}$$

This equation can be rewritten, using eqs. (2.5) and (2.8), as:

$$\frac{\partial \vec{\mu}}{\partial t} = \vec{\mu} \times \gamma \vec{B}. \tag{2.24}$$

This result immediately translates to the macroscopic magnetization:

$$\frac{\partial \vec{M}}{\partial t} = \vec{M} \times \gamma \vec{B}. \tag{2.25}$$

It can be stated that the temporal deviation of $\vec{M}$ vanished when $\vec{M} = |M|\hat{e}_z$, this is expected from eq. (2.21). A finite transverse magnetization precesses around the magnetic field with a frequency of γB.
For ease of mathematical description, a transformation into a rotating frame of reference is made, this can be done without loss of generality. In the following, the primed reference frame rotates with an angular velocity $\vec{\Omega}$ relative to the unprimed laboratory frame. Equation (2.25) can be rewritten as:

$$\frac{\partial \vec{M}}{\partial t} = \left(\frac{\partial \vec{M}}{\partial t} \right)' + \vec{\Omega} \times \vec{M} \tag{2.26}$$

$$\left(\frac{\partial \vec{M}}{\partial t} \right)' = \gamma \vec{M} \times \vec{B}_{eff}, \tag{2.27}$$

with

$$\vec{B}_{eff} = \vec{B} + \frac{\vec{\Omega}}{\gamma}. \tag{2.28}$$

2.1.3 Relaxation

The existence of an energy differences between orientation states of the magnetic moment was established in section 2.1.1. Further, the emergence of a finite difference in the occupation probability was motivated, but it was omitted by which the interaction state transitions are realized. This section will give a short overview on the fundamental interactions of the magnetization.

The characteristic time constant which describes that rate of change in the occupation number between the two energy states towards the thermal equilibrium, is termed T_1. The thermal equilibrium is defined by eq. (2.16). This process occurs when the probe is first introduced into the magnetic field or after the action of RF-pulses, which can change the occupation number. During the change in occupation numbers, the energy is dissipated into molecular motion. The misleading name of T_1 is *spin-lattice relaxation time*, which originates from solid state NMR experiments. For NMR in liquid, the is evidently no lattice, nevertheless, T_1 occurs.
A second relaxation time can be observed with NMR, representing spin-spin interactions. The *spin-spin relaxation time* T_2 describes a loss of phase coherence in the transverse plane between magnetic moments.

Based on empirical observation of both processes, Bloch formulated the well-known Bloch-equations [18]:

$$\frac{\mathrm{d}M_x(t)}{\mathrm{d}t} = \gamma(\vec{M} \times \vec{B})_x - \frac{M_x(t)}{T_2} \tag{2.29}$$

$$\frac{\mathrm{d}M_y(t)}{\mathrm{d}t} = \gamma(\vec{M} \times \vec{B})_y - \frac{M_y(t)}{T_2} \tag{2.30}$$

$$\frac{\mathrm{d}M_z(t)}{\mathrm{d}t} = \gamma(\vec{M} \times \vec{B})_z - \frac{M_z(t) - M_0}{T_1}. \tag{2.31}$$

Here, M_0 is the z-component of magnetization in thermal equilibrium. This equation is a generalization of eq. (2.22), to include interactions in form of relaxation. In the rotating frame of reference of the magnetization and in absence of a an RF-pulse, a solution can be written as:

$$M_\perp(t) = M_\perp(0)e^{-t/T_2} \tag{2.32}$$

$$M_\parallel(t) = M_0 - (M_0 - M_\parallel(0))e^{-t/T_1}, \tag{2.33}$$

with $M_\perp = M_x + iM_y$ and $M_\parallel = M_z$.

A more fundamental description of the relaxation process was proposed by Bloembergen et al. [19]. Here, interactions between magnetic moments are assumed stochastic,

these could for example based on dipolar coupling. This leads us to the definition of a correlation function linking the correlation between the perturbation at a time $t_0 + \tau$ to the perturbation a the time point t_0. The transition probability between a state m and k can be written as a function of the correlation function G_{mk}:

$$W_{km} = \frac{1}{\hbar^2} \int_{-\infty}^{\infty} G_{mk}(\tau) e^{i(\frac{E_m - E_k}{\hbar})\tau} \mathrm{d}\tau, \tag{2.34}$$

with $E_m - E_k$ the energy difference between the states and the temporal correlation of the perturbations is expressed by G_{mk}. The molecular motion inevitable causes this correlation to decay to zero. The molecular tumbling rate due to Brownian motion defines a correlation time τ_c after which a strong decay of G_{mk} is observed.
The similarity of eq. (2.34) to a Fourier-transform motivates the definition of a spectral density J_{mk}:

$$J_{mk}(\omega) = \int_{-\infty}^{\infty} G_{mk}(\tau) e^{-i\omega\tau} \mathrm{d}\tau. \tag{2.35}$$

The transition probability is now given by:

$$W_{km} = \frac{J_{mk}(\frac{E_m - E_k}{\hbar})}{\hbar^2} \tag{2.36}$$

J_{mk} indicates the probability of a transition at a given frequency to occur. This frequency evidently translates into an energy difference between states. In the simple case of an exponentially decaying correlation function, J_{mk} can be calculated by:

$$J_{mk}(\omega) = \frac{\tau_c}{1 + \omega^2 \tau_c^2}. \tag{2.37}$$

For the constructed scenario of an isolated spin pair with isotropic rotations and constant distance r, T_1 and T_2 can be expressed as:

$$\frac{1}{T_1} = K[J(\omega_L) + 4J(2\omega_L)] \tag{2.38}$$

$$\frac{1}{T_2} = K[3J(0) + 5J(\omega_L) + 2J(2\omega_L)]. \tag{2.39}$$

Here, K is a coupling constant dependent on the distance r of the dipolar interaction. For more realistic cases, T_1 and T_2 cannot be derived as easily from a given spectral density distribution.

2.2 Magnetic Resonance Imaging

Since the discovery of Magnetic Resonance Imaging (MRI) in 1971 by Paul C. Lauterbur this technique has gained significant importance in medical diagnostics. Although waste improvements have been made in the image quality and speed of the acquisitions, the fundamental principle of imaging has remained the same. The spatial encoding of the magnetization is achieved by the application of linearly varying magnetic field. To fully encode the spatial information, three of these magnetic fields are required. Their orientation is along the direction of the main magnetic field but their respective gradients span an orthogonal basis of the three-dimensional space. These spatial gradient fields induce a local shift of Larmor-frequency which allows the localization of the magnetization, as will be described in greater detail in the following sections.

2.2.1 Spatial Encoding

The following description of the spatial encoding is given in the rotating frame of the magnetization, further the magnetization will be assumed non-interacting and located in the transversal plane relative to the main magnetic field. This means that transversal magnetization precessing with $\omega_L = \gamma B_0$ in the laboratory frame, appears as static in the x-y-plane of the rotating frame of reference.
In a first step we consider a one dimensional object in x-direction, defined by its effective spin density $\rho(x)$. ρ may later include relaxation effects and other processes which are independent of the spatial encoding. Applying a temporally constant linear gradient along x for a time period t yields the following change in frequency and an accumulation of a phase relative to the static magnetization:

$$\omega_G(x) = \gamma x G \tag{2.40}$$

$$\phi_G(x,t) = -\int_0^t \omega_G(x,t')\mathrm{d}t \tag{2.41}$$

The acquired signal of the object as a function of the duration during which the gradient is applied can be written as:

$$s(t) = \int \rho(x) e^{i\phi_G(x,t)}\mathrm{d}x \tag{2.42}$$

Here the spatial frequency k can be introduced:

$$k(t) = \frac{\gamma}{2\pi}\int_0^t G(t')\mathrm{d}t', \tag{2.43}$$

Substituting $k(t)$ in eq. (2.42) makes the relation between the Fourier-transform and the measured signal apparent:

$$s(k) = \int \rho(x) e^{-i2\pi kx} \mathrm{d}x \tag{2.44}$$

The measured signal is hence the Fourier-transform of the effective spin density. If $s(k)$ is known of all k then the effective spin density can be computed by the well-defined inverse of the Fourier-transform:

$$\rho(x) = \int s(k) e^{i2\pi kx} \mathrm{d}k \tag{2.45}$$

In a realistic experiment $s(k)$ will never be know for all k. The consequences of measuring $s(k)$ in a finite range and at a finite number of sample points will be discusses in the following section. Note that at the beginning of this section t was introduced as the time period during which the gradient was applied prior to the data acquisition. This means that any delay can be inserted between the action of the gradient and the measurement of the signal. These two can be temporally uncorrelated, this is usually termed *phase-encoding*. If the data is acquired while the gradient G is switched on, then this process is called *frequency-encoding*. Despite the different terminology, these encoding techniques are equivalent in their action as they measure the space of spatial frequencies of the object (k-space).

Properties of Fourier Transform

The previous section alluded that measured data in MRI can be viewed as the sampling of the space of spatial frequencies, termed k-space. A detailed discussion of this unitary linear operator called Fourier operator $\mathcal{F}$, transforming between the two Hilbert spaces, the k-space and the Euclidean space (image space), is beyond the scope of this work. Nevertheless, some fundamental properties of this transformation are of utmost importance to the understanding of the presented techniques and methods. The first and potentially the most important property is the *linearly* of the transformation. Formally, this means:

$$\mathcal{F}(af(x) + bg(x)) = af'(\xi) + bg'(\xi) \tag{2.46}$$

here, f' and g' are the respective Fourier transforms of the functions f and g which are assumed integrable.
Further, the Fourier-shift theorem is of great importance in MRI, stating that a shift/translation in one of the Hilbert spaces results in a linear phase in the other and vice versa:

$$\mathcal{F}(f(x - x_0)) = f'(\xi) e^{-i2\pi x_0 \xi} \tag{2.47}$$

Lastly, the convolution theorem states that a multiplication of two functions in the Fourier-domain is equal to a convolution with the respectiv Fourier-transforms of in spatial domain:

$$f \cdot g = \mathcal{F}^{-1} \left\{ \mathcal{F}\{f\} * \mathcal{F}\{g\} \right\} \tag{2.48}$$

Discrete and Finite Sampling of k-Space

In theory, k-space can be sampled at arbitrary positions and correct images be can reconstructed, as long as a *dense* sampling is ensured. The definition of *dense* k-space sampling will be given in the following section. Nevertheless, in order to make use of the reduction in computational burden of the *fast Fourier transform* (FFT) compared to the direct definition of the *discrete Fourier transform* (DFT) a regular sampling on a Cartesian grid is required. This can either be achieved by directly measuring the data on such an Cartesian grid or by interpolating the data onto this grid using for example a Kaiser-Bessel window function [20]. The FFT algorithm reduces the computational burden from $\mathcal{O}(N^2)$ to $\mathcal{O}(N \log(N))$, where N is the number of data points. In a practical example of a volumetric high resolution head scan N can be in the order of: $N = 256^3 \approx 16.7 \cdot 10^6$. Here, the use of the FFT reduces the computational burden by a factor of 2.3 million, while producing the same result as the DFT. Compuation times would be unreasonably large if a DFT would be used, thus the following section assumes an equidistant distribution of sampling points.
This section again assumes a one-dimensional encoding problem but this can be applied to 3D as each orthogonal encoding direction is independent of all others. The discrete and finite sampling of the k-space can be understood in terms of a multiplication of the continuous signal with a Dirac-comb and a windowing function. The Dirac-comb, sometimes refereed to as sampling function, represents the action of acquiring a single data point while the duration of acquisition is assumed to be infinity short. Even though this represents an ideal sampling process, it is a good approximation of the actual sampling behavior. The Dirac-comb can be written as an infinite sum of Dirac-delta functions:

$$u(k) = \Delta k \sum_{p=-\infty}^{\infty} \delta(k - p\Delta k). \tag{2.49}$$

Here, Δk is the step size between sampling points. The measured signal $s_m(k)$, which can be acquired by the discrete sampling process can be written as:

$$s_m(k) = s(k) \cdot u(k) \tag{2.50}$$

$$s_m(k) = \Delta k \sum_{p=-\infty}^{\infty} s(p\Delta k)\delta(k - p\Delta k) \tag{2.51}$$

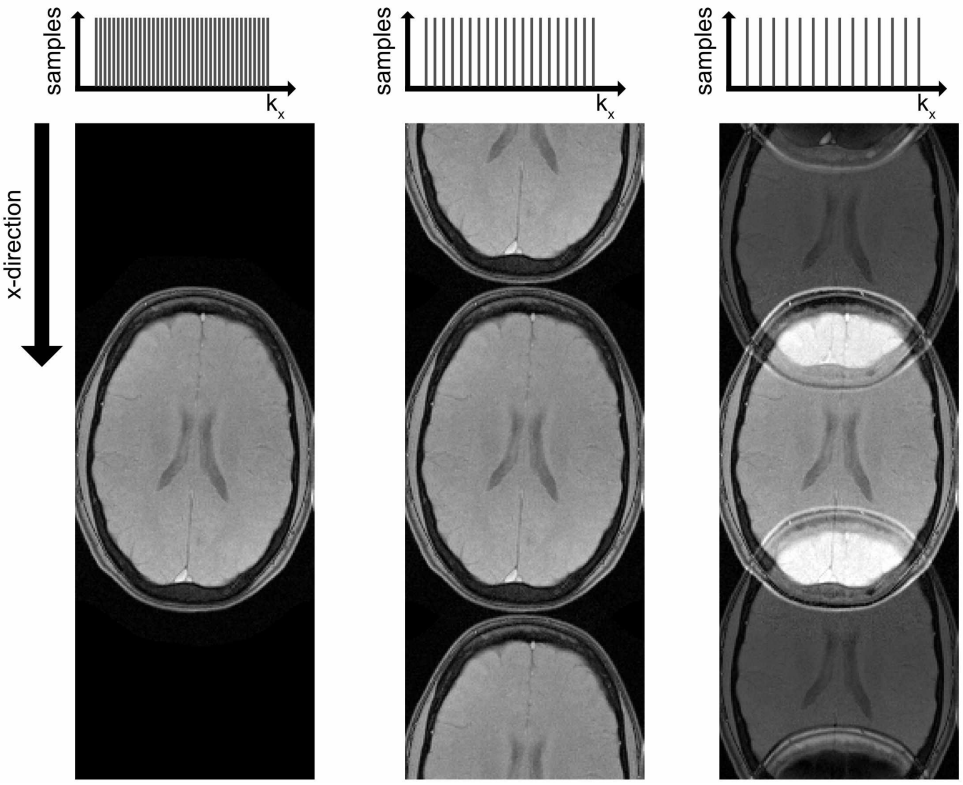

Figure 2.1: Schematic representation of the influence of the sampling density on the spread of the Dirac-comb in image space. A sampling rate higher then 2-fold the maximal frequency, as stated by the Nyquist sampling theorem, causes the delta function to be far apart in image space. In the first column they were cropped from the image. In the second image the sampling frequency is just above the Nyquist limit, here the images can still be separated without overlap. In the third image the sampling frequency is to low and the well know *fold-in* artifacts occurs.

An important side note, the Fourier-transform of the Dirac-comb is again a Dirac-comb but the spacing between delta function is the inverse of the previous spacing

Δk. Figuratively speaking, this means that a Dirac-comb with delta function *close* to one another will yield a Dirac-comb with delta function *far* apart when Fourier-transformed.

The consequences of the discrete sampling, described in eq. (2.51) together with the convolution theorem in eq. (2.48), are shown in fig. 2.1. Here, a densely sampled measurement, in the first column, is retrospective subsampled. This brings the additional delta functions in image space of the Dirac-comb closer to the central central image. The second column shows the minimal sampling frequency where no overlap occurs, this is usually the optimum for imaging as no excess of information has to be gathered. This minimal sampling frequency is also defined by the Nyquist sampling theorem. Sampling with frequencies lower than the Nyquist-limit is refereed to as *undersampling*, this is the case for the third column in fig. 2.1, for example. The discrete sampling of $s(k)$ is thus the reason why period images are reconstructed even though the measured object is non-periodic.

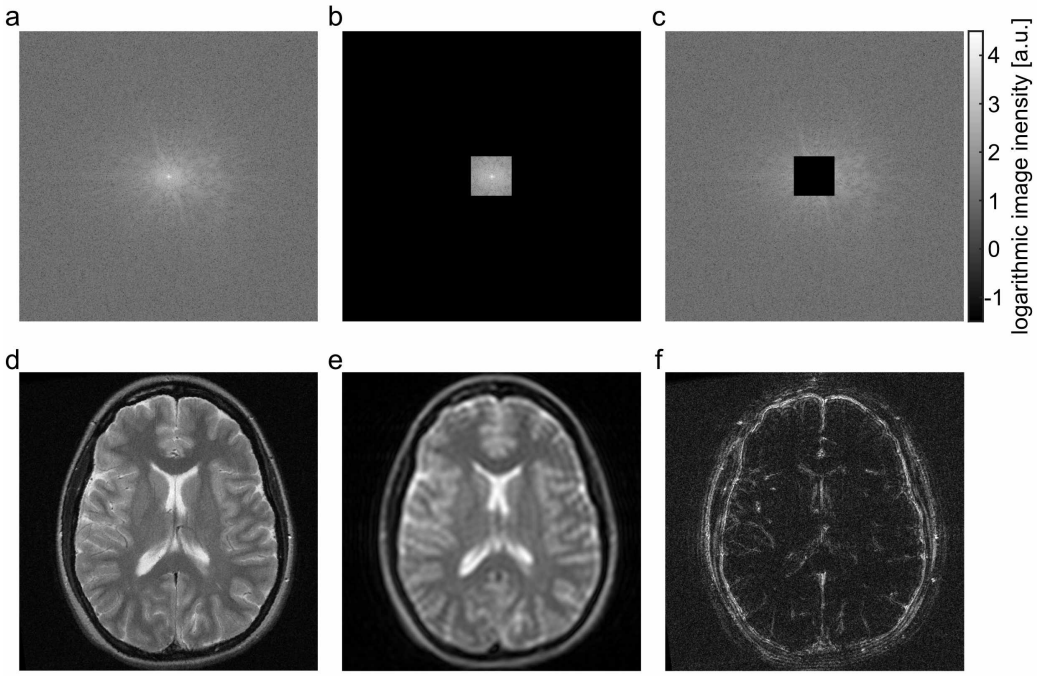

Figure 2.2: Images reconstructed from different parts of k-space are compared to the image of the complete k-space. The cropping of the outer parts of k-space as shown in (b) is equivalent to the application of a narrow windowing function. As discussed, this causes a broadening of the PSF and a low resolution image (e). The outer parts of k-space hold the edge information as can be seen in (f).

In any measurement k-space can only be sampled up to a maximum spatial frequency k_{max}. This effectively means that the continuous and infinite signal $s(k)$ is multiplied by a windowing function, usually a *rect* function with width $W = 2k_{max}$ and center around $k = 0$. Making use of the convolution theorem, as stated in eq. (2.48), indicates that this truncation of the infinite signal leads to a convolution of the *true* effective spin density with a sinc-function. Let $\hat{\rho}(x)$ be the estimated image:

$$\hat{\rho}(x) = \rho(x) * W\text{sinc}(\pi W x) \tag{2.52}$$

This eq. (2.52) imitatively shows that the point spread function (PSF) in MRI can be approximated, to a first order, as a simple sinc-function. An we can deduce that k_{max} determines the resolution of the image as it defines the width of the PSF. Figure 2.2(a,b,d,e) illustrate this observation. Figure 2.2a,d show a large k_{max} and as a results a high resolution image, while fig. 2.2b,e show a small k_{max} resulting in a larger PSF and a blurred image. A direct influence of the sinc-shaped PSF can be seen in fig. 2.2e as ripples in the brain, often refereed to as Gibbs-ringing. Applying additional weighting function to the data, such as a Hamming-window function, can reduce these ripples but a the cost of a broadening of the PSF. Figure 2.2c,f illustrate that the outer parts of k-space hold the edge information of the image.

Non-Cartesian k-space sampling

The previous section motivated why sampling k-space on a Cartesian grid is desirable because of the reduction in computational burden of the FFT compared to a general DFT. Cartesian k-space sampling, on the other hand, was not explained. In the simplest case of Cartesian imaging, one of the three spatial dimensions is encoded via the frequency-encoding as described in section 2.2.1, the other two are encoded via phase-encoding steps. This means that after each excitation of the magnetization a parallel line in k-space is acquired. This process is repeated for each phase-encoding step until the k-space is filled such that the desired spatial resolution is achieved and the Nyquist sampling theorem fulfilled. This sampling scheme has many advantages, especially in regards to its robustness against system imperfections, but a detailed description of those is beyond the scope of this work. Here,the focus lies on the differences in undersampling behavior between Cartesian and non-Cartesian imaging. The most commonly used non-Cartesian k-space trajectories are spiral and radial trajectories. Both are illustrated in fig. 2.3. In radial imaging a straight line in k-space is acquired, either from the center of k-space outward or a complete spoke from $-k_{max}$ to $-k_{max}$ going through $k = 0$.

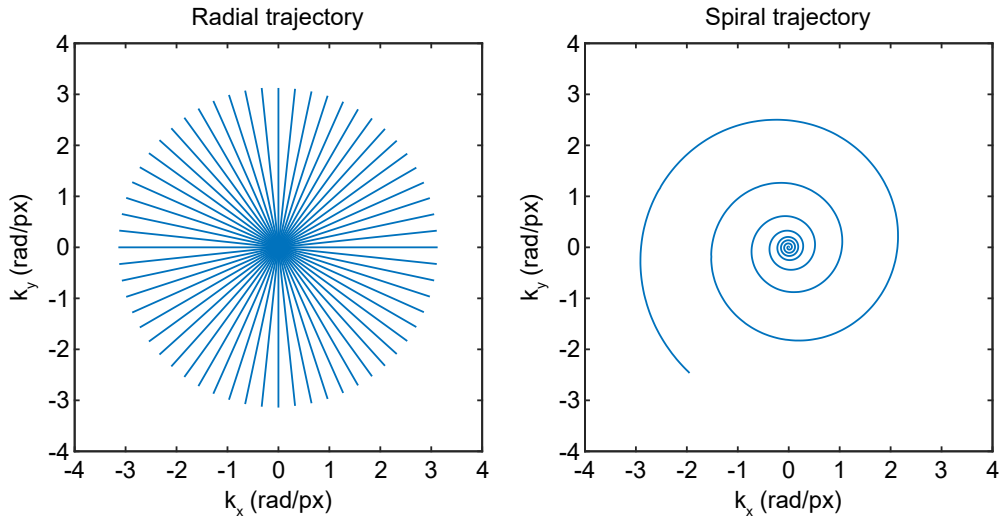

Figure 2.3: Two common non-Cartesian k-space trajectories are shown. The first image shows a host of radial trajectories, while only a single variable density spiral-trajectory is shown in the second image.

The angle of the spoke in the k_x-k_y plane is then incremented until the k-space is fully sampled. The same process can be used for spiral imaging the only difference is that a single acquisition samples a spiral trajectory (see fig. 2.3) in k-space. Here, variable density spiral as in fig. 2.3 or Archimedean spiral can be used.

Inspecting either trajectory in fig. 2.3 shows that the density of sample points is no longer homogeneous throughout k-space. Interpolating the data simply onto the Cartesian grid, as described in section 2.2.1, will lead to a higher weighing of the spatial frequencies with a larger sampling density. This is equivalent to multiplying a homogeneously sample k-space with a weighting function, just like the windowing function in previous section. A greater weighting of low spatial frequencies, as found in radial imaging, leads to a strong broadening of the PSF, thus a blurring of the reconstructed image as can be seen in fig. 2.4. This effect can be eliminate by applying an additional weighting of the data with the inverse of the sampling density, called density compensation (DC). The trajectories used in this work all have a by design a rotational symmetry around $k = 0$. The sampling density is thus a pure function of $|k|$. For 2D imaging the density compensation as a function of the discrete samples n can be written as:

$$d(n) = \pi \frac{\mathrm{d}|k|^2}{\mathrm{d}n} \tag{2.53}$$

$$s_{dc}(n) = s_m(n)d(n). \tag{2.54}$$

Here, n is indexing the sampled points along the trajectory and s_{dc} is the density compensated signal that can be interpolated yielding an image with a PSF as described in eq. (2.52).

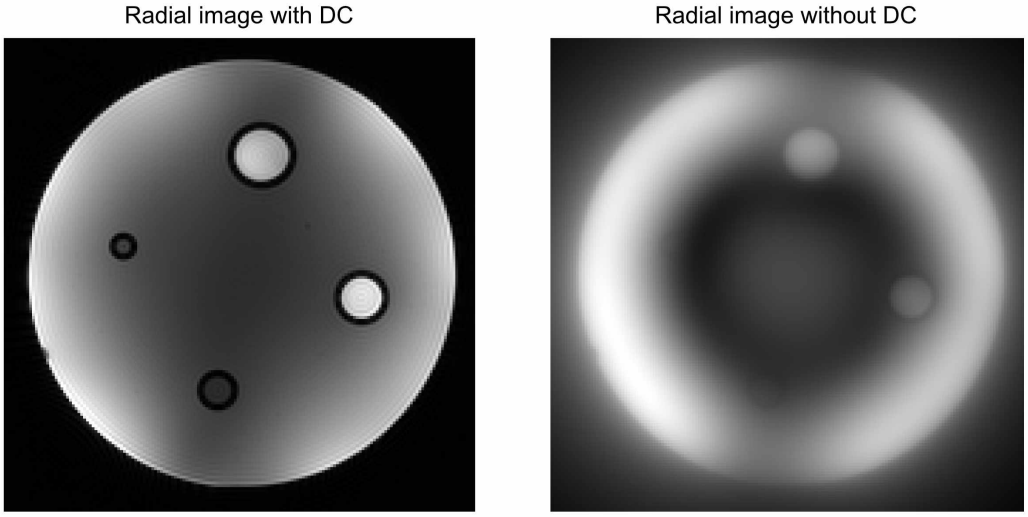

Figure 2.4: The influence of a sampling density compensation is illustrated in this figure. The first image shows the reconstructed image with density compensation and the second one is reconstructed without DC. The circular dropout in the second image is cause by spatial phase variations. Although the magnitude is shown here, these images are inherently complex valued.

k-space undersampling

Undersampling (US) of k-space, as previously stated, is defined when the Nyquist sampling theorem is not fulfilled and it some part of the magnetization is mislocalized as in the third image in fig. 2.1. An equivalent definition would be that Δk between any nearest neighbors anywhere in k-space is smaller then $1/L$ where L is the largest dimension of the object:

$$\Delta k = \frac{1}{L}. \tag{2.55}$$

For radial imaging the spacing between sample points in polar direction is always the largest at k_{max}. For this reason, radial images can be undersampled while preserving the image quality as most of the k-space still fulfills the Nyquist criterion. This is illustrated in fig. 2.5.

Visual inspection shows only very light *streak-like* radial US artifacts when undersampling by a factor of 2-4. These become more prominent for US factors of 8-16 to a point where a real degradation of image quality can be noted. The last image, with an US factor of 140, was reconstructed from 5 radial projections. This is the same amount of spatial data per timeframe that is used in most MRF applications in this work. For this imaging protocol with a spatial resolution of $0.8\,\text{mm}$ in-plane and a square FOV of 190 mm approximately 700 radial projections are needed to fully sample the image. The visual appearance the US artifacts in regularly sampled Cartesian imaging, as in the third image in fig. 2.1, and in radial image is highly dissimilar. In Cartesian imaging the *fold-in* artifact is highly structured and spaciously localized, this is because Δk is constant throughout k-space. In radial or variable density spiral imaging Δk is changing locally, thus spreading out the US artifacts within the whole spatial domain. This is also possible in Cartesian imaging when variable Δk are used but the US artifacts still show a higher correlation to actual image then in radial or spiral imaging.

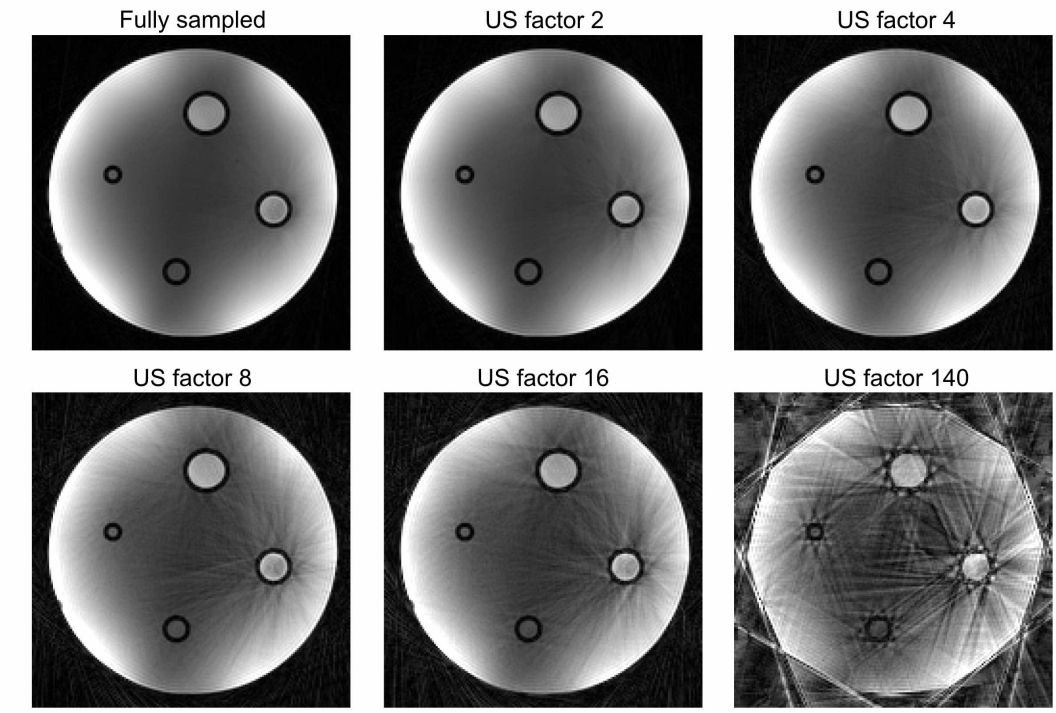

Figure 2.5: This figure illustrates the effects of radial undersampling with different undersampling factors. The visual impression of the image is well preserved, even for 16-fold undersampling.

2.2.2 Gradient moments

The quantification of velocities is of a central importance to this work. This section will define the prerequisite notions needed for the explanations of the presented velocity encoding techniques.
The special case of static and a one-dimensional object has been discussed in section 2.2.1. The phase of the signal took a simple form as shown in eq. (2.41). In a more general case:

$$\varphi(\vec{r}(t),t) = \varphi(\vec{r}(t_0),t_0) + \gamma \int_{t_0}^{t} \vec{G}(t')\vec{r}(t')\mathrm{d}t', \tag{2.56}$$

here t_0 is the start point of integration. This point reefers to the point instantaneous creation of the magnetization (isodelay point) [21]. For the symmetric excitation pulses in the small tip angle regime, this point can be defined as the center of the RF pulse.
Assuming vanishing acceleration and higher order motion terms, the truncated Taylor expansion yields:

$$\vec{r}(t) = \vec{r}_0 + \vec{v}_0(t - t_{exp}). \tag{2.57}$$

The choice of expansion time point has a direct influence on the calculation of the flow encoding gradients as was shown in [22, 23]. In this work the expansion time point was always set to the echo time.
Further, we define the n^{th} gradient moment as:

$$\vec{m}_n(t) = \int_{t_0}^{t} \vec{G}(t')(t' - t_{exp})^n \mathrm{d}t'. \tag{2.58}$$

Substituting eqs. (2.57) and (2.58) in the previous equation of signal phase yields:

$$\varphi(\vec{r}_0 + \vec{v}_0 t, t) = \varphi(\vec{r}_0, t_0) + \gamma\vec{r}_0 \int_{t_0}^{t} \vec{G}(t')\mathrm{d}t' + \gamma\vec{v}_0 \int_{t_0}^{t} \vec{G}(t')(t' - t_{exp})\mathrm{d}t' \tag{2.59}$$

$$\varphi(\vec{r}_0 + \vec{v}_0 t, t) = \varphi_0 + \gamma\vec{r}_0\vec{m}_0(t) + \gamma\vec{v}_0\vec{m}_1(t). \tag{2.60}$$

Equation (2.60) immediately shows that the zeroth gradient moment is related to the spatial encoding, the first to velocity encoding and following moments are linked to higher orders of motion such as acceleration, jerk, and so on.

Reconsidering eqs. (2.43) and (2.60), the relations between the spatial frequencies and the zeros gradient moments become apparent:

$$\vec{k}(t) = \frac{\gamma}{2\pi} \int_0^t \vec{G}(t')\mathrm{d}t' \tag{2.61}$$

$$= \frac{\gamma}{2\pi} \vec{m}_0(t) \tag{2.62}$$

2.2.3 Action of Radio Frequency Pulses

The formation a finite macroscopic z-magnetization in thermal equilibrium has been shown in section 2.1. In the following section 2.2, the assumption of a finite transverse magnetization was made, such that the spatial encoding of said magnetization could be discussed. Until now the process by which transverse magnetization can be created from longitudinal magnetization has not been explained. This section will give a general overview of how the magnetization can be manipulated by radio frequency (RF) pulses.
The RF pulses are creating linearly or circularly polarized magnetic field in an orthogonal direction relative to the main magnetic filed. This magnetic field is further referred to as B_1-field:

$$\vec{B}_1 = B_1(\hat{e}_x \cos(\omega t) + \hat{e}_y \sin(\omega t)) \tag{2.63}$$

If the angular frequency of the rotating frame of reference is: $\vec{\Omega} = -\omega \hat{e}_z$ then $\vec{B}_1$ can be written in this frame as:

$$\vec{B}_1 = B_1 \hat{e}'_x. \tag{2.64}$$

The phase of the B_1 field is neglected for now.

Reconsidering the equation of motion in the rotating frame of reference, stated in eqs. (2.27) and (2.28), in the presence of a finite RF field:

$$\left(\frac{\partial \vec{M}}{\partial t}\right)' = \vec{M} \times [\hat{e}'_z(\omega_0 - \omega) + \hat{e}'_x \omega_1] \tag{2.65}$$

$$= \gamma \vec{M} \times \vec{B}_{eff} \tag{2.66}$$

with

$$\omega_1 \equiv \gamma B_1 \tag{2.67}$$

Assuming that the resonance condition is met, meaning that $\omega = \omega_0$, then $\vec{B}_0$ has a vanishing influence on the dynamic of the magnetization in the rotating frame:

$$\left(\frac{\partial \vec{M}}{\partial t}\right)' = \omega_1 \vec{M} \times \hat{e}'_x \tag{2.68}$$

Equation (2.68) also assumes that the RF-phase ϕ is zero, in practice however, the $\vec{B}_1$ field takes the more general form:

$$\vec{B}_1 = B_1 \cos(\phi)\hat{e}'_x + B_1 \sin(\phi)\hat{e}'_y. \tag{2.69}$$

This simply changes the axis of rotation on in eq. (2.68) from $\hat{e}'_x$ to $\cos(\phi)\hat{e}'_x + \sin(\phi)\hat{e}'_y$. The solution of eq. (2.66), or in the special case of on-resonance eq. (2.68), is a rotation around the effective B field and the rate of rotation is proportional to its magnitude. The angle of polar rotation θ is defined as the flip angle (FA) and can be written in the on-resonant case as:

$$\alpha = \int \gamma B_1(t) \mathrm{d}t \tag{2.70}$$

2.2.4 Slice Selection & Small Tip Angle Solution

A spatial modulation of the FA can be achieved in MRI by combining RF pulses with linear gradient fields, which were introduced at the beginning of section 2.2. In the case of small excitation flip angle a closed form solution for the excitation profile in the presence of gradients can be derived. In this case the following approximations can be made: $\cos(\theta) \approx 1$ and thus $M_z \approx M_0$. Hereby, the longitudinal and transverse equation decouple.
Defining:

$$M_+ = M_x + iM_y \tag{2.71}$$

and

$$B_{1+} = B_{1x} + iB_{1y}. \tag{2.72}$$

Equation (2.66) can now be reduced to:

$$\frac{\mathrm{d}M_+}{\mathrm{d}t} = -i\gamma(\vec{G}\vec{r})M_+ + i\gamma B_{1+}M_0 \tag{2.73}$$

Assuming an RF pulse of length τ_{RF} centered around the temporal origin with initial conditions of $M_x(\vec{r}, -\tau_{RF}/2) = M_y(\vec{r}, -\tau_{RF}/2) = 0$ and $M_z(\vec{r}, -\tau_{RF}/2) = M_0$.

Equation (2.73) is a first order linear ordinary differential equation and can thus be solved by:

$$M_+(\vec{r}, \tau_{RF}/2) = i\gamma M_0 \int_{-\tau_{RF}/2}^{\tau_{RF}/2} B_{1+}(t) e^{-i2\pi\vec{k}(t)\vec{r}} \mathrm{d}t. \tag{2.74}$$

Here, k has a time reversed definition compared to eq. (2.43):

$$\vec{k}(t) = \frac{\gamma}{2\pi} \int_{t}^{\tau_{RF}/2} \vec{G}(t')\mathrm{d}t' \tag{2.75}$$

From eq. (2.74) it becomes evident that in the case of a constant gradient during the excitation, that the excited profile is the the Fourier transform of the excitation pulse. To achieve a slice selective excitation, as a consequence, a sinc-shaped excitation pulse can be used. As for the spatial encoding during the readout, described in section 2.2.1, the finite sampling of the k-space has to be considered. To differentiate between readout and excitation, the just introduced k-space is usually referred to as excitation k-space [21].

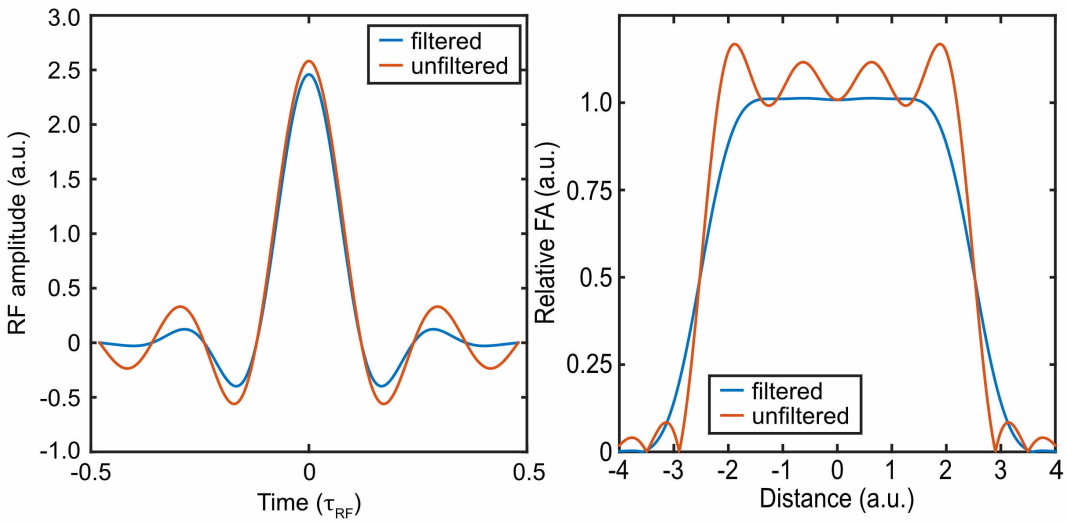

Figure 2.6: RF-pulse envelope and corresponding slice profile for a filtered and unfiltered sinc-pulse.

Figure 2.6 illustrates the effect of a simple truncation (boxcar windowing function) in excitation k-space. Equation (2.52) already showed that this results in a sinc-shape

PSF in the image domain, labeled as *unfiltered* in fig. 2.6. Applying an additional weighting in the excitation k-space can smooth the spectral response function. On the excitation side the broadening of the PSF is less important then on the readout side, where image filters are less common. For the excitation the high oscillations and on the profile and high side-lobes make unfiltered pulses virtually unusable. Thus for all slice selective excitations the following Hanning-windowed pulse envelope was used:

$$B_1(t) = \begin{cases} At_0 \underbrace{\left[(1-\alpha) + \alpha \cos\left(\frac{\pi t}{Nt_0}\right)\right]}_{\text{filter-function}} \frac{\sin\left(\frac{\pi t}{t_0}\right)}{\pi t} & , -Nt_0 \leq t \leq Nt_0 \\ 0 & , \text{elsewhere} \end{cases} \tag{2.76}$$

With A a scaling factor, t_0 halved width of the central lobe, N half of the number of zero crossings and α a constant of value 0.46. The width of the excitation PSF is determined by N or the so called bandwidth-time-product (BWT), which simply is equal to $2N$.

2.2.5 Extended Phase Graph Formalism

The Extended Phase Graph (EPG) formalism allows a description of the signal behavior in spoiled sequences [24]. In the EPG formalism, the action of RF-pulses is described by the partitioning effect [25]. Further, the state of the magnetization is expressed by integer Fourier-coefficients of the spatial dephasing state. The combination of these descriptions allows the formation of stimulated echos and partial spin echos to be predicted more intuitively than in Bloch-simulations.

For convenience, the magnetization is not expressed in terms of the spatial coordinates components $M_x, M_y,$ andM_z but in states denoted $M_+, M_-,$ andM_z. The relation between the two representations is:

$$\begin{pmatrix} M_+ \\ M_- \\ M_z \end{pmatrix} = U \begin{pmatrix} M_x \\ M_y \\ M_z \end{pmatrix}. \tag{2.77}$$

Here, the transformation matrix U can be written as:

$$U = \frac{1}{\sqrt{2}} \begin{pmatrix} 1 & +i & 0 \\ 1 & -i & 0 \\ 0 & 0 & \sqrt{2} \end{pmatrix}. \tag{2.78}$$

i denotes the imaginary unit. The rotating action after an RF pulse on the magnetization can also be transformed into the new representation. The state of the magnetization of an RF pulse, denoted M^+, as a function of the state before the RF pulse (M^-) can be calculated from the following equation:

$$\begin{pmatrix} M_+ \\ M_- \\ M_z \end{pmatrix}^+ = \begin{pmatrix} \cos^2\left(\frac{\alpha}{2}\right) & e^{2i\Phi}\sin^2\left(\frac{\alpha}{2}\right) & ie^{i\Phi}\sin(\alpha) \\ e^{-2i\Phi}\sin^2\left(\frac{\alpha}{2}\right) & \cos^2\left(\frac{\alpha}{2}\right) & -ie^{i\Phi}\sin(\alpha) \\ -\frac{i}{2}e^{-i\Phi}\sin(\alpha) & \frac{i}{2}e^{-i\Phi}\sin(\alpha) & \cos(\alpha) \end{pmatrix} \begin{pmatrix} M_+ \\ M_- \\ M_z \end{pmatrix}^- \tag{2.79}$$

In these equations, α is the FA and Φ the RF-phase.

The previously mentioned Fourier decomposition is defined in the following manner:

$$\tilde{F}_+(\vec{k}) = \int_V M_+(r)e^{-ikr}\mathrm{d}^3r \tag{2.80}$$

$$\tilde{F}_-(\vec{k}) = \int_V M_-(r)e^{-ikr}\mathrm{d}^3r \tag{2.81}$$

$$\tilde{Z}(\vec{k}) = \int_V M_z(r)e^{-ikr}\mathrm{d}^3r \tag{2.82}$$

The matrix describes the action of RF-pulses as in eq. (2.79) is identical for the Fourier-coefficients, due to the linearity of the Fourier-transform:

$$\begin{pmatrix} \tilde{F}_+(\vec{k}) \\ \tilde{F}_-(-\vec{k}) \\ \tilde{Z}(\vec{k}) \end{pmatrix}^+ = \begin{pmatrix} \cos^2\left(\frac{\alpha}{2}\right) & e^{2i\Phi}\sin^2\left(\frac{\alpha}{2}\right) & ie^{i\Phi}\sin(\alpha) \\ e^{-2i\Phi}\sin^2\left(\frac{\alpha}{2}\right) & \cos^2\left(\frac{\alpha}{2}\right) & -ie^{i\Phi}\sin(\alpha) \\ -\frac{i}{2}e^{-i\Phi}\sin(\alpha) & \frac{i}{2}e^{-i\Phi}\sin(\alpha) & \cos(\alpha) \end{pmatrix} \begin{pmatrix} \tilde{F}_+(\vec{k}) \\ \tilde{F}_-(-\vec{k}) \\ \tilde{Z}(\vec{k}) \end{pmatrix}^- \tag{2.83}$$

Like before, the superscript +/- describe the states before and after the RF-pulse. Equation (2.83) shows that any RF-pulse causes mixing between states. The action of gradients can be described as a shift operator on the Fourier-states:

$$\tilde{F}_+(\vec{k}) \to \tilde{F}_+(\vec{k} + \Delta\vec{k}) \tag{2.84}$$

$$\tilde{F}_-(\vec{k}) \to \tilde{F}_-(\vec{k} + \Delta\vec{k}) \tag{2.85}$$

$$\tilde{Z}(\vec{k}) \to \tilde{Z}(\vec{k}) \tag{2.86}$$

$$\tag{2.87}$$

Here, $\Delta\vec{k}$ is the total moment of the gradient.

Based on the EPG formalism, the origin of echos can be characterized. In the following, the *FID signal path* is defined the as $F(0)_+$ state excite by the RF-pulse just before the acquisition from the $\tilde{Z}(0)$ state. Stimulated echos are defined as $F(0)_+$ states, which were excited from a $\tilde{Z}(n\Delta\vec{k})$ by n RF-pulses before the acquisition. It is assumed that during each TR a spoiling moment of $\Delta\vec{k}$ is applied. Partial spin echos can be identified by the fact that they occupy the $\tilde{F}_-(-\Delta\vec{k})$ state before being shifted to the $\tilde{F}_-(0)$ by the action of a gradient.

2.2.6 Fast Gradient Echo Sequences

Fast gradient echos (GRE) sequences are extensively used in clinical MRI examinations. These sequences can be generally categorized as *spoiled* or *balanced* GRE sequences. The attribute *balanced* refers to the rewinding of all zeroth gradient moments during a TR, this sequence is often refereed to as bSSFP. The original MRF sequence was bSSFP-based because the image contrast is influence strongly by both T_1 and T_2. Unfortunately, ΔB_0 also influences the signal, reducing its applicability at ultra high fields. Here, *spoiled* sequences are preferred, which are characterized by an unbalanced zeroth gradient moment at the end of a TR, dephasing the magnetization by multiples of 2π over a voxel. This so called spoiling creates a ΔB_0 insensitive image contrast.

An important parameter for spoiled GRE sequences is the RF-phase evolution. Typically a quadratic phase evolution is chosen such hat the influence of all non-FID signal paths vanish, this is often called a FLASH sequence.

$$\varphi_j = \frac{1}{2}\varphi_0(j^2 + j + 2) \tag{2.88}$$

φ_0 phase/spoiling increment and j indicates the j^{th} TR of the sequence. Different phase increments have been proposed to minimize the effect of non-FID signal paths such as 117° by Zur et al. [26]. Choosing a spoiling increment of 0° results in a maximally constructive interference, this sequence is often termed a FISP sequence. Even in the signal steady state a significant influence of T_2 on FISP image contrast can be seen.

Figure 2.7 illustrates the sequence diagram for a spoiled GRE sequence alongside the evolution of the zeroth gradient moment during a single TR. For this exemplary diagram gradient spoiling is performed in both read and slice direction. The gradient moment in phase encoding direction is changing from one k-space line to the next, thus moment nulling is preferred on this axis for ease of gradient calculation. A variable spoiling moment on any axis can cause artifacts.

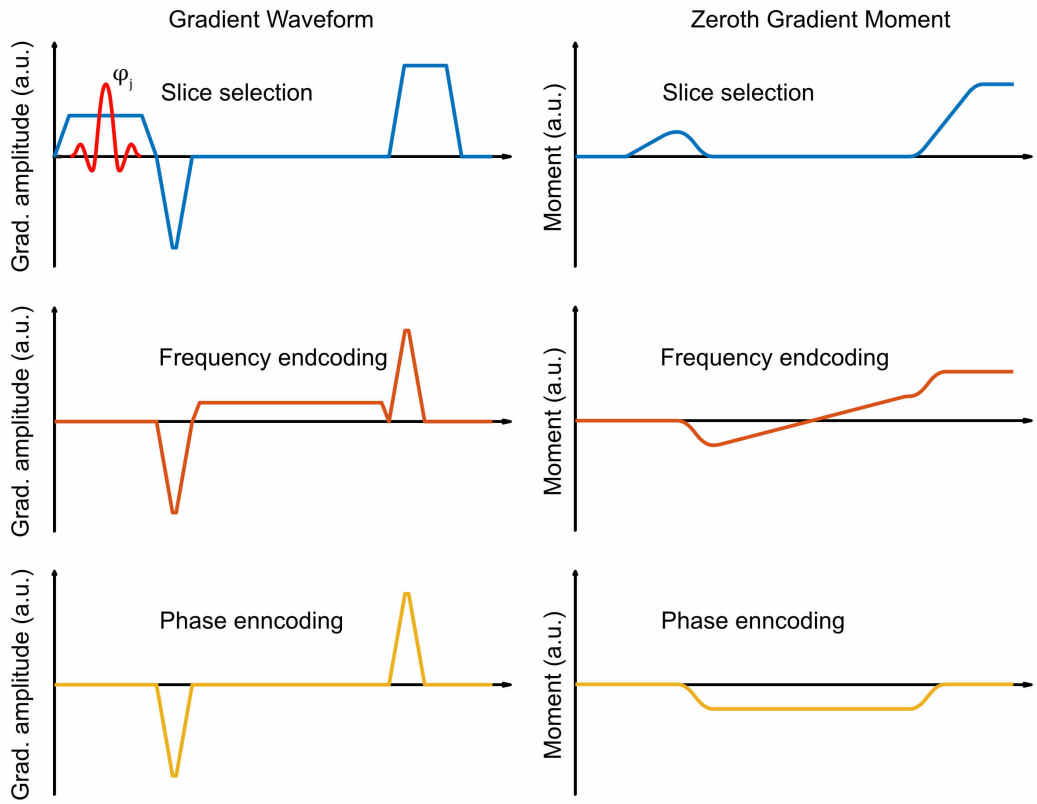

Figure 2.7: Schematic sequence diagram of a spoiled GRE sequence. The corresponding zeroth gradient moments are displayed on the right of each gradient axis. This sequence is called *spoiled* because the zeroth gradient moment at the end of a TR is non-zero.

Figure 2.8 shows exemplary transient states of a FLASH, FISP and bSSFP sequence at different FAs. The spoiling increment for the FLASH sequence was set to 117 ° and a cycling increment of 180 ° was chosen for the bSSFP sequence. The importance of the transient states for MRF are detailed in the following section.

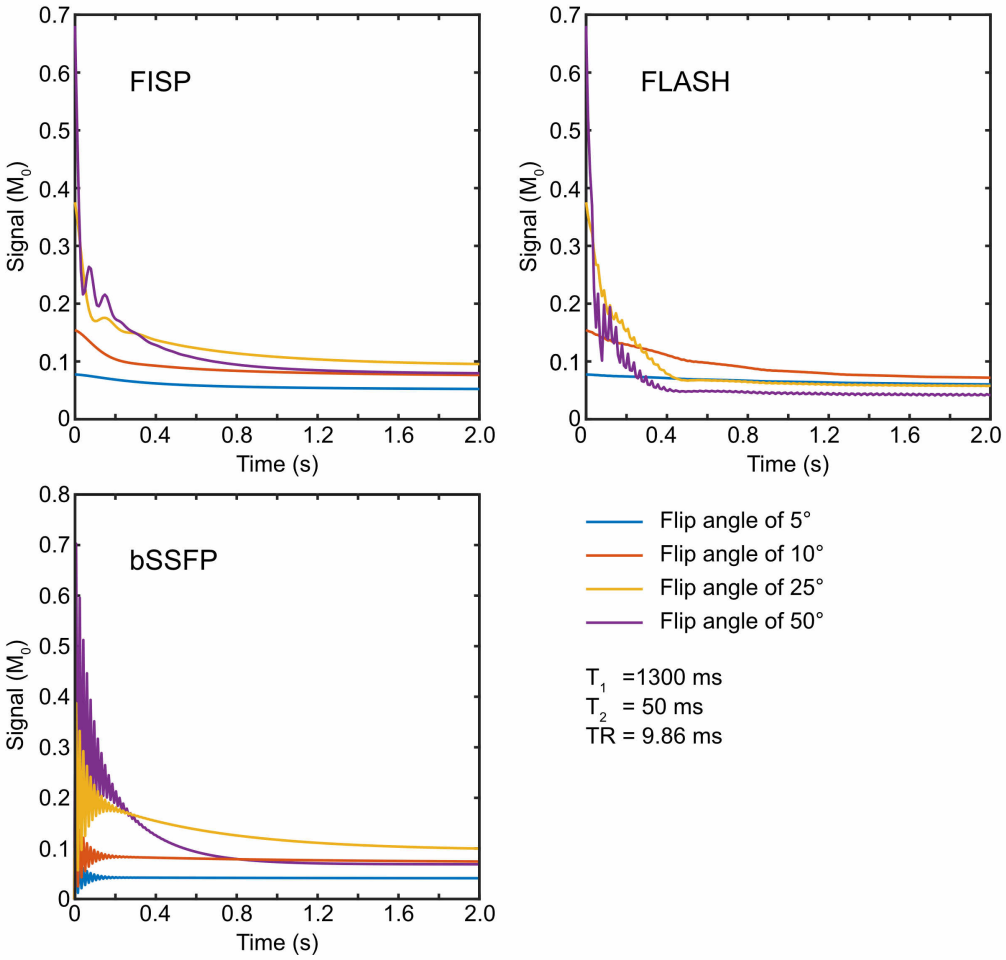

Figure 2.8: Transient behavior for different GRE sequences as a function of the excitation FA.

2.3 MR Fingerprinting

Magnetic Resonance Fingerprinting [7] is a technique aiming to achieve rapid quantitative imaging by acquiring a spatially highly undersampled time series of the sequence-driven transient signal. In theory, any parameter quantifiable with MRI can likewise be quantified by MRF but most prominently the aim is to quantify T_1 and T_2. At its core, MRF can be split into three mostly independent parts: The sequence-driven transient signal behavior, the undersampled image acquisitions, and the simulation-based model reconstruction. Rarely, some applications of MRF neglect one or two of the aforementioned parts, nevertheless these parts are the defining features of MRF. Rieger et al., for example, used a fully sampled EPI readout [27] to achieve high SNR in all time frames. The following sections are dedicated to a more detailed description of each of the three parts.

2.3.1 Transient Signal Evolution

Subjecting the magnetization to the action of the same RF pulse at regular intervals drives the magnetization into a steady state, which is usually wanted in fast imaging sequences. A multitude of parameters, such as FA, TE, TR and the RF-phase, influence the exact state into which the magnetization is driven and consequently the precise steady state signal. A change in any of the aforementioned parameters thus entails a transition period from one steady state to the next. A sequence-driven transient state can be achieved by changing key sequence parameters before a steady state is reached. The FA and the TR have the most significant impact on the steady state for the T_1 and T_2 quantification, motivating the extensive use of these in MRF.
Both relaxation parameters are well suited to be quantified based on transient signals as they inherently describe the temporal behavior of the magnetization and they have a temporally extended effect on the transient signal. This effect can be seen in figs. 2.8 and 2.9 where the simplest case of transient behaviors are shown, namely the beginning of a periodic sequence where the magnetization is in thermal equilibrium at the temporal origin. Figure 2.9 shows example transient signal curves for different T_1 and T_2 values obtained with a FISP sequence. In this specific example, T_1 mainly dominates the rate of decay to the steady state signal level while longer T_2 introduces an oscillatory behavior at the beginning of the sequence. Strong coupling between the effect of T_1 and T_2 exists, but these unique signal features allow the separation of both parameters in the MRF reconstruction.

The steady state signal is again strongly dependent on both T_1 and T_2, but the absolute signal level does not directly provide information of either parameter. This is because other parameters in MRI introduce scalar factors into the measured signal level, most prominently the proton density ρ_0 and the receive sensitivity B_1^-. This is the reason

why any MRF-quantifiable parameter has to have an explicit time dependance in its impact on the MR signal. The dependence of the steady state signal level on sequence parameters may be small as can be seen in fig. 2.8, where the flip angle is varied for different sequence types. A higher signal variation as a function of sequence parameters can be achieved during the transient state compared to the steady state. This statement is difficult, to prove formally, but it constitutes one of the main reasons why MRF can reach higher efficiency than conventional relaxometric steady state methods, such as DESPOT 1& 2 [10]. The efficiency in this context is defined as a modified Crawley-Henkelmann metric similar to the one proposed by Deoni et al. [10]:

$$\Lambda = \sum_i \frac{1}{\sigma_i V \sqrt{TA}}. \tag{2.89}$$

Here, Λ is the efficiency, i an index summing over all quantified parameters, σ_i the noise level of each quantified parameter, V the voxel volume, and TA the acquisition time.

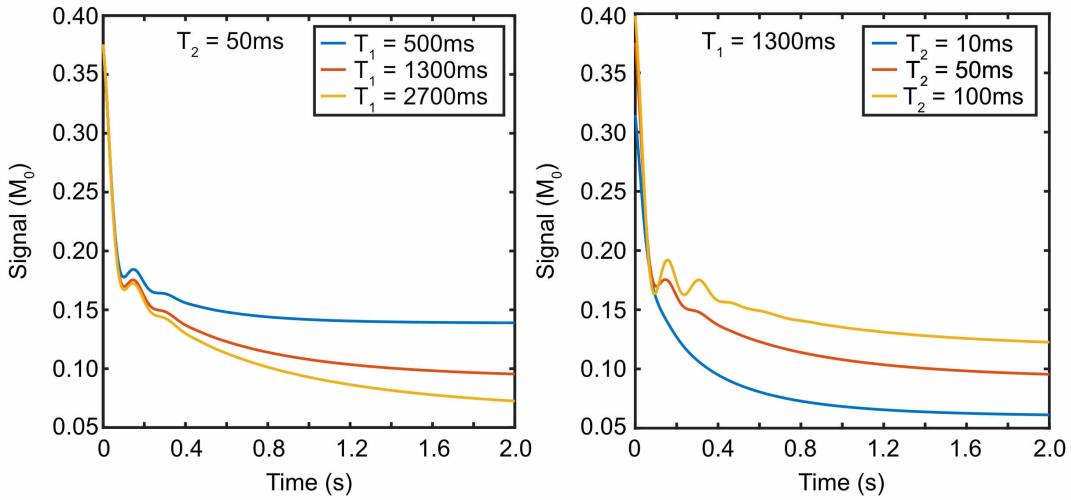

Figure 2.9: Transient signal evolution at the beginning of a FISP sequence with a constant FA of 25 ° and a constant TR of 9 ms displayed for varying T_1 and T_2 constants.

2.3.2 Undersampled Image Acquisition

The spatial undersampling in each time frame is the feature of MRF, which allows short acquisition times, in the order of seconds, to be reached. Examples of these undersampled time frames can be seen in fig. 2.10. Spatial undersampling of often used to accelerate measurements and the missing data can then be completed using

compressed sensing. The spatial undersampling in MRF, however, is different from the undersampled acquistions used in conjunction with compressed sensing. In MRF, each time frame is undersampled but over the whole stack of time frames, the complete spatial information is acquired. Here, the linearity of the Fourier-transform (eq. (2.46)) is exploited by spreading the acquisition of spatial information over the whole MRF sequence.
In a conventional imaging experiment the acquired spatial data is combined in the k-space and a finally Fourier-transform is applied on the fully sampled k-space. Assuming, without loss of generality, a Cartesian k-space readout and let $d(k_i)$ represent the data of the i^{th} k-space line, with i enumerating over all measure k-space line. The reconstruction of the image I can then be written as:

$$I = \mathcal{F}\left[\sum_i d(k_i)\right]. \tag{2.90}$$

Here, $\mathcal{F}$ is a Fourier-operator transforming between frequency and image space. Equivalently to eq. (2.90), each k-space line could be transformed into the image space and then summed up. This would result in an identical image:

$$I = \sum_i \mathcal{F}[d(k_i)]. \tag{2.91}$$

As alluded to at the beginning of the section and restated by eqs. (2.90) and (2.91), the linearity of the Fourier-transform allows the summation to be performed in the complex image space, yielding an identical images. This is a central observation needed for the understanding of MRF, as here, each individual time frame is undersampled but the entirety of the time series samples the k-space densely enough to fulfill the Nyquist-theorem. As a side note, the spatial information in MRF usually oversamples the k-space multifold, although a sub-Nyquist-theorem amount of spatial information is feasible if iterative compressed sensing (CS) reconstructions are used. The previous statements are illustrated in fig. 2.10 where individual time frames and the sum over a complete radial MRF measurement are shown.

Even though it is often expressed that the undersampled MRF signal of a single voxel is simply a noisier version of the fully sampled time course, a caveat has to be added to this statement as the nature of *undersampling noise* and thermal noise are fundamentally different. The term *undersampling noise*, misleading as it might be, refers to all signal contributions to a voxel cause by spatial undersampling. It thus is by no means of stochastic nature but rather fully deterministic and object-dependent.

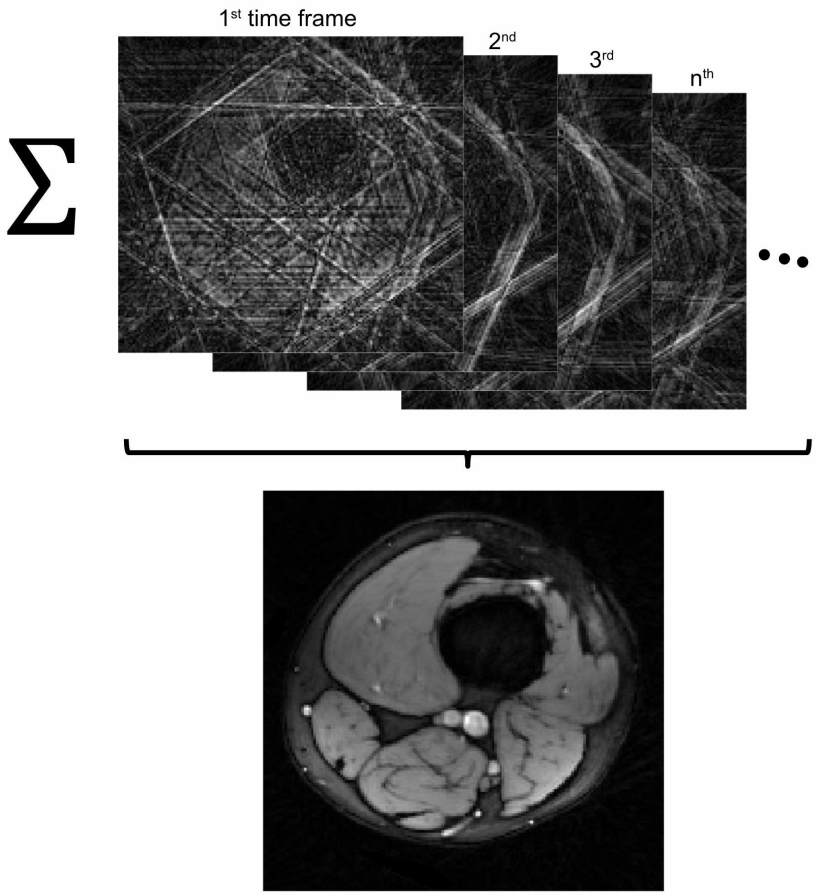

Figure 2.10: Exemplary summation over all MRF frames in a volunteer measurement of the upper leg. This example shows that the complete spatial information is contained within the MRF time series and that each fame contains a small portion of the complete information.

The thermal noise in MRI can be assumed uniform, Gaussian with zero mean in the complex image domain, and constant in amplitude throughout the measurement [28]. The amplitude of the undersampling noise is dependent on the overall signal level and the mean can in a general case not be assumed as zero when the signal levels change as in MRF. Although the mean signal contribution is usually zero with the conventional MRF patterns and the spatial oversampling, as demonstrated by fig. 2.10. This is because the changing signal levels introduce variable weightings of the k-space data, the effect of which is already discussed in section 2.2.1. A detailed discussion on the characterization of undersampling noise in MRF is beyond the scope of this work. But it has been verified that in all MRF applications shown in this work, the zero mean assumption is well fulfilled.

2.3.3 Simulation-Based Model Reconstruction

The advantages of sampling the transient signal evolution to quantify relaxation times have been explained in section 2.3.1. A seeming disadvantage is that generally no analytic solution for the signal behavior can be formulated, thus a simulation-based model is derived for the MRF reconstruction. Alleviating some of the challenges, mainly the high computational burden and high memory demand, that come from the simulation-based model is subject of current research and beyond the scope of this section [29, 30].
All timings, gradients and RF pulses played out during an MRI sequence are well-known either beforehand or after the sequence was measured, if physiological feedback is used for example. This means that the signal evolution can be computed as a function of macroscopic parameters approximating the behavior of the magnetization. The emphasis that these parameters are approximations has to be made clear. Even the quantum mechanically motivated properties of transverse and longitudinal relaxation times are approximations to describe biological tissue. No biological tissue is homogeneous in its composition and the assignment of a single parameter can only describe the average behavior at best. The choice of approximations has a significant influence on the results of the MRF experiment and the degree of detail needed for a robust and accurate quantification are still under investigation in the scientific community. Significant points of discussion, for example, is whether the effect of diffusion and chemical exchange have to be taken into account for the correct quantification of T_1 and T_2. Assuming an appropriate set of parameters x_i is selected, then a signal parameter-space (dictionary) can be spanned covering all feasible combination for a given application. Here, i is an enumerator counter over the complete set of parameters. An appropriate simulation framework has to be selected based on the x_i parameters and the signal evolution has to be computed for every parameter combination. A detailed description of the simulation framework used in this work is given in section (section 3.4.1).
The simulated dictionary D can be represented as a matrix of dimensions $N \times M$ where N is the number of signal observations and M the number of unique combination of the all parameters. The MRF reconstruction then consists of finding the entry (atom) of the dictionary which best represents the measured signal. Of course, a linear combination of atoms could be reconstructed, but this is rarely done due to the instability of the problem. A simple reconstruction can be formulated as:

$$\vec{x}_{est} = LUT(\underset{m\in[1,\dots,M]}{\arg\max}\ |\vec{s}^{\dagger}D|) \tag{2.92}$$

Here, LUT is a lookup table linking the index of every atom to its corresponding parameters, $\vec{s}$ is the measured temporal signal vector of a single voxel in image space, $\dagger$ indicates the transposed complex conjugate of a vector, and $\vec{x}_{est}$ the estimate for

the predefined parameters. This reconstruction is effectively finding the best representation of the measured signal within the dictionary via the Pearson correlation. The representation is sparse by design and thus the proposed MRF reconstruction is seamlessly integratable into a compressed sensing framework. A visualization of a simplified reconstruction process is shown in fig. 2.11.

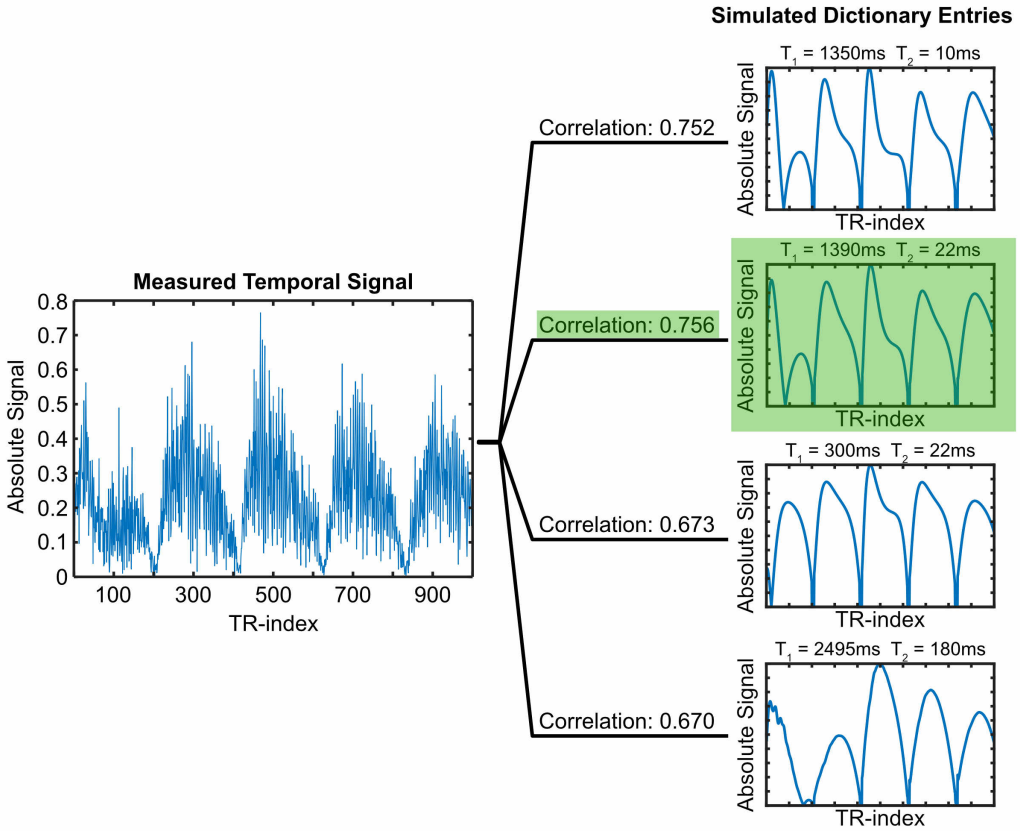

Figure 2.11: Illustration of a simplified MRF reconstruction process. The signal evolution of an actual undersampled measurement is correlated with a few dictionary atoms. The complete correlation space corresponding to this matching process in shown on fig. 2.12

Figure 2.11 displays the absolute signal time course of an undersampled MRF measurement. Further, the correlation to example atoms of the dictionary are shown and the best match is highlighted in green. The relatively small change in the correlation, relative to the change in T_2, can be seen when comparing the correlation the first and second atom. Here, T_2 changes by 12 ms, but the correlation only changes in the third decimal place. The complete correlation space corresponding to the time course shown in fig. 2.11 to a T_1 and T_2 dictionary is shown in fig. 2.12.

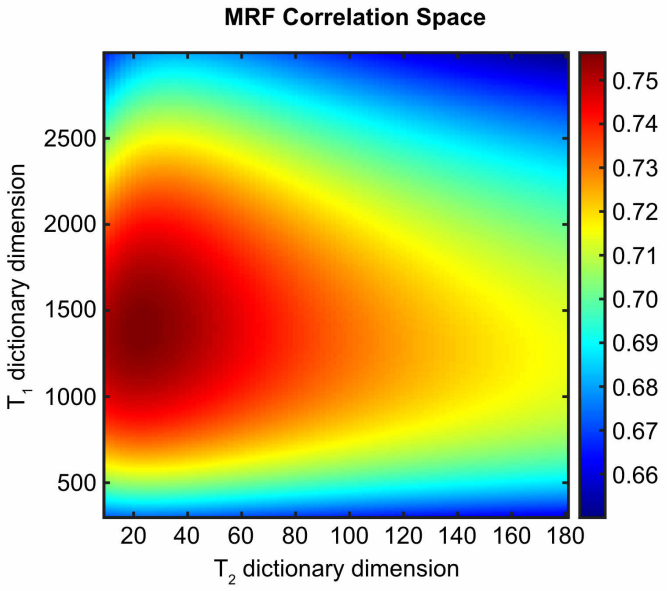

Figure 2.12: A 2D correlation space spanning a large range of T_1 and T_2 values is shown. The measured signal time course which was used to calculate the correlation to dictionary entries is shown in fig. 2.11.

Figure 2.12 shows that the correlation space is smoothly varying over the range of relaxation constants. It is thus unlikely that a *completely* wrong set of relaxation constants is quantified, even in conditions of high noise.

The main drawbacks of this dictionary based method are the sometimes lengthy computation times of the dictionary, the finite sampling steps of the parameter space, and the high memory demand of the dictionary, which can easily reach tens of gigabytes. All of these challenges have been investigated in many ways in the current research, to a point where the challenges are rarely prohibitive but rather an inconvenience for the given MRF application. The finite resolution of the dictionary and the high memory demand, for example, were tackled by hierarchical searches [31] and *through dictionary fitting* [32], both are exploiting the smoothness of the correlation space. The long computation times have been addressed by highly optimized GPU simulation frameworks [6] and neural networks [33], keeping in mind that the computation of the dictionary has usually to be performed only once. Nevertheless, constructing an MRF sequence such that the dimensionality of the parameter space needed to describe the signal evolution is small, has many benefits beyond the lower computational burden. It is expected that an increased number of parameters is accompanied by a reduction in the fidelity of the quantification due cross-correlation between parameters.

2.4 Flow and Turbulence

In theory, NMR not only allows the measurement of the spatial distribution of the magnetization but also the distribution of motion states such as velocity, acceleration, jerk and so on. A phase proportional to each of these can be applied by multi-polar gradient schemes, as described for the zeroth and first gradient moment in section 2.2.2. Applying a phase linearly proportional to velocity or higher order terms allows these distributions to be probed by conventional phase encoding techniques as described in section 2.2.1 [34]. Although interesting, the measurement of acceleration and higher orders of motion becomes increasingly more difficult as the needed gradient schemes become longer and more sophisticated. This section will thus only discuss the velocity distributions but a more general application is possible.
The distribution $s(v_i)$ of a velocity component v_i, with i enumerating of the spatial dimensions, can be sampled by probing the velocities with different velocity encodings $k_v = \gamma m_1$. The complex measurement signal is then given by:

$$S(k_v) = Ce^{i\varphi_0} \int_{V_i} s(v_i) e^{-ik_v \cdot v_i} \mathrm{d}v_i \tag{2.93}$$

Here, C is a real scaling constant and φ_0 a phase offset. As in standard imaging, a Fourier transform allows the velocity distribution to be retrieved. This method is called Fourier velocity encoding (FVE) [34] but requires prohibitively long acquisitions time and large bipolar gradients.

The velocity distribution is especially interesting in regimes of turbulent flow. A velocity vector field of turbulent flow $\vec{v}(\vec{x}, t)$ can be split into a mean and fluctuating part:

$$v_i = \overline{v_i} + v_i' \tag{2.94}$$

Again, i indicates a spatial direction, $\overline{v_i}$, is the averaged velocity and v_i' is the fluctuating part with zero mean. This splitting is often termed Reynolds decomposition. Conventional phase contrast (PC) MRI measures $\overline{v_i}$, the averaged velocity component. Finite fluctuating velocity components are a characteristic feature of turbulent flow.

The fluctuating velocity components cannot be measured directly by MRI because the measurement process inherently averages over a finite spatial and temporal domain. We thus consider the Reynolds averaged Navier-Stokes equation for incompressible fluids [35]:

$$\rho \left[\frac{\partial \overline{v_i}}{\partial t} + \overline{v_j} \frac{\partial \overline{v_i}}{\partial x_j} \right] = -\frac{\partial p}{\partial x_i} + \frac{\partial}{\partial x_j} \left(\mu \frac{\partial \overline{v_i}}{\partial x_j} - \rho \overline{v_i' v_j'} \right) \tag{2.95}$$

Here, i and j represent different spatial directions, p the pressure, $\frac{\partial}{\partial x_i}$ a spatial derivative, ρ the density and μ the dynamic viscosity. The last term in eq. (2.95), $\rho \overline{v_i' v_j'}$, shows

proportionality to the fluctuating velocity components, which describe the turbulence. The term $\rho\overline{v_i'v_j'}$, however, is Reynolds averaged, which makes this quantity measurable through MRI. This term effectively represents a covariance matrix of the velocity fluctuations, which is called the Reynolds stress tensor [35] in the following:

$$\tau_{ij} = \rho\overline{v_i'v_j'}, \tag{2.96}$$

Why this tensor represents stress, is not immediately clear, however, it appears in conjunction with the viscous normal and shear stress term $\mu\frac{\partial\overline{v_i}}{\partial x_j}$.

To reduce the acquisition time needed to estimate $\rho\overline{v_i'v_j'}$, assumptions on the shape of the velocity fluctuation have to be made. Experimental evidence with FVE, [36], indicates that the assumption of a Gaussian velocity distribution is a good approximation. This assumption is confirmed by the use of a Gaussian-model by numerous publication [37, 38, 39, 40]. Nevertheless, the effects of finite skewness and kurtosis in some flow conditions have been shown [41]. The Gaussian-model is assumed in the following as it highly simplifies the description of the signal intensity of the velocity-encoded images. The potential effects of higher central moments of velocity distribution are discussed in a later sections.

For convenience and incompressible fluids, another definition of the Reynolds stress tensor is often used:

$$\tau_{ij} = \overline{v_i'v_j'}. \tag{2.97}$$

This definition is also used in the later sections of this work. The assumption of a Gaussian velocity distribution means that τ effectively represents the covariance matrix of a multivariate normal distribution, which can be probed by finite velocity encodings. A more detailed description of the used methods can be found in section 3.2.3. A schematic illustrating the distribution and the signal dephasing in the presence of velocity encodings is shown in fig. 2.13. The voxel indicated by the blue square in fig. 2.13a is located in the boundary between a velocity jet and almost stationary fluid, which promotes the formation of turbulent flow in this region. This voxel will display a small mean velocity and the broad velocity distribution within the voxel. The latter attribute is not captured by conventional PC-MRI. The voxel indicated by the red square has a high mean velocity but the turbulent components are much smaller. Measuring the signal loss as a function of the velocity encoding moments allows the Gaussian-shaped signal dephasing to be sampled and thus Reynolds stress to be resolved within each voxel, as indicated by fig. 2.13d.

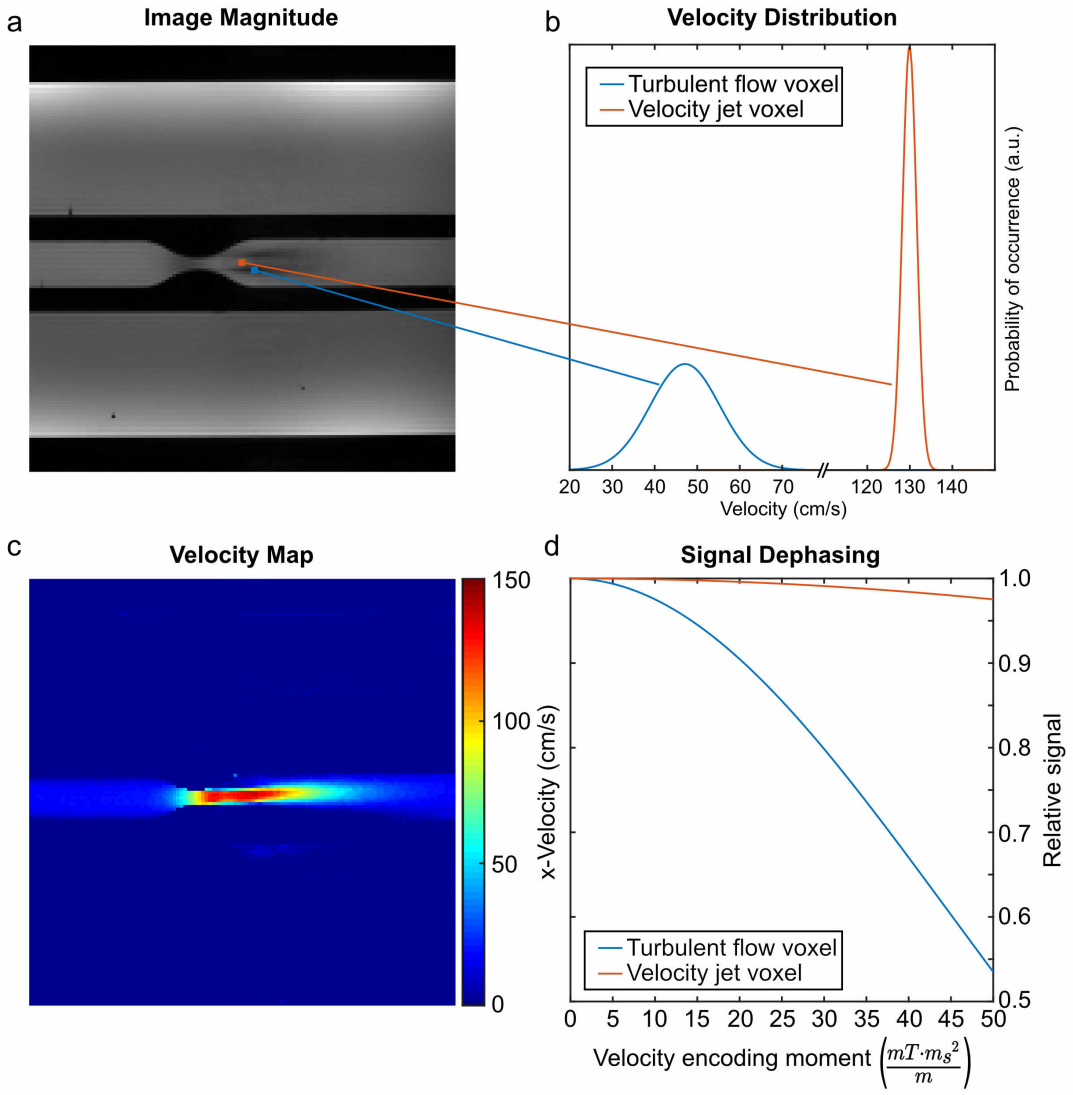

Figure 2.13: Schematic representation of intravoxel velocity distribution in laminar and turbulent flow conditions. The broad velocity distribution in the jet/slow flow boundary pixels can be guessed in the velocity encoded image in (a) by the reduction in signal. The velocity jet does not present a strong reduction in signal, indicating a small velocity distribution. The relative signal loss induced by the schematic distributions in (b) is shown in (d). The velocity map for the x-component is shown in (c).

3 Material and Methods

3.1 Hardware and Phantoms

All experiments shown in this work were performed on a whole body 7T MAGNETOM (Siemens, Erlangen, Germany). Different commercial RF coils were used to accommodate the specific phantom or regions of interest in volunteer measurement. A complete overview of the used hardware is presented in the following sections.

3.1.1 RF Coils

Both RF coils utilized in this work show a similar design as they consist of nested pairs of transmit and multi-receive coils. In both cases the outer transmit coil has a birdcage design and the inner part is composed of multiple receive-channels. The dedicated head coil from Nova Medical (Wilmington, MA, USA) has 24 receive channels. The knee coil from Quality Electrodynamics (Mayfield Village, OH, USA) has 28 dedicated receive elements. This coil has the advantage of allowing phantoms to be inserting completely as both sides of are open. This open design is especially useful in flow experiments where lengthy phantoms are preferred to allow consistent flow to established.

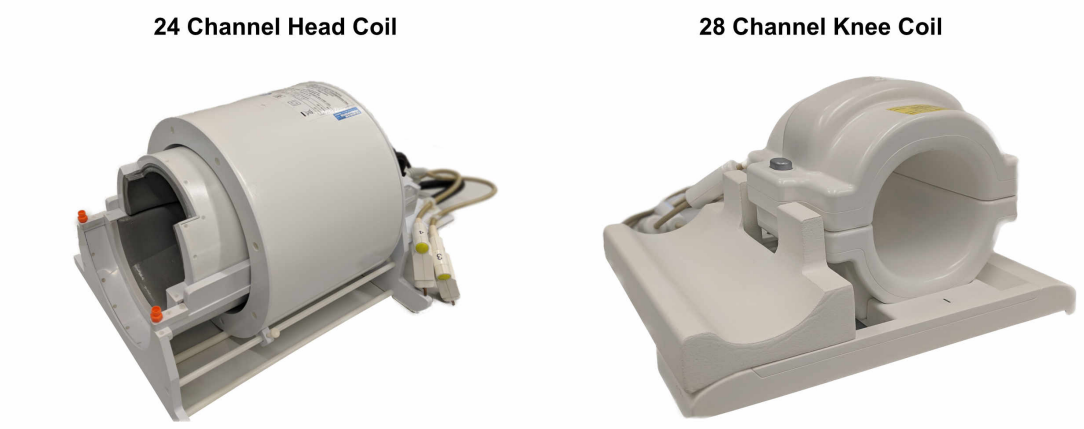

Figure 3.1: Picture of both coils used in this work.

3.1.2 Flow Pump

The flow pump used in all flow experiments is the CardioFlow 5000 (Shelly Medical Imaging, London, Ontario, Canada). This programmable gear pump can be used to generate constant and pulsatile flow. It can further be used to simulate an ECG signal allowing the synchronization between pulsatile flow waveforms and the MR system. A picture of the pump unit alongside the connective tubing is shown in fig. 3.2. This long tubing is needed because the pump is operated outside the RF cabin for safety reasons.

Figure 3.2: Picture of the CardioFlow 5000 pump unit with the operating PC and the connective tubing used to link the pump to the flow phantoms.

Even though exact temporal flow profiles can be prescribed, the elasticity of the connective tubing distorts the flow profile such that no quantitative comparison between input and measure output can be made. The behavior is nevertheless, repeatable and temporally stable allowing intrinsic comparisons between different velocity quantification sequences.

3.1.3 Phantoms

Three different phantoms were used in the experiments presented in this work, a picture and MR image for each of them is shown in fig. 3.3. All of these phantoms are in-house built and are based on agarose gel of a 0.9 % saline solution. The agarose and the physiological saline solution help to modify the electrical properties and to reduce the inhomogeneity of the B_1-field. The agarose gel is additionally doped with

a gadolinium-based contrast agent (Magnevist, Bayer Vital GmbH, Leverkusen, Germany). Both T_1 and T_2 can be influenced through the concentrations of the contrast agent (CA) and agarose gel.

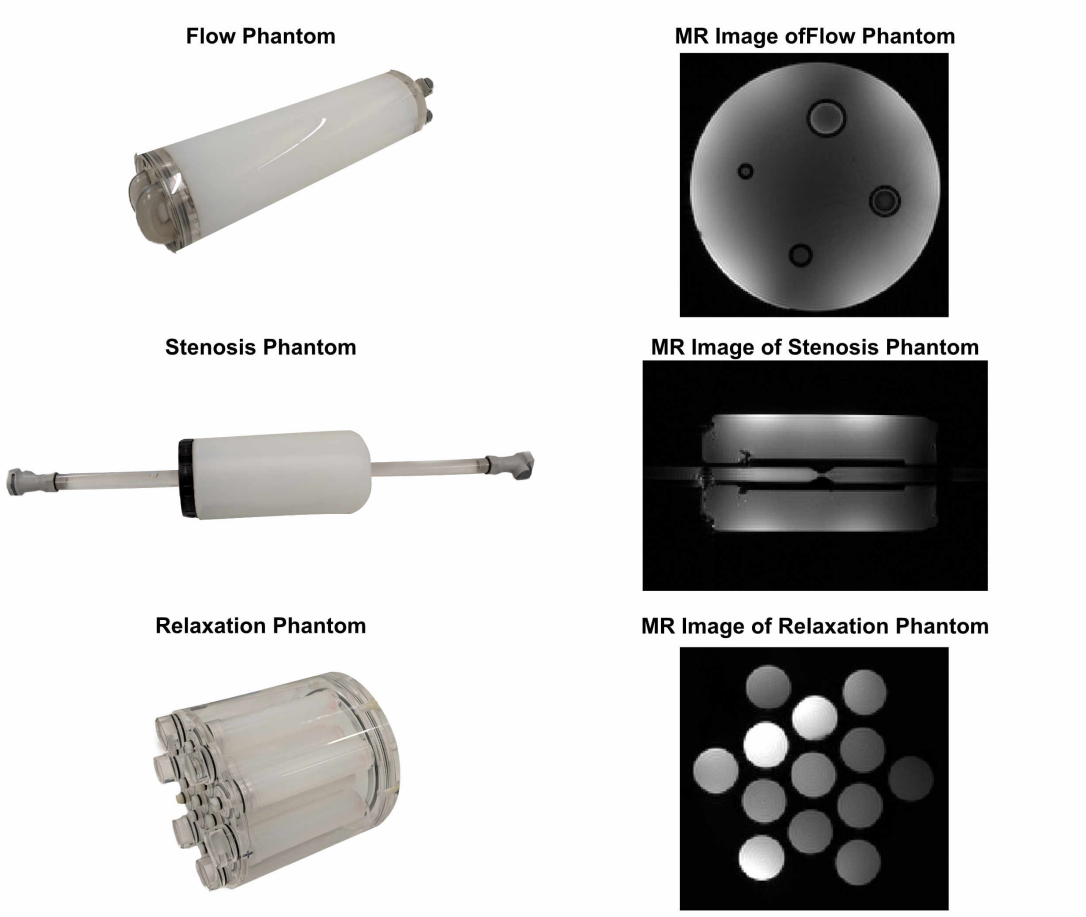

Figure 3.3: Picture and MR images of the used phantoms.

Flow Phantoms

The first flow phantom displayed in fig. 3.3 (top) consist of 4 straight pipes with different diameters (4, 8, 12 and 16 mm), embedded in an agarose gel-based phantom body with 130 mm diameter and a total length of 450 mm. Only the two largest pipes were used in experiments as they are sufficient to cover the range of physiological velocities with the pump shown in section 3.1.2. At the end of the phantom, the two larger and the two smaller pipes are connected.

The stenosis phantom is built from a long Plexiglas pipe leading into an agarose filled phantom body embedded with a 3D printed stenosis. The stenosis constricts the diameter from 15 mm to 5 mm. This phantom was used to generate turbulent flow conditions to evaluate the Reynolds-stress tensor quantification.

Relaxation Phantom

The relaxation phantom is build up of 13 individually interchangeable tubes in a phantom body which can be filled. Throughout this work, however, the phantom body remained empty to achieve a greater homogeneity in the B_1 field. The tubes were filled with varying agarose concentration and contrast agent doping to modulate both relaxation constants. The concentration for each tube is listed in table 3.1 alongside the resulting relaxation constant measured at 7 T and 3 T. These relaxation constants were measured with single echo spin echo sequences as detailed in the following section.

Tube	Agarose(%)	CA($\frac{mmol}{L}$)	T_1(ms)-7 T	T_2(ms)-7 T	T_1(ms)-3 T	T_2(ms)-3 T
1	2.0	0.0	2740±42	55±2	2463±26	61±1
2	1.5	0.25	646±4	52±2	619±3	51±1
3	1.0	0.25	662±3	102±2	631±3	105±2
4	0.75	0.25	664±5	126±3	648±3	129±3
5	1.5	0.1	1225±6	104±2	1175±3	112±2
6	1.0	0.1	1208±4	80±4	1144±3	74±1
7	0.75	0.1	1231±8	125±2	1195±4	140±3
8	1.5	0.075	1447±9	106±3	1377±3	110±2
9	1.0	0.075	1398±8	74±2	1333±5	79±2
10	0.75	0.075	1455±12	126±1	1392±4	139±3
11	1.5	0.05	1687±14	70±2	1597±8	79±2
12	1.0	0.05	1736±13	108±7	1640±8	110±2
12	0.75	0.05	1767±11	140±3	1709±9	148±8

Table 3.1: List of relaxation constant of the relaxometric phantom measured by the methods described in section 3.2.1 for both field strength 3 T and 7 T. The schematic in fig. 3.4 links the tube number to the spatial position which in the phantom.

The relaxation times are shown in table 3.1 were measured shortly after the filling of the phantom tubes. This phantom was then used over multiple years, during which the moisture content within the agarose gel change as the tubes are not hermetically sealed. The largest change in relaxation constants was during the first year after the building of the phantom (November 2016 to October 2017). The largest observed change in

T_1 was 112 ms or 5 %. The maximum change in T_2 was 13 ms or 10 %. Subsequent measurements only revealed further changes in the order of 1 %. These were caused by varying water content, effectively leading to increases in the concentration of both agarose and CA. The quantitative compassions were always done relative to the most recent reference measurement, to ensure the highest accuracy.

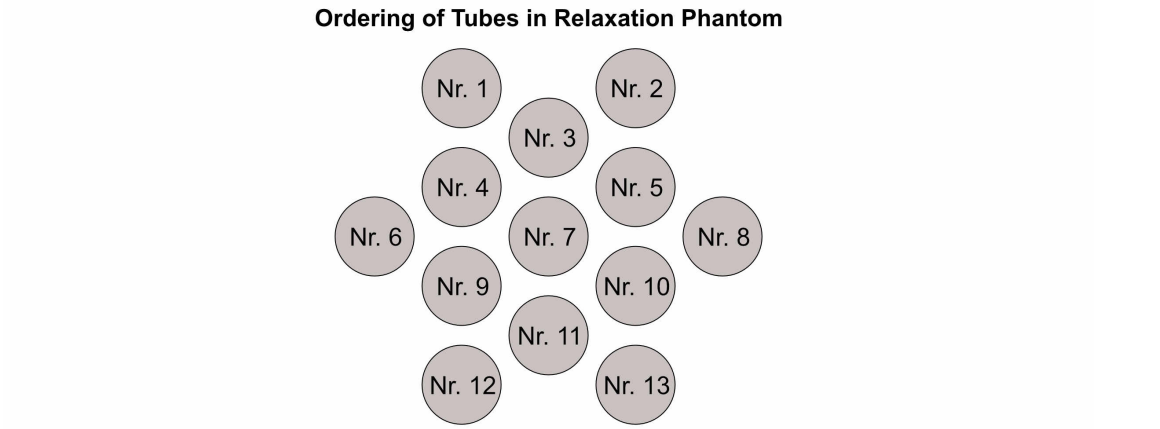

Figure 3.4: Spatial ordering of the individual tubes of the relaxation phantom as listed in table 3.1

3.2 Pulse Sequences

This section lists the sequences, and their respective signal models, used as reference measurements for the quantified parameters. These sequences were chosen foremost for their accuracy in the quantification and the required measurement time was secondary.

3.2.1 Relaxometric Mapping

The quantification of references values for the relaxation constants was performed though pixelwise least square fitting to inversion recovery spin echo data for T_1 and to spin echo data with variable TE for T_2. Only a single k-space line is acquired after each excitation to ensure a true contrast and to minimize effects of the transmit-inhomogeneity.
The inversion preparation consists of an adiabatic hyperbolic secant pulse and is assumed to achieve a perfect inversion, the spin echo readout only provides high signal and a closed form solution for incomplete relaxation at the end of the TR, even though a long TR of 5000 ms was chosen. The signal model equation can hence be written as:

$$S(t) = \left| S_0 \left(1 - 2e^{-t/T1} + e^{-TR/T_1} \right) \right| . \tag{3.1}$$

Here, S_0 is a factor incorporating all scalar influences such as the proton density and receive sensitivity, for example. This signal sampled at 9 different inversion times (TI): $\mathrm{TI} = (22,\ 59,\ 95,\ 160,\ 200,\ 400,\ 800,\ 1600,\ 3000)$ ms.
T_2 is measured by the same sequence but without the inversion preparation and TE is increased stepwise from one measurement to the next. The fitted model takes the form of:

$$S(t) = \left| S_0 e^{-t/T2} \right| . \tag{3.2}$$

The signal evolution as a function of the echo time was sampled for the following $\mathrm{TE} = (12,\ 20,\ 30,\ 45,\ 65,\ 90,\ 130,\ 180,\ 250,\ 350)$ ms.

3.2.2 B_1 Mapping

The transmit field, even though not directly quantified in this work, is required as prior knowledge to map the relaxation constants with MRF at 7 T correctly. The importance here, is the accurate quantification of the mean B_1 amplitude throughout the whole imaging slice. 2D-selective B_1 mapping sequences often use volumetric preparation pulses but inherently weight the quantified B_1 field with the excitation profile of the readout pulse.
The actual flip-angle (AFI) imaging sequence [42] does not suffer from this limitation as it is used in a slap-selective acquisition and only the center partition is evaluated

quantitatively. Further, the AFI is know to provide highly accurate B_1 maps [43]. The AFI technique consists in the encoding the B_1 information in the signal ratio of an oscillating steady state caused by an alternating TR length. Assuming a perfect spoiling, realized through high spoiling moments, then the signal can be written as:

$$S_{1,2} = M_{z1,2} e^{-TE/T_2^*} \sin(\alpha) \tag{3.3}$$

$$M_{z1,2} = M_0 \frac{1 - E_1 + (1 - E_2) E_1 \cos(\alpha)}{1 - E_1 E_2 \cos^2(\alpha)}, \tag{3.4}$$

with $E_{1,2} = e^{-TR_{1,2}/T_1}$, M_0 the equilibrium magnetization and α the excitation FA. r is defined by the ratio of S_1 and S_2 and a first-order approximation of the exponential terms yields:

$$r = \frac{1 + n\cos(\alpha)}{n + \cos(\alpha)}, \tag{3.5}$$

with $n = \frac{TR_2}{TR_1}$. In the first-order approximation, the influence of T_1 vanishes and the FA can be estimated by:

$$\alpha = \arccos\left(\frac{rn - 1}{n - r}\right). \tag{3.6}$$

3.2.3 Velocity and Reynolds Stress Mapping

The mechanism to encode velocities in the signal phase has been explained in section 2.2.2. To encode all three components of the velocity vector at least 4 independent encoding moments $\vec{m}_1$ must measured. The velocity can then be reconstructed directly via a phase difference or by solving a linear set of equations. Let P be a directional encoding matrix, than P may, for example, take the form of a so-called *single-sided encoding*:

$$P = \begin{pmatrix} 0 & 0 & 0 \\ 1 & 0 & 0 \\ 0 & 1 & 0 \\ 0 & 0 & 1 \end{pmatrix}. \tag{3.7}$$

Here, P be defined in the conventional gradient coordinate system. The 4 measurements are then composed of firstly a velocity compensated measurement with $m_{1,x} = m_{1,y} = m_{1,z} = 0$. The next measurement then applies a finite m_1 in x-direction, while nulling $m_{1,y}$ and $m_{1,z}$ and so forth.
The phase encoding matrix E can then be derived by:

$$E = P \cdot \frac{\pi}{\vec{v}_{enc}}, \tag{3.8}$$

with:

$$\vec{v}_{enc} = \frac{\pi}{\gamma \Delta \vec{m}_1}. \tag{3.9}$$

The vector division in eqs. (3.8) and (3.9) signifies an elementwise division. The phase for a given pixel with a velocity $\vec{v}$ is then given by:

$$\phi = E\vec{v} + \phi_0, \tag{3.10}$$

where ϕ_0 is a constant offset phase. Also commonly used is the *two-sided encoding*, which has the following P matrix [44]:

$$P = \frac{1}{2} \begin{pmatrix} -1 & -1 & -1 \\ +1 & -1 & -1 \\ -1 & +1 & -1 \\ -1 & -1 & +1 \end{pmatrix}. \tag{3.11}$$

In both cases, the velocity can be directly obtained by subtracting the first encoding from all three others. In case of more complex encoding matrices, this linear problem can be solved by a Moore-Penrose pseudoinverse for example.
The PC cine utilized in this work uses a single-sided encoding scheme. Here, the velocities are encoded sequentially, meaning that consecutive TRs encode different velocity components and only after the 4 velocity encodings is the next time frame acquired.

The quantification of the 6 components of the Reynolds stress tensor requires at least 7 measurements. For the quantification of the complete Reynolds-stress tensor, the following directional encoding matrix was used as proposed by Haraldsson et al. [37]:

$$P = \begin{pmatrix} 0 & 0 & 0 \\ -\frac{1}{\sqrt{1+\psi^2}} & 0 & +\frac{\psi}{\sqrt{1+\psi^2}} \\ +\frac{1}{\sqrt{1+\psi^2}} & 0 & +\frac{\psi}{\sqrt{1+\psi^2}} \\ -\frac{\psi}{\sqrt{1+\psi^2}} & +\frac{1}{\sqrt{1+\psi^2}} & 0 \\ -\frac{\psi}{\sqrt{1+\psi^2}} & -\frac{1}{\sqrt{1+\psi^2}} & 0 \\ 0 & +\frac{\psi}{\sqrt{1+\psi^2}} & +\frac{1}{\sqrt{1+\psi^2}} \\ 0 & -\frac{\psi}{\sqrt{1+\psi^2}} & +\frac{1}{\sqrt{1+\psi^2}} \end{pmatrix}, \tag{3.12}$$

with the $\psi = (1+\sqrt{5})/2$ the golden ratio. The Gaussian signal decay model can be formulated as a linear system by the following definition:

$$\vec{k}_v = \gamma \begin{pmatrix} m_{1,x} \\ m_{1,y} \\ m_{1,z} \end{pmatrix}. \tag{3.13}$$

The Reynolds stress tensor links $\vec{k}_v$ to the signal loss in the following manner:

$$\vec{k}_v \tau \vec{k}_v^{\intercal} = -2\ln\left(\left|\frac{S(\vec{k_v})}{S(0)}\right|\right). \tag{3.14}$$

Here, $\vec{k}_v^{\intercal}$ is the transpose of the encoding vector defined in eq. (3.13), τ the Reynolds stress tensor defined in section 2.4, $S(\vec{k_v})$ is the velocity encoded signal, and $S(0)$ the signal of a velocity compensated measurement. Equation (3.14) can be rewritten as:

$$\begin{aligned}\begin{pmatrix} k_{x,1}^2 & k_{y,1}^2 & k_{z,1}^2 & k_{x,1}k_{y,1} & k_{x,1}k_{z,1} & k_{y,1}k_{z,1} \\ k_{x,2}^2 & k_{y,2}^2 & k_{z,2}^2 & k_{x,2}k_{y,2} & k_{x,2}k_{z,2} & k_{y,2}k_{z,2} \\ \vdots & \vdots & \vdots & \vdots & \vdots & \vdots \\ k_{x,N}^2 & k_{y,N}^2 & k_{z,N}^2 & k_{x,N}k_{y,N} & k_{x,N}k_{z,N} & k_{y,N}k_{z,N} \end{pmatrix} \begin{pmatrix} \tau_{xx} \\ \tau_{yy} \\ \tau_{zz} \\ \tau_{xy} \\ \tau_{xz} \\ \tau_{yz} \end{pmatrix} \\ = \begin{pmatrix} -2\ln\left(\left|\frac{S(\vec{k}_1)}{S(0)}\right|\right) \\ -2\ln\left(\left|\frac{S(\vec{k}_2)}{S(0)}\right|\right) \\ \vdots \\ -2\ln\left(\left|\frac{S(\vec{k}_N)}{S(0)}\right|\right) \end{pmatrix}\end{aligned} \tag{3.15}$$

Each row in eq. (3.15) represents the data of one of the N velocity encoded measurements. This set of linear equations can easily be solved numerically.

3.3 MRF Sequence

The original MRF sequence published by Ma et al. [7] was based on a bSSFP sequence because of the long transient response and its dependence on both T_1 and T_2, as was shown in fig. 2.8. The dependence of the bSSFP signal evolution on local off-resonance was a drawback, which motivated the use of a FISP-based MRF sequence. Successful quantification of both T_1 and T_2 with a fully spoiled sequence was first shown by Jiang et al. [8]. The robustness of this sequence against variation in ΔB_0 made this sequence preferable for uses at ultra high main magnetic fields. The MRF sequence developed in this work is directly based on the FISP-MRF sequence published by Jiang et al. and a same FA and TR pattern were used as a staring point. The FA and TR pattern introduced by Jiang at al. are shown in fig. 3.5

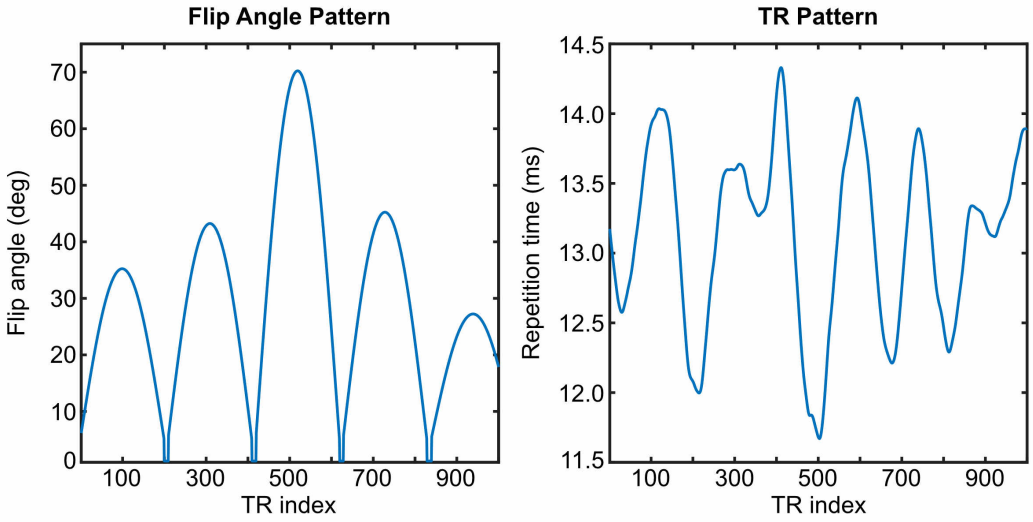

Figure 3.5: FA and TR pattern as proposed by Jiang et al. [8]. The TE is constant and minimal in their experiments.

Both type of MRF sequences used spiral readout, sampling k-space sufficiently dense to allow a time frame to be reconstructed from a single spiral acquisition. This is called a single-shot sequence. Already the original MRF publication used a multi-shot approach to acquire a fully sampled data set. The different shots are then separated by a sufficiently long waiting period, such that the magnetization is approximately in the thermal equilibrium before the beginning of the next shot. The first change made in this work to the sequence proposed by Jiang et al. was the replacement of the spiral readout trajectory with a radial trajectory. This reduced the k-space coverage per short but allowed higher resolutions to be reached, while maintaining a short

readout duration. This change required the use of a multi-shot sequence to acquire sufficient spatial information. It was found that for the consistently used nominal resolution of $0.83 \times 0.83 \times 5$ mm, 5 radial projections per time frame allowed a robust mapping of both T_1 and T_2. The pause for relaxation was set to 8 s between shots. Further, a constant TR was used instead of a variable TR. This change is investigated in detail in chapter 4. This change resulted in a constant TE/TR of 5.91 ms and 8.94 ms respectively. The used RF-pulses are 1.92 ms long Hanning-filtered and sinc-shaped with a bandwidth-time-product of 4. The choice of RF-pulse is not essential for MRF, as long as its action is accurately modeled. The inversion preparation was achieved by an adiabatic 10.24 ms-long vendor provided slice-selective hyperbolic secant pulse.

3.4 Numerical Simulations

Numerical simulations are a central part to this work as they were used to validate performance and robustness of the proposed method and form the basis of reconstructing for the MRF data. The simulation of the relaxometric dictionary is based on the simulation of the Bloch-equations [18]. The simulation of the MRF processes involves the simulation of a realistic phantom as the noise level in MRF are object-dependent. For these simulations, knowledge of the forward imaging model is used.

3.4.1 Bloch-Simulation

The simulation of the behavior of the magnetization is achieved by discretizing time into small steps during the RF pulse. During each step, a constant RF-amplitude is assumed. Further, the simultaneous action of RF-induced rotation and relaxation is performed sequentially. The error made by the approximation of sequential action becomes negligible if the time steps are chosen on an appropriate time scale relative to the relaxation rates. In this work, for the relaxation of proton MRI at 7 T, a time step of 20 μs was found sufficient. This time step also needs to accurately sample the change in amplitude and orientation of the effective B_1 field. The simulated pulses are sinc-shaped with a BWT of 4 and a duration of 1.92 ms, making a 20 μs pulse dwell-time appropriate.

The action of the RF pulse for a single time step can be expressed as a rotation matrix R around the effective B_1 field. The resulting magnetization after rotation $\vec{M}_{i+1}$ can be express as a function of the previous state $\vec{M}_i$:

$$\vec{M}_{i+1} = R \cdot \vec{M}_i \tag{3.16}$$

The index i represents a point in time after i rotations around the effective B_1 field. Likewise, the relaxation effect when no RF pulse is present can be expressed as matrix operations:

$$\vec{M}_{i+1} = A \cdot \vec{M}_i + B, \tag{3.17}$$

with

$$A = \begin{pmatrix} e^{-\Delta t/T_2} & 0 & 0 \\ 0 & e^{-\Delta t/T_2} & 0 \\ 0 & 0 & e^{-\Delta t/T_1} \end{pmatrix} \tag{3.18}$$

$$B = \begin{pmatrix} 0 \\ 0 \\ 1 - e^{-\Delta t/T_1} \end{pmatrix}. \tag{3.19}$$

Δt is the time interval of one time-step (20 μs). The state after n time-steps can thus be written as:

$$\vec{M}_n = A_n \left(R_n \left(\dots \left(A_2 \left(R_2 \left(A_1 \left(R_1 \cdot \vec{M}_0 \right) + B_1 \right) \right) + B_2 \right) \dots \right) \right) + B_n \quad (3.20)$$

For given properties of a magnetization vector the state of the magnetization at any given point in time can be computed based on eq. (3.20). This formulation in matrix form allows the efficient computation and a GPU implementation was developed within this work to permit the efficient computation 10^5 time-steps for $3{\cdot}10^9$ independent magnetization vectors.

3.4.2 MRF Imaging Simulations

The simulation of the MRF imaging processes are based on a numerical phantom, constructed following the design of the flow phantom described in section 3.1.3 and a schematic representation of the phantom can be seen in fig. 4.8. This phantom is exclusively build up of circles and thus an analytical formula of the resulting signal intensity in k-space can be written for each compartment. This means that the phantom can be sampled by any k-space trajectory without the need to interpolate the k-space data. Each compartment is assigned a positive or negative proton density, here the negative proton density is needed to create the signal voids where the Plexiglas is located in the real phantom. The negative proton density generates a signal with a phase offset of π relative to a positive proton density. Further, each compartment is assigned all physical properties relevant for the computation of the signal evolution, such as T_1, T_2, and velocity. The signal evolutions are computed beforehand according to the known sequence scheme and only a complex scaling of the k-space signal is applied to each compartment. This simulation allows the testing of Flow-MRF under optimal conditions while allowing a realistic estimate of the noise in the time series.

4 Results

This chapter details the developments made to allow the quantification of periodic flow in laminar and turbulent conditions with MRF. The decoupling of the relaxometry and velocity quantification is explained, an indispensable prerequisite to cope with the physiological variability. Further, the advantages of an MRF-based velocity quantification approach are shown, and the flexibility in the newly introduced velocity encoding pattern is explored. Later, the potential in the quantification of the Reynolds-tensor, characterizing turbulent flow, is presented.

4.1 Signal Phase in FISP-MRF Sequences

The signal phase is commonly used to encode velocities in MRI. Here, the independent modulation of the zeroth and first gradient moment with bipolar gradients is exploited to create a signal phase proportional to space and velocity respectively, as described by section 2.2.2. Although the velocity of the magnetization is potentially encoded in the signal magnitude of an MRF experiment, in the form of the in- and out-flow behavior, this mapping is highly ambiguous and less precise than a phase based velocity quantification. For this reason, the signal phase in conventional FISP-based MRF sequences has to be investigated.

4.1.1 Signal Phase in Conventional FISP-MRF

Conventional FISP-MRF refers to the use of the same FA and TR pattern as the original FISP-MRF publication by Jiang et al. [8]. This pattern is widely used within the community and has found acceptance as a reliable choice of MRF pattern for T_1 and T_2 mapping. Both FA and TR pattern are shown in fig. 3.5.
A continuously variable TR is rarely found in standard fast GRE sequences. The impact of the variable TR on the signal phase is not immediately apparent, as the signal phase of each voxel in image space for fully spoiled sequence is usually determined by:

$$\varphi = \varphi_{RF} + \Delta B_0 \cdot TE. \tag{4.1}$$

Here, φ is the phase of each voxel, φ_{RF} the local RF phase, ΔB_0 the local off-resonance and TE the echo time of the sequence. Equation (4.1) assumes the tissue to be static otherwise velocity dependent phases are accrued, as explained in section 2.2.2. The

phase term $\Delta B_0 \cdot TE$ has been subtracted for visual clarity from the signal phases displayed in fig. 4.1. This term is constant throughout the entire MRF sequence as TE is kept constant. The rapid incidence of RF pulses excites stimulated echos and partial spin echos, as described by section 2.2.5. These echos are often termed non-FID signal paths in the EPG framework. The magnetization constituting these non-FID signal paths spends variable time in the transverse plane due to changing TR. Their signal contribution then creates the variable phase observed in fig. 4.1.
As a consequence, the signal phase is dependent on the off-resonance even though a fully spoiled sequence is used. The size of the phase variation is difficult to quantify as it is strongly dependent on relaxation times and the FA pattern. Exemplarily, the signal phase is shown as a function of the TR index for different off-resonances in fig. 4.1. For this simulation a T_1 of 1800 ms and a T_2 of 120 ms was assumed. For these parameters peak phase variation in the order of of 0.5 rad can be observed. The phase variation is not a linear function of ΔB_0. This is the result of the large number and complex interferences between non-FID signal paths.

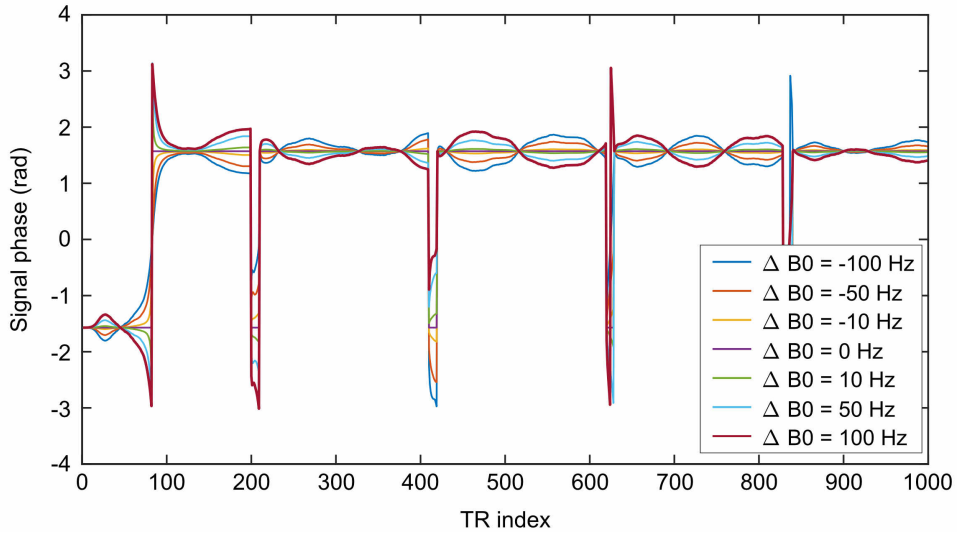

Figure 4.1: Signal phase evolution in FISP-MRF experiments with variable TR for different off-resonances is shown. A T_1 of 1800 ms and a T_2 of 120 ms were assumed in this simulation.

The sharp phase transition of π at around TR index 80 is caused by the inversion of the magnetization at the beginning of the MRF sequence. Before this point a negative z-magnetization is present, which leads to a phase offset of π in the signal. This phase transition is important for Flow-MRF and will be investigated in greater detail in section 4.2.3.

The phase discontinuities at TR index 200-210 and every 210 indices afterward are caused by a FA of 0 ° and can thus be ignored as the magnitude is approximately also zero.

ΔB_0 is usually not quantified with FISP-MRF sequences. The phase changes caused by the variable TR reduce the correlation between the measurement and the dictionary but do not change the quantified relaxation times, unless large intravoxel off-resonance distributions are present. The particular case of Lorentzian-shaped off-resonance distributions was investigated in this work [45], as these distributions represent the T_2^* dephasing. The influence on the signal magnitude as a function of different T_2^* times is shown in fig. 4.2. It is evident that these changes in the signal evolution impact the matching process beyond a simple reduction in overall correlation. Their precise effect is again dependent on many parameters, such as FA pattern, TR pattern, T_1, T_2, T_2' and dictionary coverage to name a few.

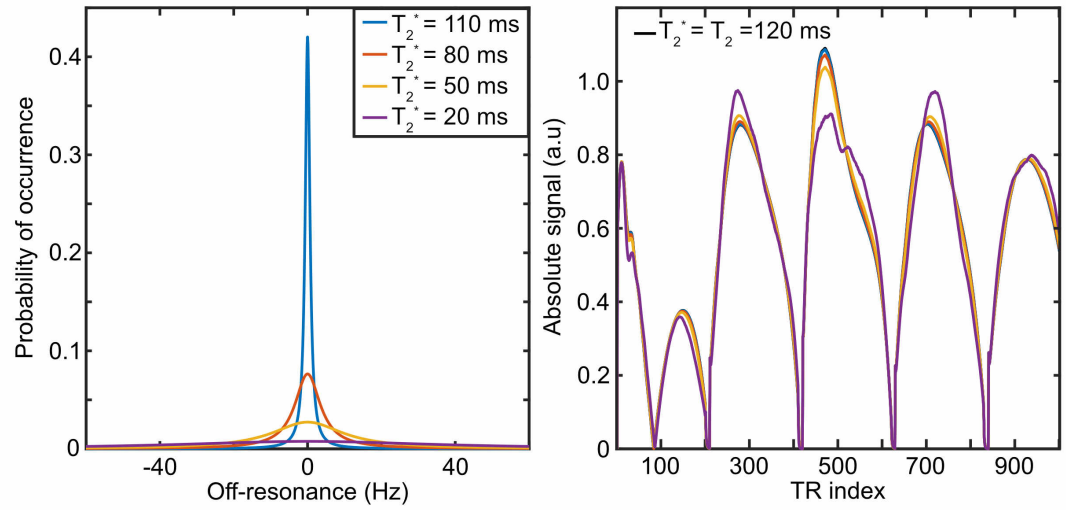

Figure 4.2: Exemplary influence of a variable TR on the signal magnitude for voxels with Lorentzian-shape intravoxel off-resonance distributions.

Besides the explained disadvantages of a variable TR, the finite phase modulation throughout the signal pattern interferes with phase-based velocimetry. In an ideal case, the phase modulation caused by the variable TR could be modeled and correct velocity quantification would be assured despite their presence. In regions of flow, the modeling of the phase modulation is further complicated by the in- and out-flow behavior, making the simulation of the signal phase unfeasible. Not only because T_1 and T_2 are unknown for flowing regions but also because the exact path of the liquid through the slice influences the resulting signal phase.

All these facts make the variable TR induced phase modulation unacceptable for phase-based velocity quantification with MRF, and a constant TR was chosen as a consequence.

4.1.2 Signal Phase in Constant TR FISP-MRF

The previous section linked the variable TR to the phase modulation present for finite off-resonances. Using a constant TR alleviates the phase modulations, which can be shown through the EPG formalism and is exemplarily shown by a simulation displayed in fig. 4.3. In this figure the real part of the signal and the corresponding phase for magnetization vectors with off-resonances between $\pm 100\,\mathrm{Hz}$ are shown. Besides the section where the FA is zero and the part of inverted magnetization, no phase modulation is present.
It remains to be shown that the relaxometric encoding capability of the MRF pattern is not reduced by fixing the TR to a constant value.

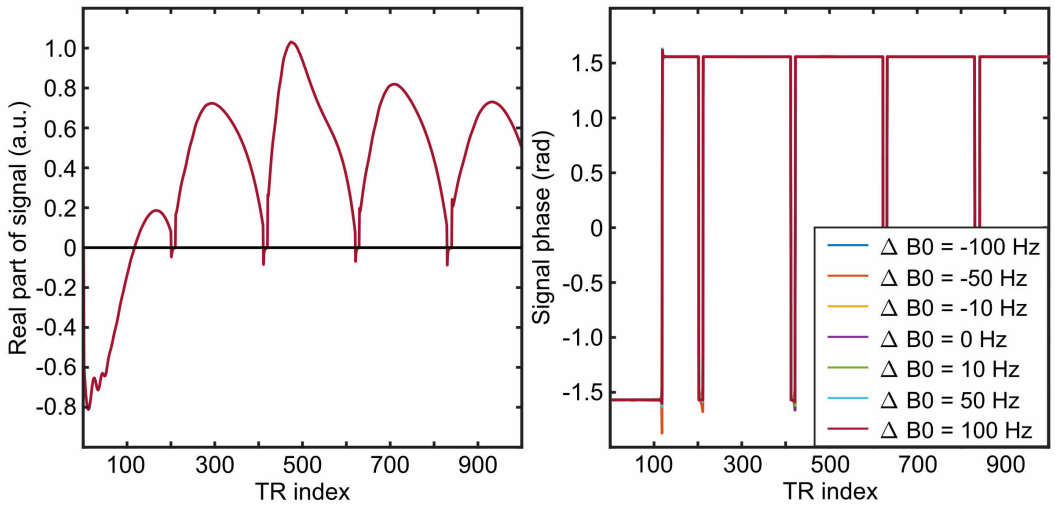

Figure 4.3: Real part of the signal and signal phase for a magnetization vectors with $\pm 100\,\mathrm{Hz}$ off-resonance during a FISP-MRF sequence with constant TR.

In general, a quantitative assessment of the encoding capability in MRF is complicated and ambiguous because the noise level in MRF experiments is dependent on the signal level. The design of appropriate metrics is still being investigated by current research [46, 47, 48, 49]. In the investigated case, however, the problem simplifies as the overall signal level remains approximately unchanged between the variable and constant TR.

The change in TR is gradual and spanning about 3 ms, which results in a change in the overall signal below 5 %. An autocorrelation matrix A can thus be used to evaluate the encoding capability [50]. Here, the mean over all elements of A, with a pure T_1 and a pure T_2 dictionary, is used as a metric as proposed by Cohen et al. [50]. The A matrices of this experiment can be seen in fig. 4.4.

$$A = |D \cdot D^{\dagger}| \tag{4.2}$$

Here, D is the given dictionary and $D^{\dagger}$ is the transposed complex conjugate of D. The mean of the correlation matrix for the given T_1 dictionary in fig. 4.4a with variable TR is 0.961, which reduces to 0.954 when the TR is fixed. For T_2 a change from 0.986 to 0.985 can be observed by the fixing of the TR. Both the metric as well as the autocorrelation plots indicate a slightly better encoding capability for the fixed TR. In conjugation with the small signal reduction due to the fixed TR, an almost identical performance in the relaxometric mapping is expected from both patterns. This result signifies that the TR can be fixed to allow a phase base velocity encoding without hindering the mapping of T_1 and T_2.

The inverted magnetization, which can clearly be seen in fig. 4.3, does present a challenge for Flow-MRF and sets a lower bound on the quantifiable velocities. This effect is investigated in detail in section 4.2.3. A change to the orignally proposed FISP-MRF sequence can be made to reduce the impact of the inversion on the velocity quantification. The non-selective inversion pulse was replaced with a slice-selective adiabatic inversion. The slice thickness of the inversion was chosen as 10 mm, twice the thickness of the excitation slice to avoid slice profile effects. The inverted magnetization in the flowing regions was assumed to wash out of the slice after approximately 50 ms and be replenished by non-inverted magnetization. Therefore, time frames covering the first 50 ms after inversion are discarded for the velocity quantification. The relaxometric mapping still used the complete information. The inversion is an indispensable part of the MRF pattern, significantly improving the quality of the relaxometric quantification. Hence, the inversion can not be removed, even though an improved velocity quantification could be achieved.

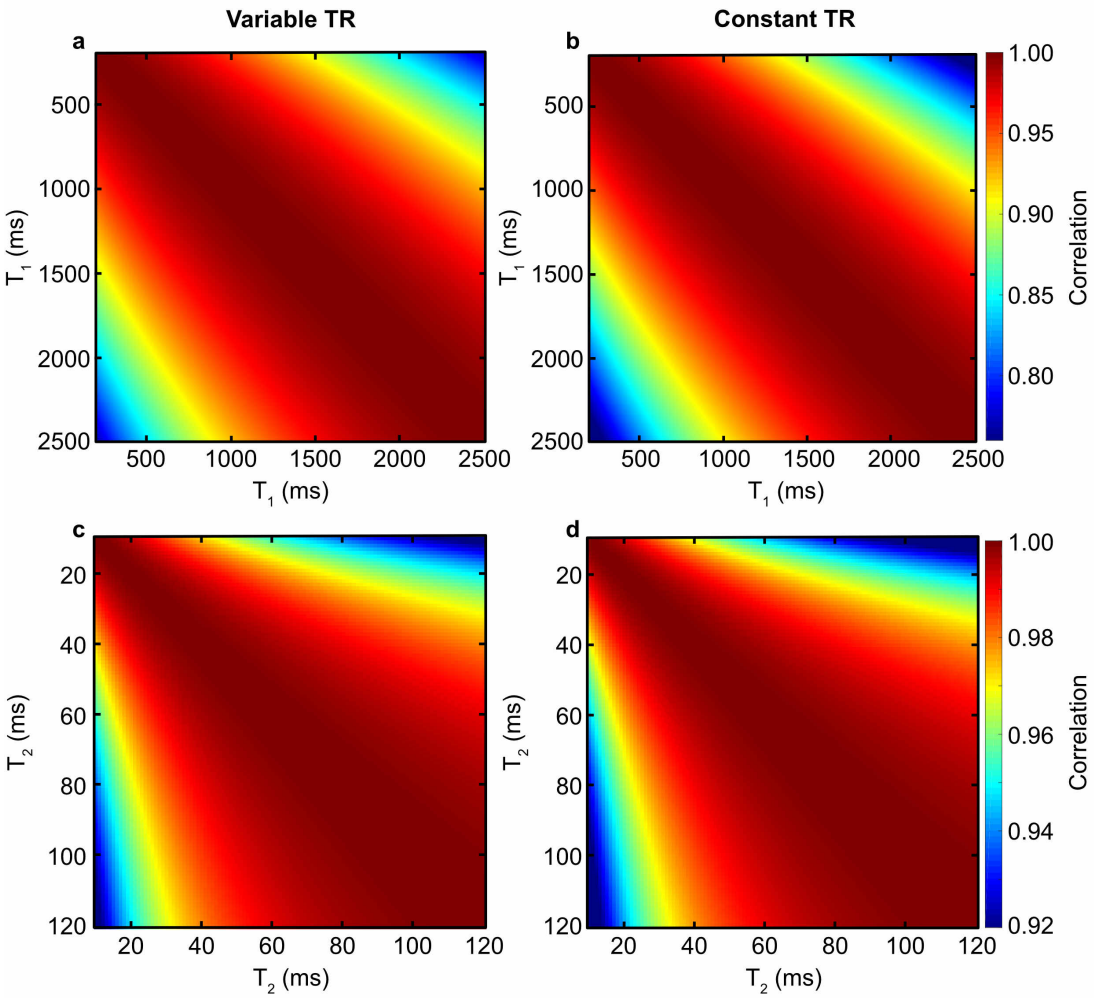

Figure 4.4: Autocorrelation plots for MRF with a variable (a,c) and constant TR (b,d) for both relaxation constants.

4.2 Phase Based Velocity Quantification Using MRF

The previous section established the observation that except for a short period at the beginning of the MRF pattern where an inverted magnetization is measured, the signal phase in flowing regions is constant. This constant phase allows velocities to be encoded by imparting additional phases to flowing magnetization. As detailed in section 2.2.2 this can be achieved by the modulation of the first gradient moment.

4.2.1 Velocity Encoding

The beginning of a Flow-MRF sequence is shown in in the sequence diagram in fig. 4.5a. The colored gradient lobes indicate the velocity encoding gradients applying well defined m_0 and m_1 values, prewinding for the radial readout and encoding the velocity. Figure 4.5b displays an $\vec{m}_1$-pattern often used in this work, the precise shape and amplitude of which is investigated and discussed in a later section.

The signal phase in image space of each voxel for a velocity-encoded Flow-MRF measurement can be expressed as:

$$\varphi(j) = \varphi_0 + \gamma \vec{m}_1(j)\vec{v}(j) \tag{4.3}$$

Here, j is the current index of the MRF pattern, φ_0 a phase offset including the phase terms of eq. (4.1), $\vec{m}_1$ the encoding moment and $\vec{v}(j)$ the velocity during the j^{th} TR. Only phases between $-\pi$ and π are observable; thus, the modulus has to be applied to the phase equation. A more convenient expression can be written in the form of a complex signal:

$$a(j) = e^{i[\gamma \vec{m}_1(j)\vec{v}(j)+\varphi_0]} \tag{4.4}$$

a has a constant magnitude of 1 and only the phase is variable. This formulation is helpful for the computationally efficient reconstruction of Flow-MRF data. Assuming the velocity to be constant, $\vec{v}(j) = \vec{v}_0$, then eq. (4.4) resembles the signal of a standard velocity encoded image. Here, it is well known that $\vec{m}_1$ has to at least assume 4 non-collinear combinations to reconstruct the 3-dimensional velocity vector uniquely. In MRF, $n = 4$ time frames are not sufficient due to the high undersampling noise. However, n has to be chosen large enough that correct velocities can be mapped, while being as small as possible to achieve the high temporal resolution. An empirical study determined that $n \approx 50$ ensures robust and good performance of the velocity quantification with MRF.
Note, in Flow-MRF all three spatial velocity directions are simultaneously encoded, and the measured phase is the sum of all three phase contributions. The individual components can be separated during reconstruction if the $\vec{m}_1$ pattern is chosen appropriately.

Time-resolved velocity quantification requires the velocity to be assumed piecewise constant and a mean velocity determined for each section. In Flow-MRF taking n consecutive time frames yields a temporal velocity resolution of approximately 500 ms, inappropriate for covering the velocity dynamics in in-vivo measurements. In cardiovascular applications the knowledge of periodic flow allows this temporal resolution to be reduced. Here, the duration of a heartbeat can be segmented in any number of parts (referred to as cardiac phases) and with each heartbeat, the time frames are assigned to their respective cardiac phase. This process can be repeated until the predefined number of frames in each cardiac phase is reached. The assignment of time frames to specific cardiac phases is based on the simultaneous recording of an electrocardiograph (ECG) or achieved via real-time feedback based on the ECG signal.

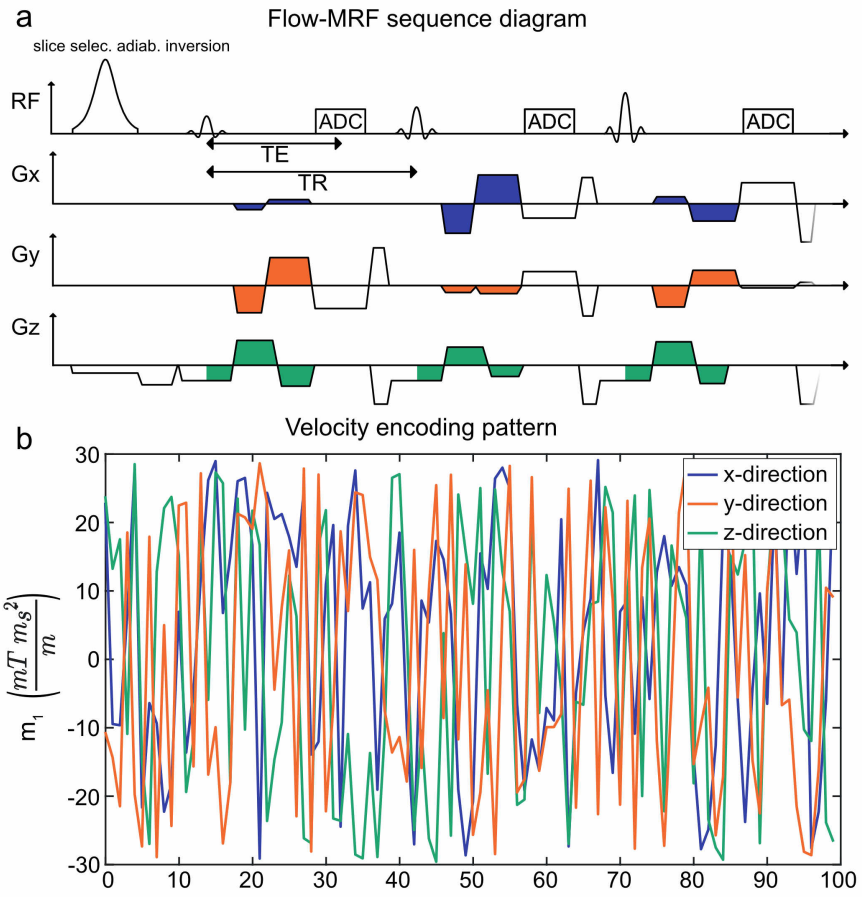

Figure 4.5: The sequence diagram in (a) shows the beginning of the Flow-MRF sequence. The colored gradient lobes indicate the velocity encoding gradients applying a well defined m_0 and m_1 on each axis. An often used $\vec{m}_1$-pattern is displayed in (b).

4.2.2 Velocity Reconstruction

It has to be restated that a precise knowledge of the signal magnitude in flowing regions is unknown, thus unlike conventional MRF, a complete signal model cannot be derived. This prohibits the use of most model-based reconstitution, commonly used in MRF. Nevertheless, the reconstruction problem can be formulated similarly to conventional velocity encoding.
Based on the n measured time frames, equations can be formulated linking the velocity to the signal as shown in eq. (4.3). The velocity could be derived very computationally efficient via a Moore-Penrose pseudoinverse for example, as can be done in standard phase based velocimetry. In Flow-MRF however, some or even all of the signal phases may be wrapped due to the accumulation of phases greater than π. Let E be the phase encoding matrix:

$$E = \gamma \begin{pmatrix} m_{1,x}(1) & m_{1,y}(1) & m_{1,z}(1) \\ m_{1,x}(2) & m_{1,y}(2) & m_{1,z}(2) \\ & \vdots & \\ m_{1,x}(n) & m_{1,y}(n) & m_{1,z}(n) \end{pmatrix}. \tag{4.5}$$

Here, $m_{1,x}(j),\ m_{1,y}(j)$ and $m_{1,z}(j)$ are the first gradient moments at the j^{th} TR on the corresponding gradient axis. Then a synthetic complex signal for a given velocity $\vec{v}$ can be calculated as:

$$\vec{a}(\vec{v}) = e^{iE\vec{v}}. \tag{4.6}$$

Likewise, a signal vector containing only the measured phase can be constructed from the general signal vector:

$$\vec{s_p} = e^{iArg(\vec{s_m})}. \tag{4.7}$$

$\vec{s_m}$ is the general signal vector, Arg calculates the argument of every entry of the complex-valued vector, meaning the angle to the positive real axis in the complex plane. Equivalently $\vec{s_p}$ can be obtained by an elementwise division of $\vec{s_m}$ by $\sqrt{\mathrm{Re}(\vec{s_m})^2 + \mathrm{Im}(\vec{s_m})^2}$. An estimate v_{est} of the velocity in a pixel can then be reconstructed by solving the following maximization problem:

$$\vec{v}_{est} = \arg\max_{\vec{v}} ||\vec{a}(\vec{v})\vec{s_p}|| \tag{4.8}$$

In other words, the magnitude of the complex-valued signal vector $\vec{s_m}$ of length n is discarded by dividing the vector by the absolute value of itself. We obtain a new signal vector $\vec{s_p}$ of length n in the form $\vec{s_p} = e^{i\varphi(j)}; j \in \{1...n\}$. The maximum correlation between the signal vector $\vec{s_p}$, which was derived from the measured data, and a synthetically generated vector $\vec{a}$ based on the velocity encoding matrix E is determined. This process identifies the most likely velocity in each pixel.

To demonstrate that in a general case this maximization problem in eq. (4.8) is not convex an exemplary correlation space is shown in fig. 4.6. The correlation between the signal vector for $\vec{v} = [0\ 75\ 0]\,\mathrm{cm/s}$ and a grid of combinations for different x- and y-velocities was calculated. Due to a large number of local maxima gradient ascent algorithms often converge without determining the *correct* velocity. Thus a two-stage reconstruction was proposed within this work, firstly the correlation of a given signal vector to a coarse 3D grid (dictionary) of velocities was calculated, similar to fig. 4.6. Here, separate local maxima were identified by a maximum filtering step, and a ranking of highly correlating maxima was established. The change in correlation within a local maximum is usually smooth and convex; thus the 5 highest correlating maxima were used as starting points for a gradient ascent algorithms.
Using exclusively a dictionary was computationally inefficient and very slow because the velocity covers a large dynamic range in the human body, subsequently leading to a high memory demand. In each direction, the dictionary would have to at least cover the velocities from $-150\,\mathrm{cm/s}$ to $150\,\mathrm{cm/s}$ with a step size preferably smaller than $0.1\,\mathrm{cm/s}$. The minimal size of the dictionary would then have $3001^3 \approx 27 \cdot 10^9$ unique entries. Such a dictionary would need 20 terabytes of memory if stored in complex double floating point precision. The coarse dictionary used to find the local maxima, on the other hand, is significantly small as the velocity resolution can be set to $5\,\mathrm{cm/s}$ or more. This resolution results in a dictionary size of $61^3 \approx 220 \cdot 10^3$ atoms or, equivalently, 180 megabytes of memory.

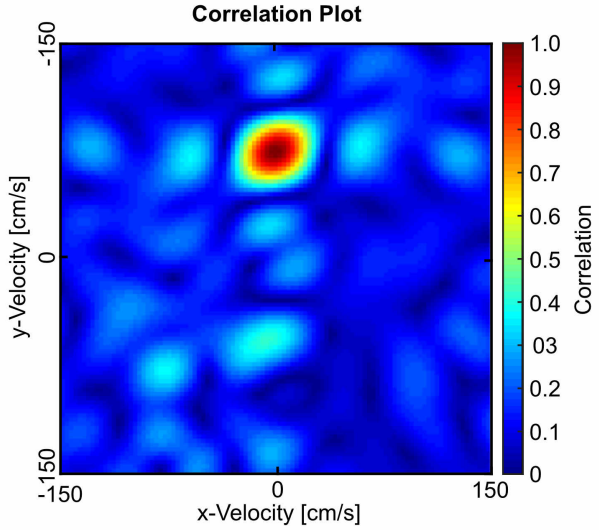

Figure 4.6: Exemplary plane from 3D velocity correlation-space. The the signal evolution of a spin ensemble with velocity of $[0\ 75\ 0]\,\mathrm{cm/s}$ is correlated to a dictionary spanning velocities from $-150\,\mathrm{cm/s}$ to $150\,\mathrm{cm/s}$ in v_x and v_y, while v_z is fixed to zero.

Reconsidering the $\vec{m}_1$ pattern shown in fig. 4.5b, the large encoding moments relative to conventional phase-based velocimetry might be noticed. The 2π periodicity in the signal phase limits, in convention phase based measurement, the maximally quantifiable velocity v_{enc}:

$$v_{enc} = \frac{\pi}{\gamma \Delta m_1}. \tag{4.9}$$

In an overdetermined system of equations as in Flow-MRF where $n \gg 4$, the velocity constraint of eq. (4.9) does not apply. This effect allows the use of a much larger spread of velocity encoding moments Δm_1 then in convectional measurements. To quantify velocities between $-100\,\mathrm{cm/s}$ and $100\,\mathrm{cm/s}$, Δm_1 can usually only be set to $11\,\mathrm{mT/m \cdot ms^2}$. In the proposed pattern of fig. 4.5b, Δm_1 spans $60\,\mathrm{mT/m \cdot ms^2}$, which equals a v_{enc} of $20\,\mathrm{cm/s}$. Nevertheless, the range of quantifiable velocities in Flow-MRF greatly exceeds $\pm 20\,\mathrm{cm/s}$ because the observed phase pattern is not periodic over this velocity range.

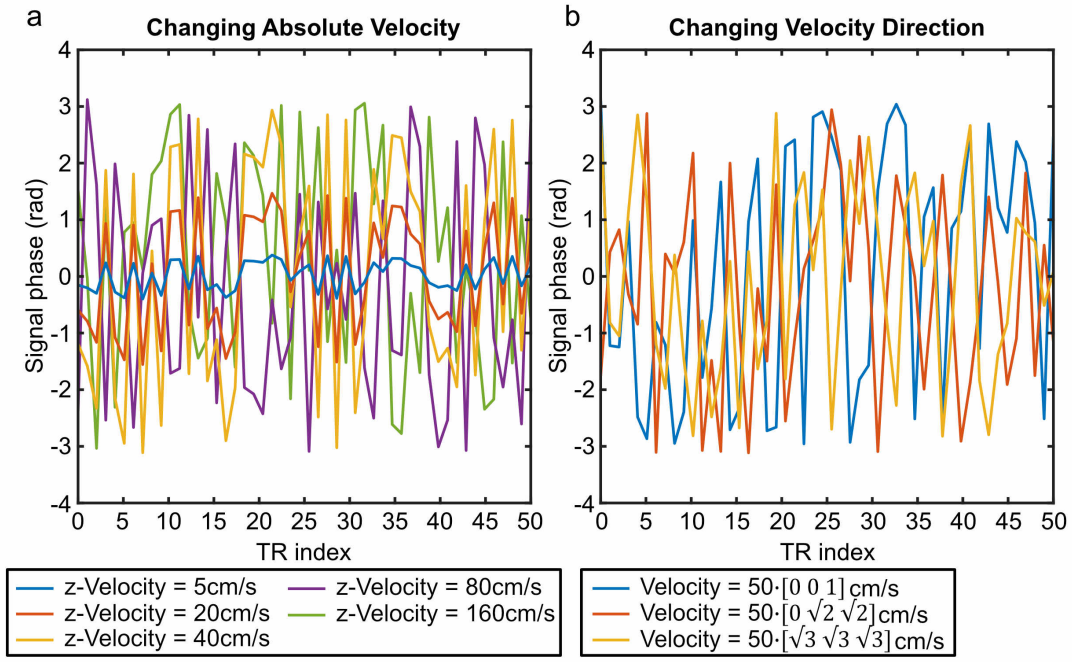

Figure 4.7: Illustration of the signal phase pattern uniqueness with respect to changes in absolute velocity and direction. The subplot (a) displays the phase pattern for a single direction as a function of increasing velocity. No phase wraps are present for the first three velocities. Higher velocities also create unique phase patterns. Changing the velocity direction while maintaining the absolute velocity likewise results in a unique phase pattern, because different noise-like m_1 pattern are used for each axis. This effect is shown in (b).

This effect is illustrated in fig. 4.7a, where the phase pattern is shown for different velocities. It can be noticed that for the first three velocities of 5, 20 and 40 cm/s, the phase pattern looks identical except for a scaling factor. For even larger velocities, some data points wrap but the overall shape is still unique. Similarly, changing the orientation of the velocity results in a unique phase pattern because different m_1 pattern are used for each gradient axis, this is shown in fig. 4.7b, allowing a discrimination of the absolute velocity as well as the spatial orientation of the velocity vector.

4.2.3 Quantifiable Velocity Range

The previous section stated the range of occurring velocities in the healthy human body to be from -150 cm/s to 150 cm/s, thus Flow-MRF should at least be able to quantify this range of velocities correctly. Further, it was motivated that Flow-MRF should be able to quantify velocities much larger than ± 20 cm/s, even with high encoding moments of $\Delta m_1 = 60\,\mathrm{mT/m \cdot ms^2}$. It remains to be tested if this assumption holds true in realistic conditions with thermal noise, undersampling, and changing signal amplitude due to the FA pattern. Likewise, the quantification at small velocities is interesting as the assumption of non-inverted magnetization becomes less valid because the magnetization is only slowly replenished by in-flowing magnetization. The range of quantifiable parameters is thus investigated in a simulation study based on an analytically defined phantom. The inflow and outflow of magnetization was modeled as well as the whole MRF imaging process. A schematic overview of this numerical phantom is shown in the upper left of fig. 4.8. The upper right plot of fig. 4.8 shows a single time frame of the simulated Flow-MRF measurement. Further, the m_1-pattern shown in fig. 4.5b and 5 projections per time frame were used.

In the presented simulation, the velocity v_{max} is purely oriented in the z-direction and varied from 0.1 cm/s to 20 m/s spanning over 4 orders of magnitude. The mean and standard deviation (SD) of the reconstructed velocity are taken as measures of quality to evaluate the performance of Flow-MRF over this range of velocities. The simulation revealed that velocities up to 840 cm/s where precisely quantifiable with a SD of 1.1 cm/s and a mean deviation below 1 cm/s. The velocity quantification beyond 840 cm/s became unstable and correct velocity values could not be determined for all pixels of the numerical phantom. Velocities below 3 cm/s were no longer distinguishable from zero due to noise. A sharp increase in the velocity noise from 3.5 cm/s to almost 100 cm/s is observed once velocities subceed 2.1 cm/s. This behavior is displayed in both lower subplots of fig. 4.8. In the double logarithmic plot, the data points where the SD exceeds the mean velocity are indicated by a black circle.

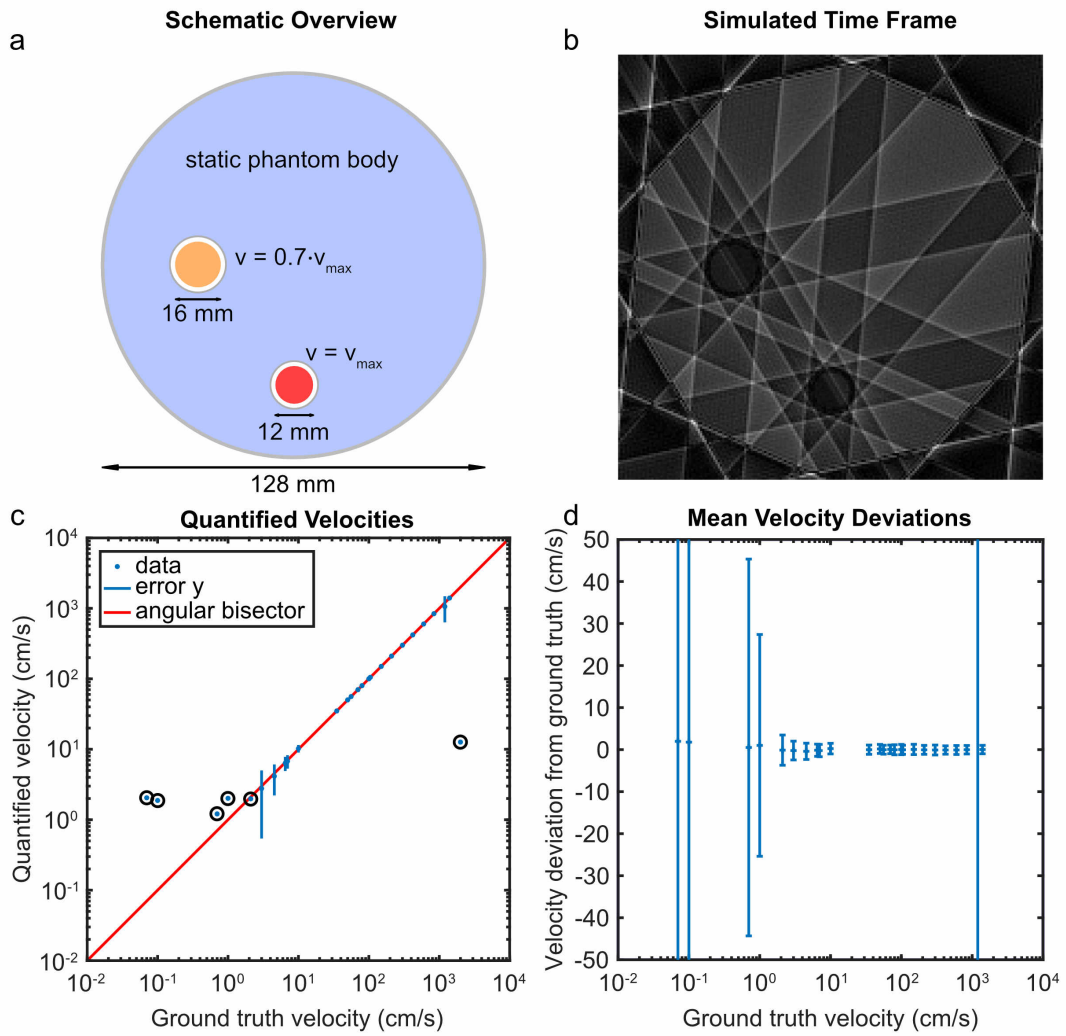

Figure 4.8: Overview of simulation results exploring the range of quantifiable velocities with Flow-MRF. A schematic of the numerical phantom alongside a single time frame of the simulated Flow-MRF sequence is shown in (a-b). The quantified velocities as a function of the ground truth are shown in a double logarithmic plot in (c). Here, the SD is indicated by the vertical lines, except for the data points where the SD exceeds the mean velocity, these are indicated by black circles. The deviation of the mean velocity to the ground truth is plotted in (d) on a semi-logarithmic scale.

4.2.4 Flow Phantom Studies

The theoretical basis of Flow-MRF was described, and its performance verified over a large velocity range in a simulation study. Nevertheless, the quantification in a real experiment has not been shown yet, which is the subject of this section. To this end, the flow phantom and pulsatile pump described in section 3.1 were used to simulate the femoral flow profile.

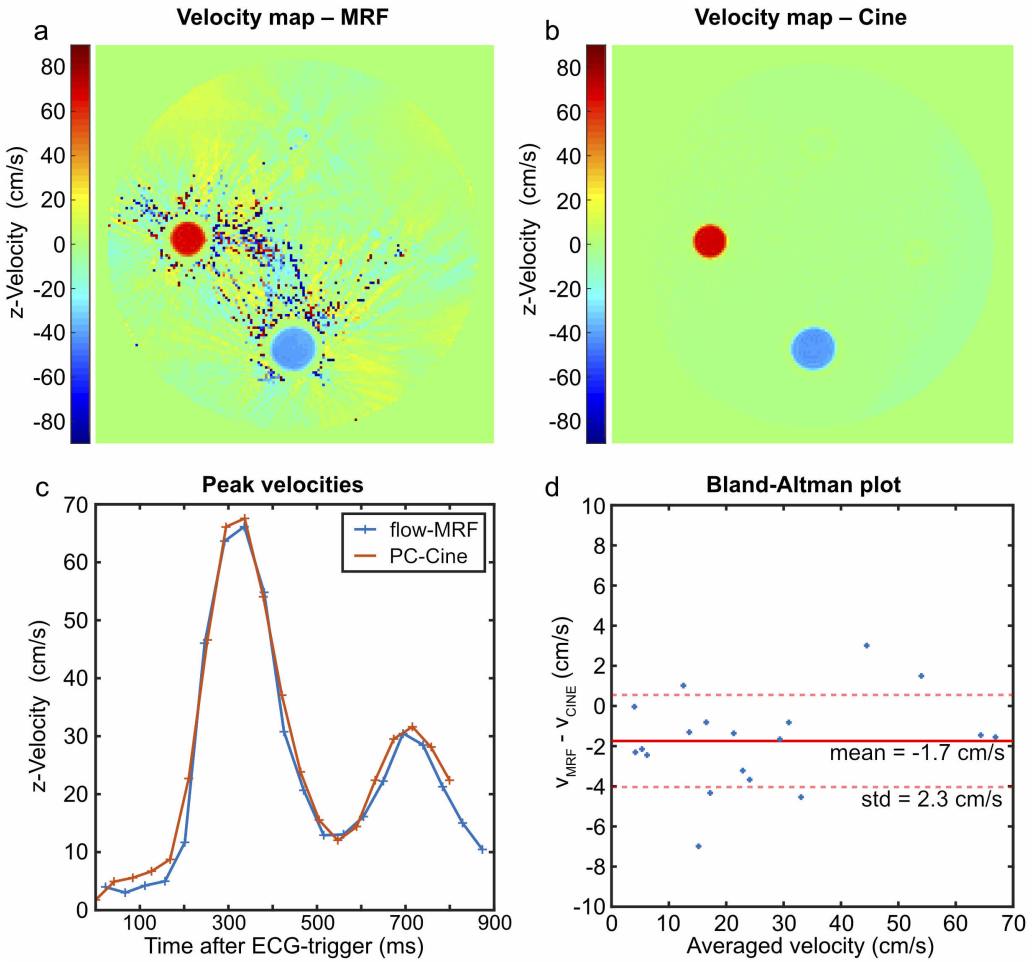

Figure 4.9: The velocity maps during peak flow for both Flow-MRF and PC cine sequence displayed (a-b). The plastic tube walls separating the flowing and static regions were masked. The mean velocities in a small central ROI in the smaller tube as a function of time is shown in (c) for both the Flow-MRF and PC cine sequence. The Bland-Altman plot corresponding to the temporal data shown in (c) between the two methods is displayed in (d).

The elasticity of the tubing connecting the flow phantom with the pump, however, distorts the flow profile to a point where no back-flow is generated. The comparison between a PC cine and the Flow-MRF sequence still allows a quantitative evaluation of the proposed method. These results are shown in fig. 4.9.
Figure 4.9a-b show the velocity maps during peak flow for both methods. The quantified velocities in the flowing regions appear similar, which is confirmed by the line plot in fig. 4.9c where the mean velocity difference between these cardiac phases is determined to below 2 cm/s. The measurement time for the Flow-MRF sequence was 84 s, which include 40 s of pauses between shots. These pauses could be used to acquire different slices, the effective measurement time per slice was thus 44 s, which is 4-fold shorter then the reference PC cine.
The velocity quantification in the static phantom body deviates more strongly, both in shape and amplitude. The background velocities of the PC cine display a linear spatial behavior and a peak velocity of 4 cm/s is measured in the static regions. This error in the quantification is likely due to the well-known effects of eddy currents and concomitant fields. A linear fit to static tissue is commonly used to correct both effects. For Flow-MRF the background velocities are not described by a linear gradient, and peak deviation of 12 cm/s is observed. The origin of these deviations are likely also eddy currents and concomitant fields, but the larger velocity encoding gradients cause them to have a higher impact. Furthermore, the radial readout complicates the spatial shape of the additional phase contributions. The lack of a simple method to correct eddy currents and concomitant fields in Flow-MRF is a drawback, but good agreement between Flow-MRF and the conventional technique could still be achieved as indicated by the Bland-Altman plot in fig. 4.9d. Here, a mean deviation between both methods was quantified as (-1.7 ± 2.3) cm/s. It can also be noted that the Flow-MRF velocity quantification fails for some pixels in the static tissue. These are located in proximity to the flowing regions, and the quantification fails here because of the elevated undersampling noise level. The flowing regions have a higher signal level because of in-flowing fully relaxed magnetization, in turn elevating the undersampling noise for the surrounding static tissue. The instability of the quantification at small velocities was discussed in the previous section.
A similar experiment to the one presented by fig. 4.9 was performed but with double oblique slice positioning relative to the z-axis, such that all three velocity components are non-zero. The velocity maps are shown in fig. 4.10 and the line plots of a central 3×3 ROI, alongside a Bland-Altman plot of the cumulative data is shown in fig. 4.11. Similar to the experiment with a flow in the z-direction, good agreement between Flow-MRF and the PC cine sequence can be seen for the flowing regions. Likewise, the same observations about the background velocities can be made. Between all three velocity components, a mean deviation of (0.17 ± 1.16) cm/s can be determined, as shown in fig. 4.11.

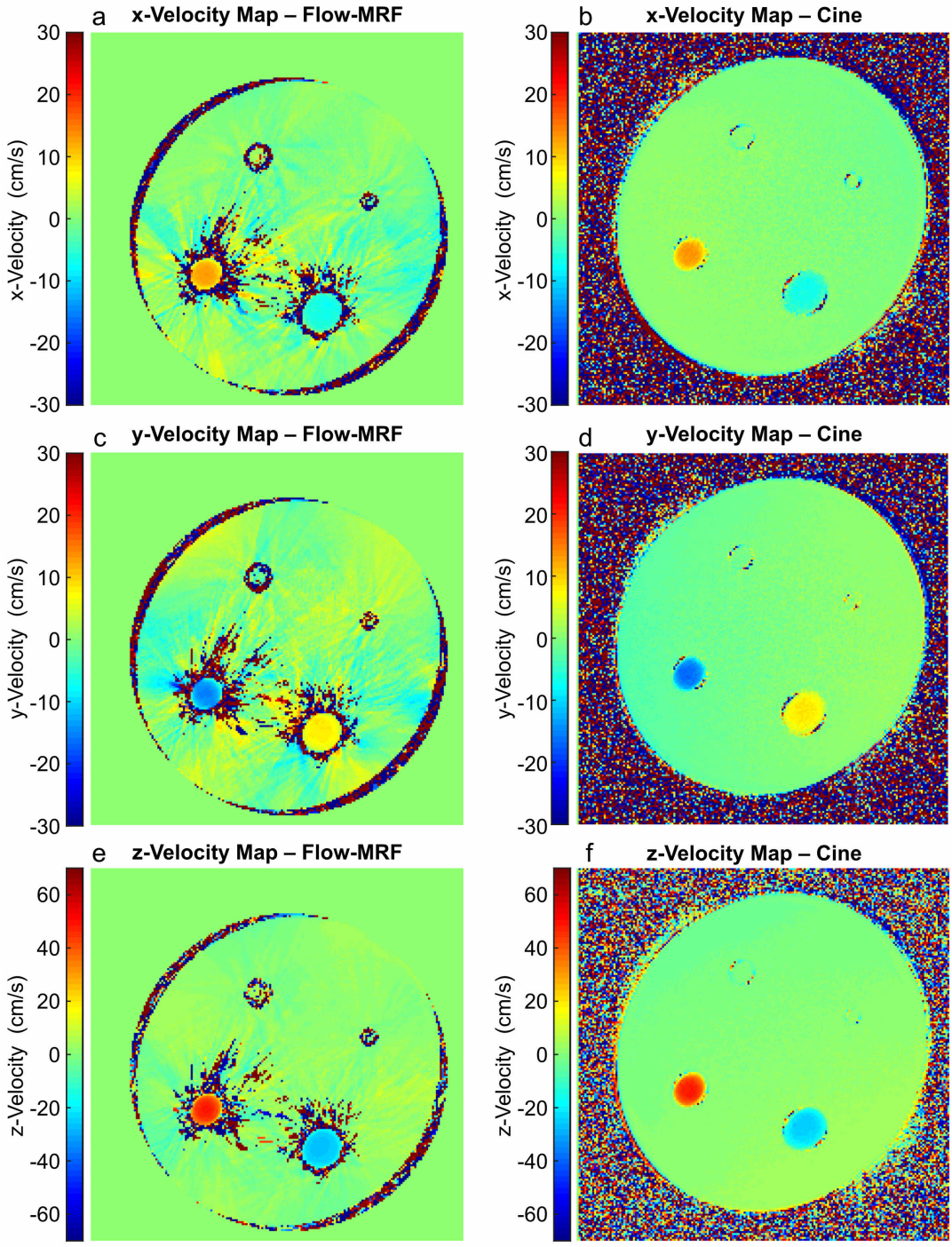

Figure 4.10: Direct comparison of velocity maps between the Flow-MRF and a the PC cine data for a double oblique measurement.

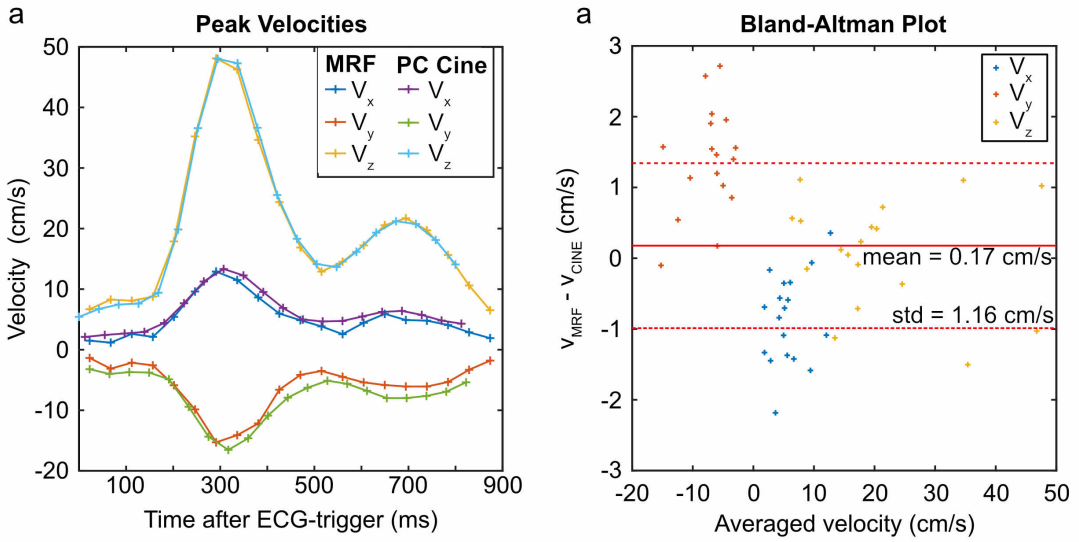

Figure 4.11: Velocity-time course of all three velocity components is displayed in (a). The corresponding Bland-Altman plot to the temporal data shown in (a) is plotted in (b).

4.2.5 Stability of Velocity Quantification

It is well known in MRI that the signal phase is much less stable than the signal magnitude. Thus in conventional PC MRI, the temporal difference between the two velocity encoded measurements is explicitly kept small, in the order of 10 to 50 ms. Temporal drifts in the signal phase then have only a minor impact on the measured velocity. In Flow-MRF on the other hand, the data used for velocity quantification spans approximately 10 s. Here, even small drifts in the signal phase, potentially caused by an unstable RF-phase or temperature drifts, have the potential to significantly influence the velocity quantification.
To investigate the influence of phase drifts in Flow-MRF, the previously shown numerical phantom was used and parasitic phase contributions added to the simulated signal. As a first order approximation, the phase drifts were assumed to be linear, which is a reasonable assumption over the considered span of 10 s. The signal phase in each TR can thus be written as:

$$\varphi(j) = \gamma \vec{m}_1(j)\vec{v} + \frac{j}{n}\theta_{max}, \tag{4.10}$$

j is again the current TR index, n the overall number of time frames and θ_{max} the amplitude of the phase drift during the Flow-MRF acquisition. Figure 4.12 displays the resulting velocity from the simulated Flow-MRF experiment as a function of the maximal phase increase θ_{max}. Two separate regimes can be observed in the quantified

velocities, if the phase increase is below a critical value (approximately 4 rad), then a small error of $-0.34\,\mathrm{cm/s/rad}$ is observed, linearly proportional to θ_{max}. Beyond this critical value, the velocity quantification fails, and no meaningful information can be drawn from the Flow-MRF data. These results are favorable for Flow-MRF as the critical regime transition value is very large. Phase increases in this order would also lead to significant image artifacts in conventional sequences. Further, the systematic error is small and below normal velocity noise levels.

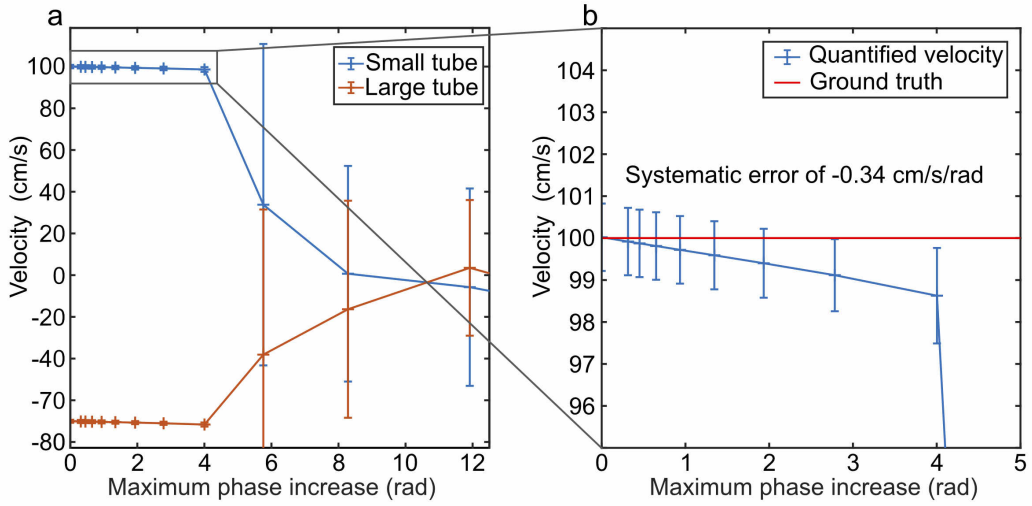

Figure 4.12: The quantified velocity as a function of the parasitic linear phase is shown in (a). Here, the mean velocity over each tube and the respective SD is displayed, illustrating the failure to quantify velocities beyond a phase increase of more then 4 rad. A zoom of the first regime is shown in (b).

The robustness of Flow-MRF against linear phase drifts might be surprising as conventional PC MRI would be strongly influenced by additional phases between velocity-encoded images. In Flow-MRF, however, the model-based reconstruction is only searching for phase patterns correlating with the ideal phase model. This ideal phase model (eqs. (4.5) and (4.6)) is solely based on the velocity encoding matrix E. As long as the parasitic phase contribution is uncorrelated with the $\vec{m}_1$ pattern, then the influence on the velocity quantification is minimal. The linear phase pattern, for example, is strongly uncorrelated with the white noise based $\vec{m}_1$ pattern shown in fig. 4.5b. Nevertheless, the linear phase reduces the overall correlation of the measurement with the ideal model until the *true* correlation can no longer be distinguished from noise, this point marks the transition between the two regimes observed in fig. 4.12.

4.2.6 Relaxometric Mapping

The performance of Flow-MRF in quantifying relaxation constants needs to be evaluated. Foremost, the influence of the bipolar gradient compared to the conventional gradient scheme needs to be investigated. To this end, two phantom experiments were performed, one comparing the relaxation constants quantified with the Flow-MRF gradient scheme to conventional MRF and secondly, an absolute comparison of Flow-MRF to spin echo based reference measurements. The quantification of relaxation constants is dependent on the knowledge of the local transmit field. In theory, this parameter can be quantified directly from the MRF data, but the reconstruction of T_1, T_2, and B_1 is not unique with the current FA pattern, resulting in an unstable quantification. To resolve this problem, either the FA pattern can be adapted [6, 51, 52] or the prior knowledge of B_1 can be included in the reconstruction. The latter option was chosen in this work.

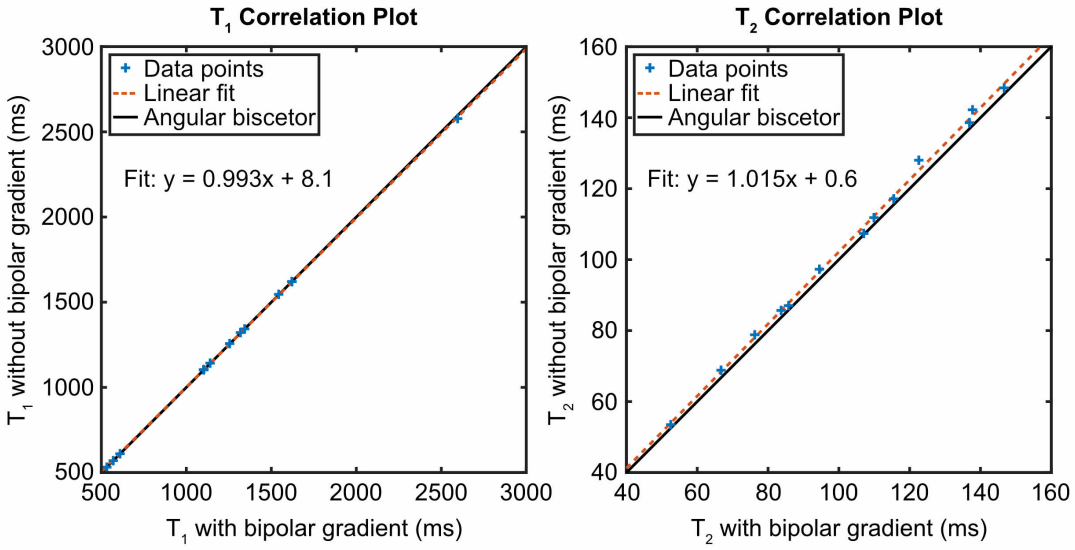

Figure 4.13: This plot illustrates the measured relaxation constants of the 13 tubes from the relaxation phantom determined by the Flow-MRF sequence and an MRF sequence with identical timings but no velocity encoding gradients.

Figure 4.13 shows the results from the MRF experiments with and without velocity encoding gradient. The differences from both T_1 and T_2 are small between the two sequences. The linear fit to the correlation plot determined a systematic deviation by $-0.7\,\%$ with an offset of 8.1 ms for T_1. The offset for T_2 is smaller with 0.6 ms, but a systematic deviation of $1.5\,\%$ could be quantified. However, these deviations are below the noise level of in-vivo measurements and thus do not introduce significant errors to the relaxometric quantification.

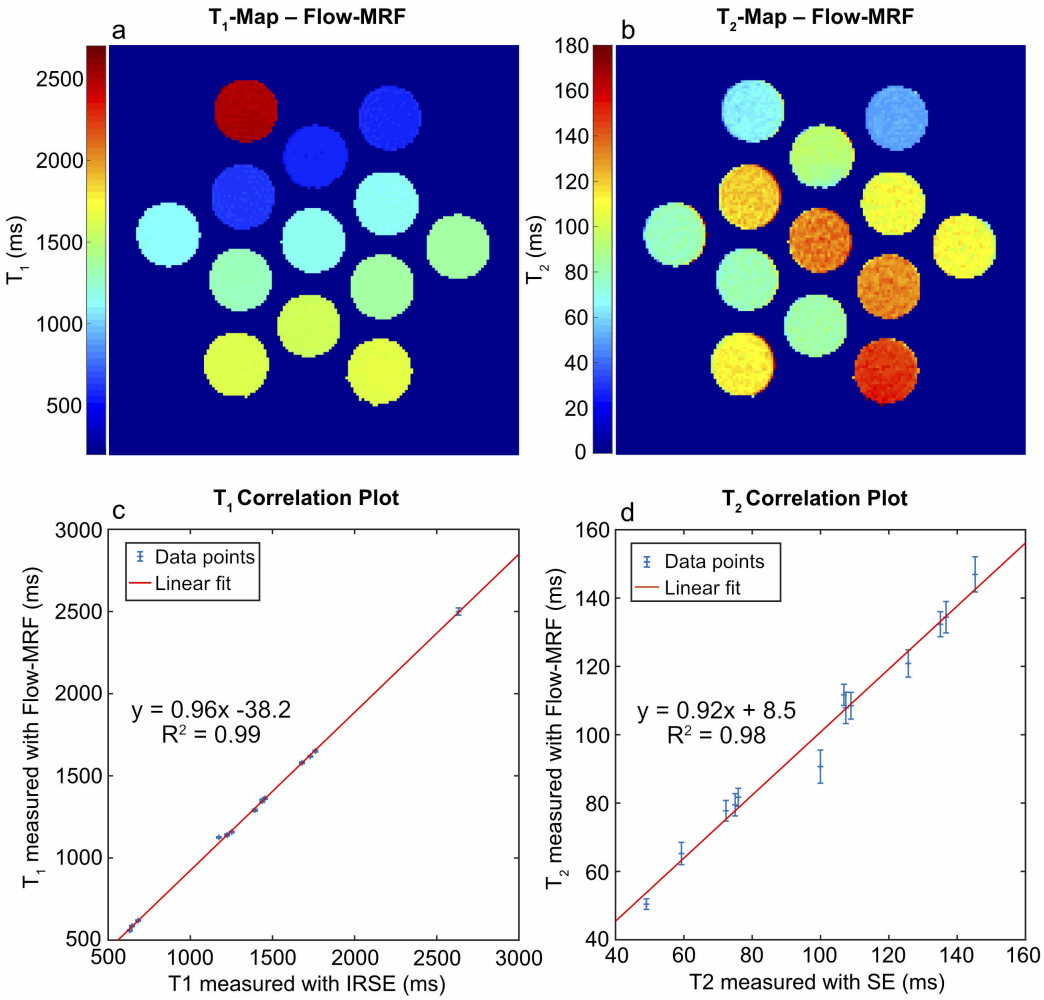

Figure 4.14: Maps of both relaxometric constants measured by Flow-MRF are shown in (a-b). The correlation plots in (c-d) compare the quantified relaxation constants of Flow-MRF with the reference measurements described in section 3.2.1.

The quantitative maps of the relaxation phantom determined by the Flow-MRF sequence are shown in fig. 4.14a-b, alongside a comparison of the determined relaxation constants relative to the reference. The maps display homogeneous relaxation constants throughout each tube, and a residual bias of B_1 is not observed. The correlation of the relaxation constants, quantified with MRF to the reference, deviates further from unity then the relative comparison between MRF with and without velocity encoding. The mean deviation between both measurements was (-89 ± 25) ms for

T_1 with a peak underestimation of 133 ms from MRF. T_2 values of MRF deviate by (0.8 ± 2.5) ms relative to the spin echo sequence with a peak deviation of -9.2 ms. The possible nature of these deviations is discussed in a later section.

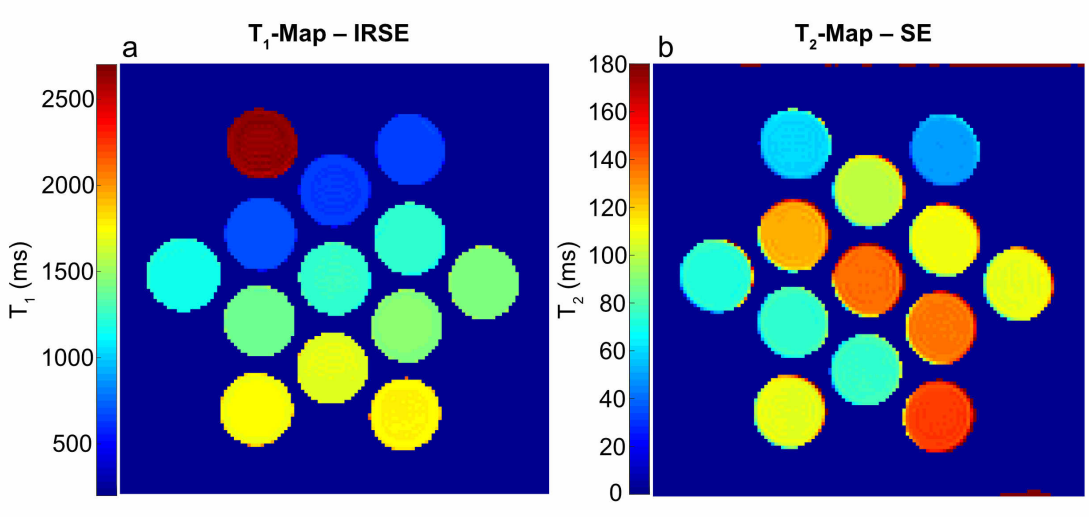

Figure 4.15: Relaxation times of the relaxometric phantom measured by the reference methods. The relaxation times were determined by least square fitting as described in section 3.2.1.

Figure 4.15 displays the relaxometric maps determined by the reference methods at 7 T. A tabular overview of relaxation times quantified in each tube is listed by table 3.1 in section 3.1.3.

4.3 Influence of Physiological Variability

One of the major challenges in the design and implementation of Flow-MRF was the stochastic variability of the heartbeat duration. Even for healthy volunteers in resting positions, the heart rate (HR) varies significantly from one beat to the next. This effect is illustrated in fig. 4.16, where the duration between R-waves (RR-interval) was recorded in two healthy volunteers while being in the MRI bore. The recorded period spans approximately 5 min, and even though the mean RR-interval is very similar between the two volunteers with 1033-1037 ms respectively, the variability is higher for the second volunteer. Here, the maximum and minimum registered RR-duration were 716 ms and 1281 ms. In Flow-MRF, where a priori knowledge of the temporal signal evolution is the basis of quantification, this variability has a significant impact. In the following section, the proposed methods to cope with physiological variability is detailed.

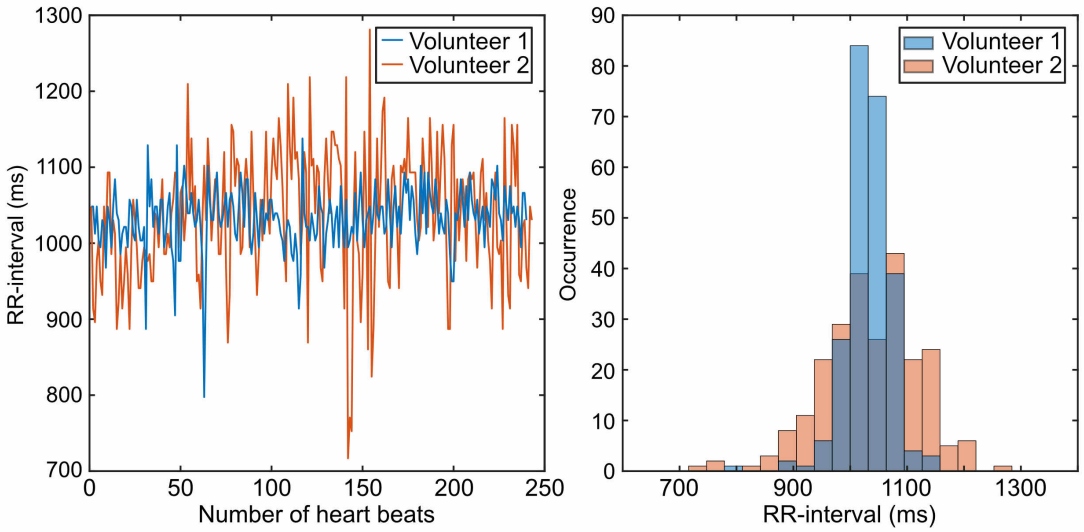

Figure 4.16: The duration of every heartbeat was recorded during an approximately 5 min long period. This time series was plotted from two different volunteers in (a). A histogram of this time series is displayed in (b).

4.3.1 Multi-Shot Flow-MRF

MRF is often used in conjunction with single-shot readout techniques. These single-shot measurements are made possible by the fairly low spatial resolution (1.2-1.5 mm inplane), the high undersampling and spiral readout covering large parts of k-space at once. The vessels in the human body, on the other hand, are mostly small structures, requiring high resolutions to estimate the blood flow accurately. This observation

motivates the choice of a high resolution (0.8 mm inplane) radial readout for Flow-MRF. As a consequence, acquiring only a single radial spoke per time frame results in an insufficient amount of spatial data to reconstruct any parameter. Thus a multi-shot approach was developed, allowing the combination of k-space data acquired sequentially into a single time frame. This multi-short implementation also enables seamless extension of Flow-MRF to volumetric coverage. To ensure that the temporal relaxometric data is identical in all shots, pauses were inserted between every acquisition-train allowing the magnetization to approximate the thermal equilibrium. The challenge with multi-shot Flow-MRF is that unlike the behavior of the magnetization, the sequence of heartbeats and thus the velocity pattern during a Flow-MRF measurement can never be reproduced due to the physiological variability.
Two assumptions have to be made to cope with the above-stated challenge of physiological variability in Flow-MRF. Firstly, the signal phase has to be independent of the FA-pattern, the validity of this assumption was shown in section 4.1.2. Secondly, the velocity profile is independent of the RR-interval. This assumption implies that the difference between a *short* and *long* heartbeat is the length of the diastole, the period where no flow is produced. The length of the heart contraction (systole) and its stroke volume must remain constant and independent of the current RR-interval. This assumption is presumed valid, and its validity discussed in chapter 5. The validity of the second assumption means that the velocity pattern is periodic, but its periodicity does not match the periodicity of the FA-pattern. The complete decoupling of the signal phase from the FA-pattern now allows reordering of the radial readouts independent of their position in the FA-pattern without affecting the encoded velocity information. This reordering or binning process is the key to cope with the physiological variability. Thus between shots, it has to be made sure that the recurring velocity profile is encoded with the same encoding moment $\vec{m}_1$, which can be achieved through real-time feedback from the physiological monitoring unit (PMU).
The beginning of each shot, and thus of each readout train, is triggered by the R-wave measured by the ECG. Hence, the FA-pattern starts alongside the first systole and both the velocity profile and the FA-pattern are synchronized for all shots. The variable length in the RR-interval means that this synchrony is lost after the second R-wave. This effect is illustrated by figs. 4.17 and 4.18. Figure 4.17 shows a schematic diagram of this process, while the measured heart rate pattern of a volunteer is shown in fig. 4.18. For the second figure, all TRs corresponding to the same cardiac cycle are colored identically after the shown color scheme. Here, the increasing dispersion with higher cardiac cycle number can be seen. The velocity encoding moments for each gradient axis is effectively stored in a 2D lookup table. The ECG-trigger at the start of the shot, sets the current index to the first column and first row. The current index is then switched in real time by 1 column from TR to TR and only the detection of an R-wave forces the index to return to the beginning of the next row. Identical

lookup tables are used for all shots ensuring that the signal phase in flowing regions is the same between all shots. Every radial spoke measured with the same index in both column and row holds the same velocity and velocity encoding information and can thus be combined into a single time frame. In general, spokes combined into a single image are not measured with the same flip angle. This results in a mixing of the magnitude information, contained in each spoke, but the phase of flowing regions remains identical between all spokes, due to the independence of phase and FA-pattern. This is again illustrated in figs. 4.17 and 4.18.

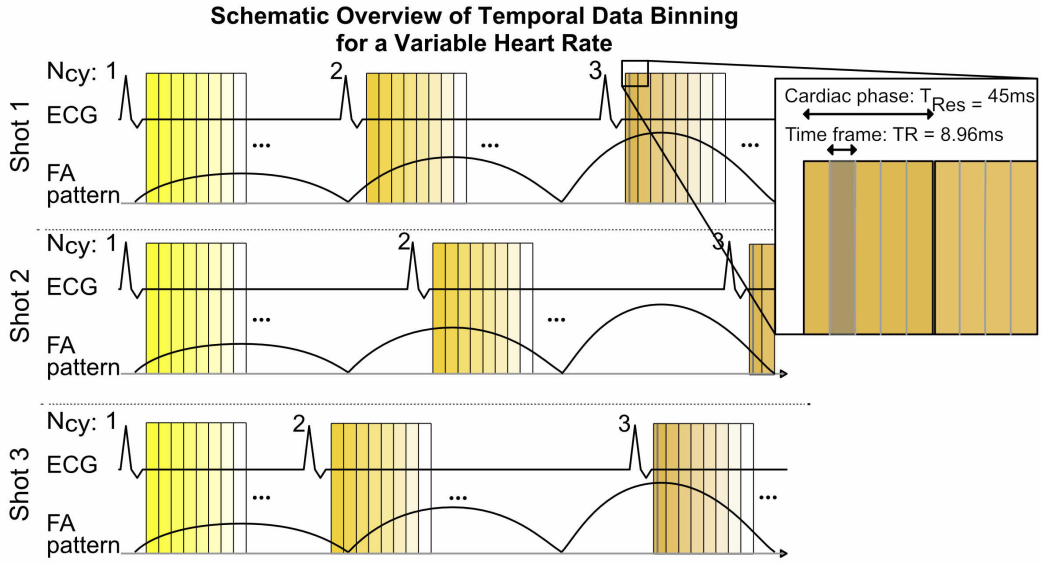

Figure 4.17: The reconstruction scheme for the velocity quantification is shown. The beginning of 3 shots is illustrated, and each colored rectangle represents a set a 5 consecutive TRs as illustrated in the zoomed section. The color of each block represents the corresponding cardiac cycle number, and the same color scheme as in fig. 4.18 was used.

Figure 4.18 shows the HR variation of a volunteer. To reconstruct a time frame within the 5th cardiac cycle, useful for the velocity quantification, a host of projections acquired at different TR-indices need to be combined as illustrated by the dark blue line in Figure 4.18. The black line at the bottom of the plot indicates qualitatively the change in FA associated with the different TR-indices but should not be interpreted as a function of the y-axis. To derive meaning relaxometric information, the time frames need to be reconstructed from projections acquired with identical FA and magnetization history. Thus the TR-index must be the same as shown by the red line.

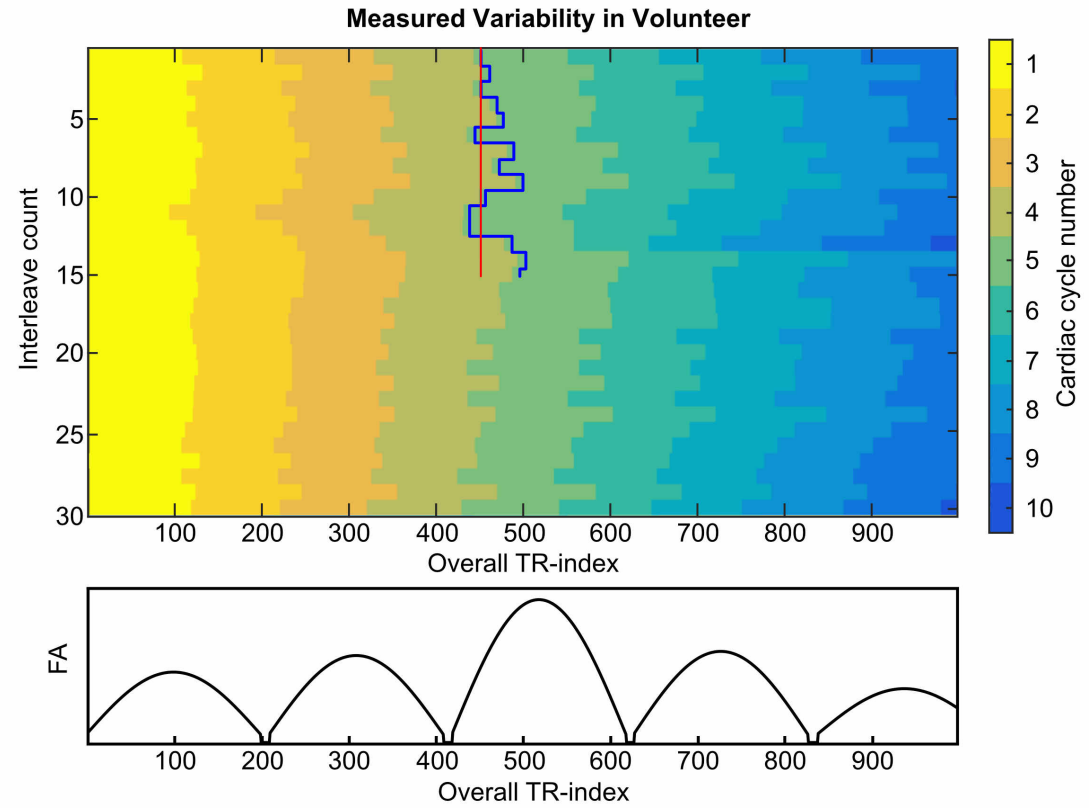

Figure 4.18: The variability of the HR of a healthy volunteer during a Flow-MRF measurement is displayed. Each TR is colored according to the current cardiac cycle number, which is reset at the beginning of each readout train. The blue and red lines shows the indices of the projections which make up the simulated time frames in fig. 4.19. The black FA-pattern in the lower part of the figure serves to give a visual impression of the rate of change in the FA relative to this mixing of projections.

4.3.2 Flip Angle Mixing

Even though the mixing of projections acquired with different FA does not directly influence the velocity quantification, the different weighting of each radial spoke causes a suboptimal interference of undersampling artifacts. Further, the radial projection angle is chosen such that a uniform and optimal k-space coverage is achieved for each time frame. The radial projection angle can be written as:

$$\vartheta_p(i,j) = \frac{\pi}{N_i} i + \varphi \cdot j, \tag{4.11}$$

with ϑ_p the projection angle relative to the k_x axis, i the index of the current shot, j the index of the current TR, N_i the total number of shots and φ the golden angle ($\varphi \approx 2.34$ rad). After the reordering of projections needed for the velocity quantification, this optimal k-space coverage is lost, resulting in higher k-space sampling densities in some regions and lower densities in others.
To evaluate the influence of the FA mixing, numerical simulations were performed based on an ideal heart rate (perfectly steady) and measured heart rate patterns.

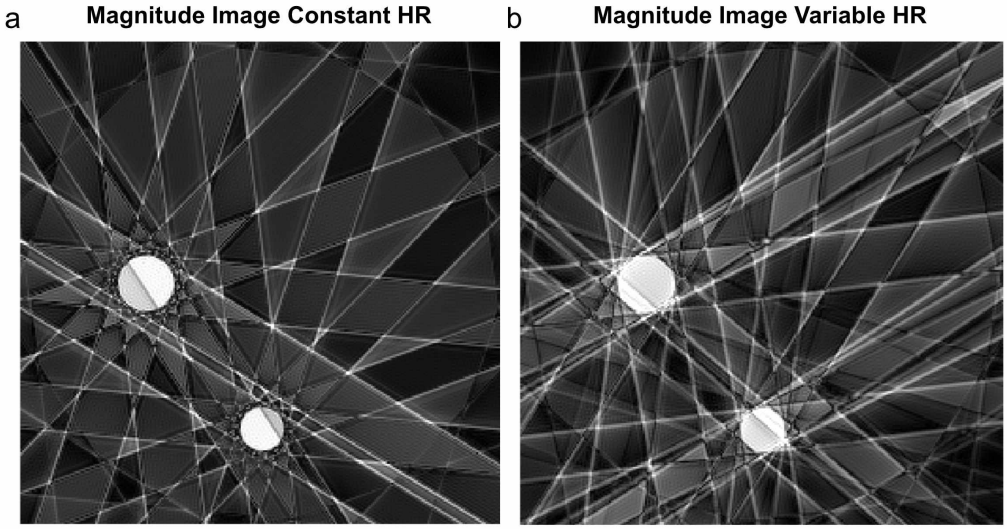

Figure 4.19: Individual time frame used for the velocity quantification based simulated HR patterns. The time frame in (a) is simulated with a perfectly steady HR of 60 beats per minute. The projections constituting this time frame are indicated by the red line in fig. 4.18. The time frame shown in (b) is based on the HR pattern of a volunteer, which is shown in fig. 4.18. The blue line in fig. 4.18 indicates the projection reordered to create the frame in (b).

Figure 4.19 shows, exemplarily, two time frames of the 5$^{\text{th}}$ heartbeat, simulated with a constant HR of 60 beats per minute and the other based on the HR variation shown in fig. 4.18. Additionally, the simulation with variable HR was repeated with three other measured heart rates due to their volunteer dependence as shown in fig. 4.16. The mean and SD of the HR was (1136 ± 93) ms, (1105 ± 63) ms and (985 ± 44) ms. Their respective longest/shortest RR-interval was 1402/784 ms, 1245/985 ms, and 1129/887 ms. The suboptimal k-space coverage can be seen in comparing the two frames in fig. 4.19. The time frame in fig. 4.19b incidentally shows the largest absolute spread of FA between combined projections, one projection was acquired with $\alpha = 58.7\,^\circ$ and another with $\alpha = 5\,^\circ$.

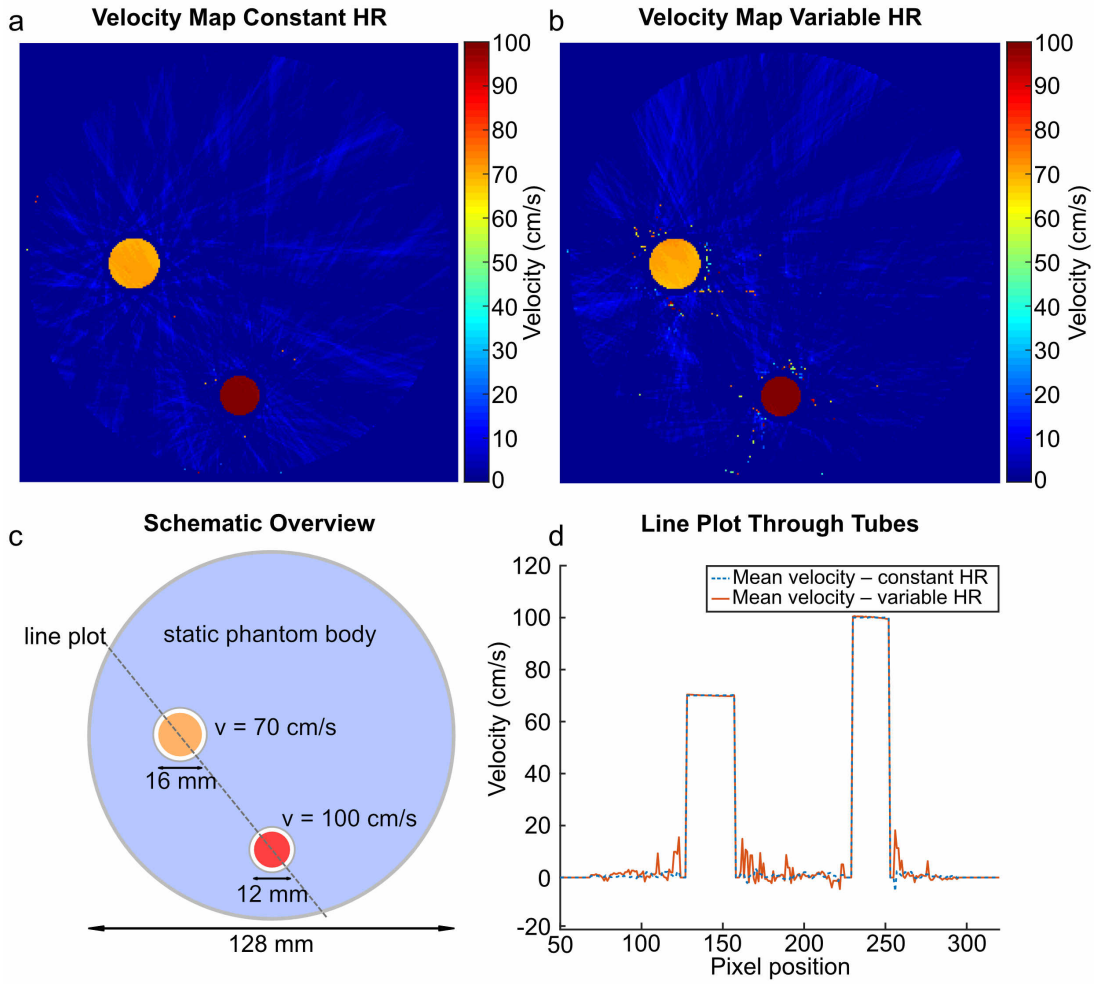

Figure 4.20: The simulation results based on the a variable and constant HR are displayed in this figure. The time frames shown in fig. 4.19 are taken from the data sets which are the basis of the velocity mapping results in this figure. The schematic in (c) of the simulated phantom was already presented in fig. 4.8, here the orientation of the line plot in (d) is indicated. This line plots displayed the mean velocity along the indicated path.

Figure 4.20 presents some of the quantified velocities resulting from the simulated MRF experiments. All simulations were performed without the addition of thermal noise and 15 projections per time frame to emphasize the effect suboptimal projection angles. The mean velocity deviation in all 5 simulations was smaller than 0.1 % from the ground truth (GT) of 100 cm/s and 70 cm/s. The constant HR produced velocities, quantified overall cardiac phase, of (70.0 ± 0.4) cm/s and (100.0 ± 0.5) cm/s with a single pixel peak deviation of 3.3 cm/s. The worst case of the variable HR simulations

produced velocities of (70.0 ± 0.9) cm/s and (100.0 ± 1.0) cm/s with a peak deviation of 5.7 cm/s. These findings, alongside the line plot shown in fig. 4.20d, confirm that the velocity quantification is not biased by variable heart rates, but an increase in velocity noise is observable.

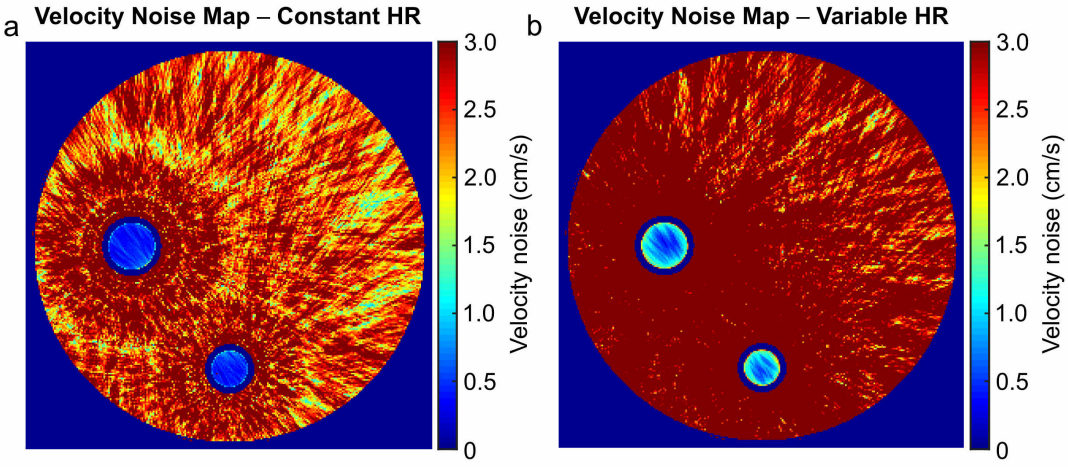

Figure 4.21: These figures illustrate the increase in velocity noise caused by HR variability. The velocity noise is calculated by the standard deviation over all cardiac phases. In the flowing regions the mean increase was 2.1-fold. The velocity noise increase in static regions is inessential as a correct velocity quantification cannot be assured here.

Figure 4.21 displays the pixelwise velocity noise distribution for constant and variable HR. Here an increase in the velocity noise can be noted in both static and flow regions due to the variability of the HR. The velocity noise in the static tissue is inconsequential as velocities cannot reliably be quantified here as shown in section 4.2.3. Within the flowing region, an increase of the velocity SD from 0.48 cm/s to 1.03 cm/s can be determined. This 2.1-fold increase in the velocity noise indicates an upper limit as no thermal noise was added. Nevertheless, the unbiased velocity quantification in the case of a variable heart rate is a positive result as no influence can be had on a volunteer's heart rate.

4.3.3 In-Vivo Studies

In this section, a final validation of the proposed method is shown in a small in-vivo study. Both, velocity, in the popliteal artery, and the relaxation parameters of the gastrocnemius muscle are measured in three healthy volunteers (2 female, 1 male). In figs. 4.22 and 4.23 the maps of only a single volunteer are shown, but the quantified means are stated for all volunteers.

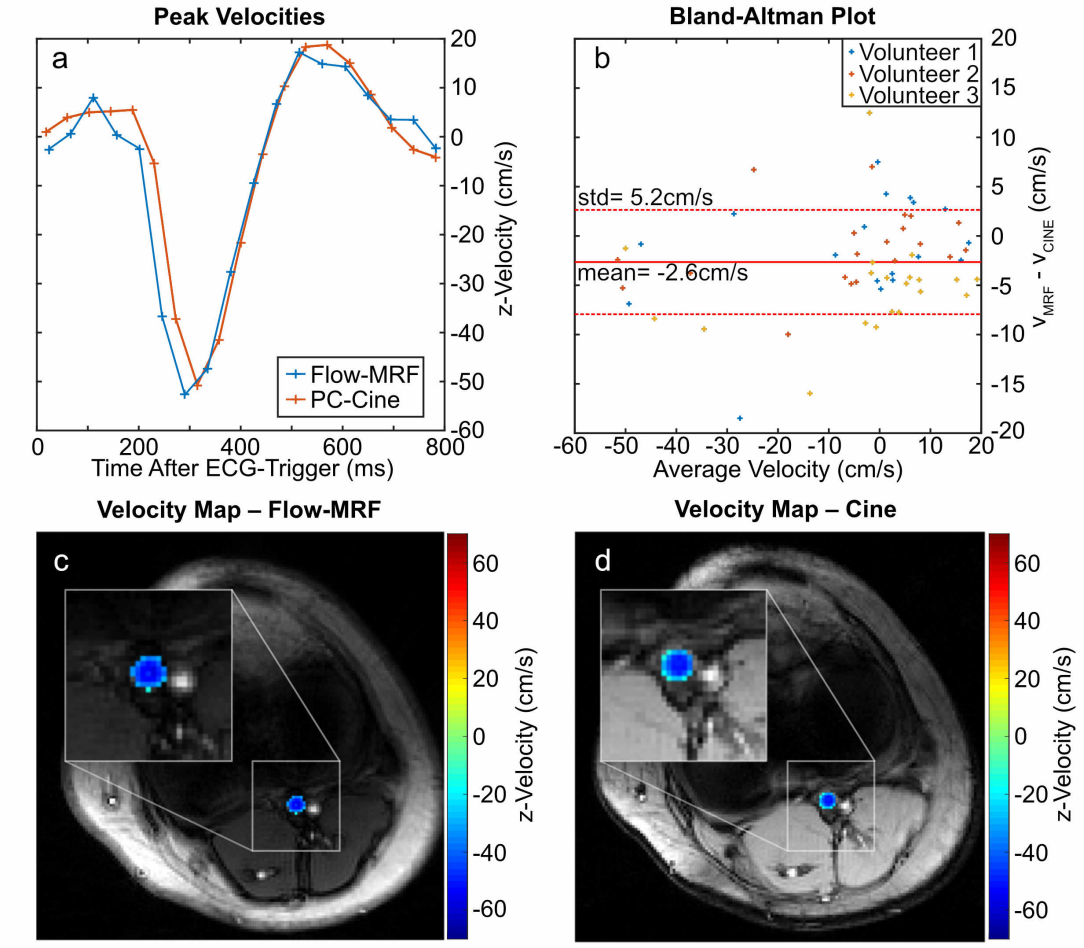

Figure 4.22: Quantitative comparison of velocity quantification results between Flow-MRF and a conventional PC cine in the popliteal artery. The line plot displays the velocity in a central voxel of the vessel. The Bland-Altman plot was generated on the basis of all three volunteer measurements. Velocity maps during peak systole within the vessel are displayed on top of a magnitude overlay in (c-d) for both Flow-MRF and the PC cine.

The temporal evolution of the velocity for a central pixel in the artery is shown in fig. 4.22a and a good agreement between the MRF and PC cine can be observed. The mean deviation between both velocities is $-1.4\,\mathrm{cm/s}$ with a peak deviation of $18.4\,\mathrm{cm/s}$ during steep velocity changes in early systole. The other two scans show mean deviations of -1.2/$-5.1\,\mathrm{cm/s}$ with peak deviations of 7/$12\,\mathrm{cm/s}$. The Bland-Altman plot in fig. 4.22b visualizes the aggregated velocity information of all three measurements. Here, the difference between Flow-MRF and the PC cine is plotted as

a function of their averaged velocity. The velocity maps in the vessel lumen during peak flow are displayed as an overlay in Figure fig. 4.22c-d. The blurring of fatty tissue due to the radial readout is clearly visible in Figure fig. 4.22c for the MRF sequence, as no correction for off-resonances was performed.
The relaxometric maps derived from the MRF data are exemplarily displayed in fig. 4.23. Relaxation constants of (1380 ± 80) ms and (28 ± 4) ms for T_1 and T_2, respectively, were evaluated within the gastrocnemius muscle. The area where a vessel runs through the medial head of the gastrocnemius (left side) was excluded from the quantification. The other two volunteer scans yielded mean relaxation constants of $(1394 \pm 68)/(1377 \pm 78)$ ms for T_1 and $(26 \pm 4)/(24 \pm 5)$ ms for T_2. All relaxation constants are in agreement with the spectroscopically determined values of (1440 ± 150) ms and (25.5 ± 3.1) ms for T_1 and T_2 as reported by Ren et al. (20).

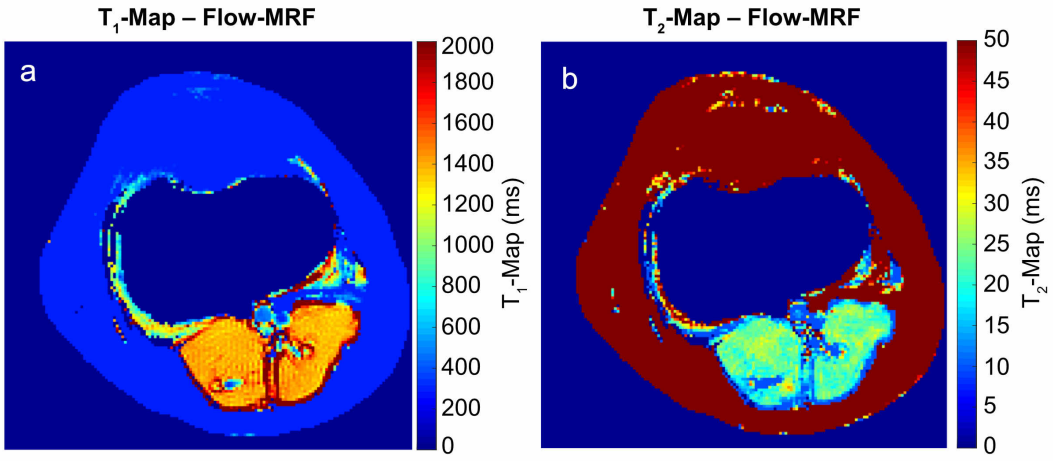

Figure 4.23: Relaxometric maps corresponding to the velocity maps displayed in fig. 4.22. The region of the joint was masked to improve the clarity of the maps.

4.4 Optimization of Velocity Encoding Pattern

Flow-MRF introduces a new degree of freedom in the design of the MRF-pattern in the form of the $\vec{m}_1$ applied before each readout. Similar to the encoding of relaxometric parameters, two main features of the encoding pattern have to be considered. Firstly, how noise in the input data propagates to the determined quantity and secondly the stability of quantification. The former can be described with the Cramér–Rao bound and the Fischer information, which was successfully done for the design of the FA-Pattern [46, 47]. A measure of stability of is more difficult to be formulated. Monte Carlo simulations were used to estimate both the precision and stability [48]. This approach was also utilized to evaluate the different $\vec{m}_1$ patterns.

In Flow-MRF, all three velocity components have to be quantified simultaneously, this can only be achieved if the m_1 pattern of each gradient axis do not correlate highly with each other. A simple method to reduce correlation is to randomly draw m_1 values from a predefined distribution. The design of the $\vec{m}_1$ pattern is thus reduced to the design of random-distributions from which the m_1 values are drawn. The exception to this random-draw design is a pattern based on Multi-Directional High Moment (MDHM) encoding [53]. Here, the encoding in the space of $\vec{m}_1$ are distributed on a sphere with radius $m_{1,max}$ and a golden angle method is used to cover the sphere homogeneously.
In the design of the different m_1 patterns, precision and stability have competing demands on the shape of the random-distributions. Good stability in the quantification is achieved if a broad distribution with many unique m_1 values is used. The highest precision is obtained if the used encoding moments are as high as possible.
These considerations lead to the design of the patterns shown in fig. 4.24. Here, the random distributions are shown as a function free scaling parameter $m_{1,max}$. The difference in m_1 between the two closer peaks, in fig. 4.24e for example, corresponds to the encoding to a v_{enc} of 150 cm/s. These secondary peaks are required to ensure a velocity range of at least $\pm$150 cm/s is resolvable. The first two patterns (fig. 4.24a-b) are designed for high stability and the pattern in fig. 4.24e for maximal precision. The patterns fig. 4.24d,f are trade-offs between stability and precision. Lastly MDHM encoding pattern is included, as this was previously published for use in high moment applications.

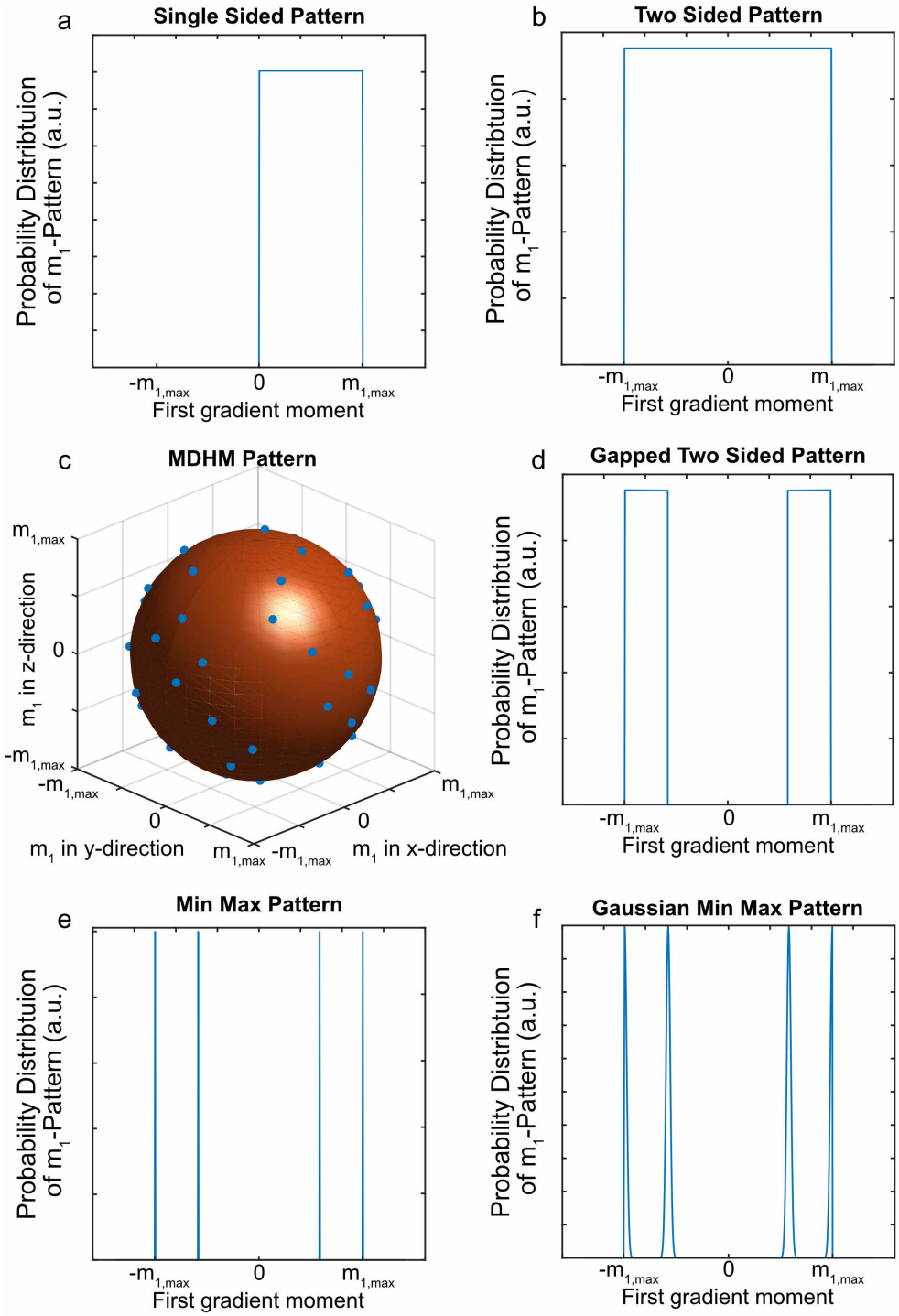

Figure 4.24: Schematic overview of the proposed m_1-pattern evaluated in this simulation study.

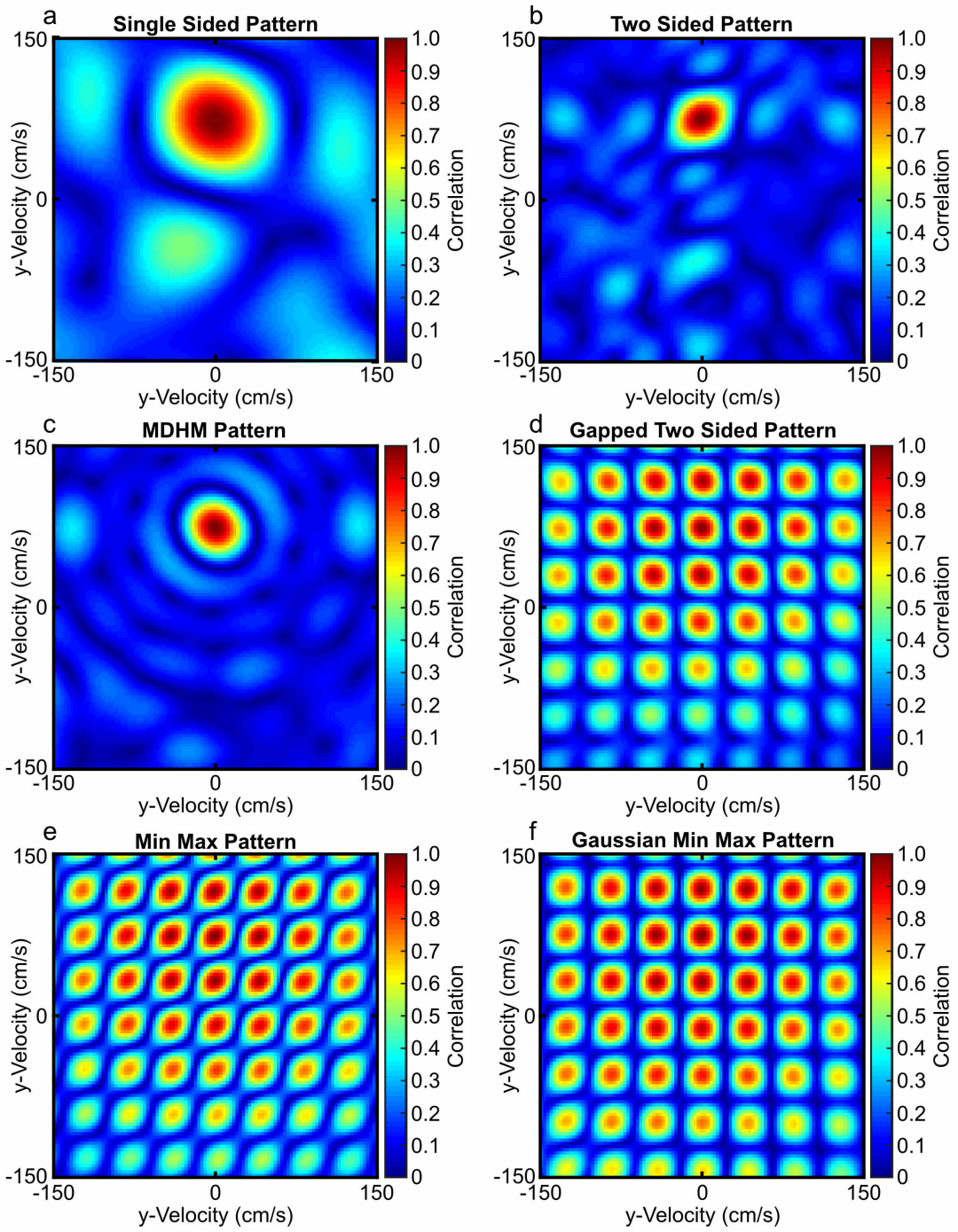

Figure 4.25: Correlation plots for the different m_1 patterns displayed in fig. 4.24. The correlation to a simulated signal vector with velocity $[0\ 75\ 0]$ cm/s was computed. Here $m_{1,max} = 30\,\mathrm{mT/m \cdot ms^2}$.

Figure 4.25 displays the correlation of a simulated signal vector with velocity [0 75 0] cm/s with a 2D-dictionary covering the range of −150 cm/s to 150 cm/s in both x- and y-velocity. Figure 4.25 already shows differences in the design choice between stability and accuracy. The correlation plots in fig. 4.25a,b,c show a single highly correlated maximum around the correct velocity, entailing a good stability of quantification. The global maximum for fig. 4.25d,e,f is narrower than for the other patterns indicating a more precise velocity quantification if the global maximum can be distinguished from the side maxima.
A more quantitative evaluation of the proposed m_1 pattern can be seen in fig. 4.26. Here, the velocity noise in an ROI of the numerical phantom is shown as a function of the maximal encoding moment $m_{1,max}$ for the different patterns. This was tested for *delta peak* velocity distribution and for a Gaussian velocity distribution with 15 cm/s full width half maximum.

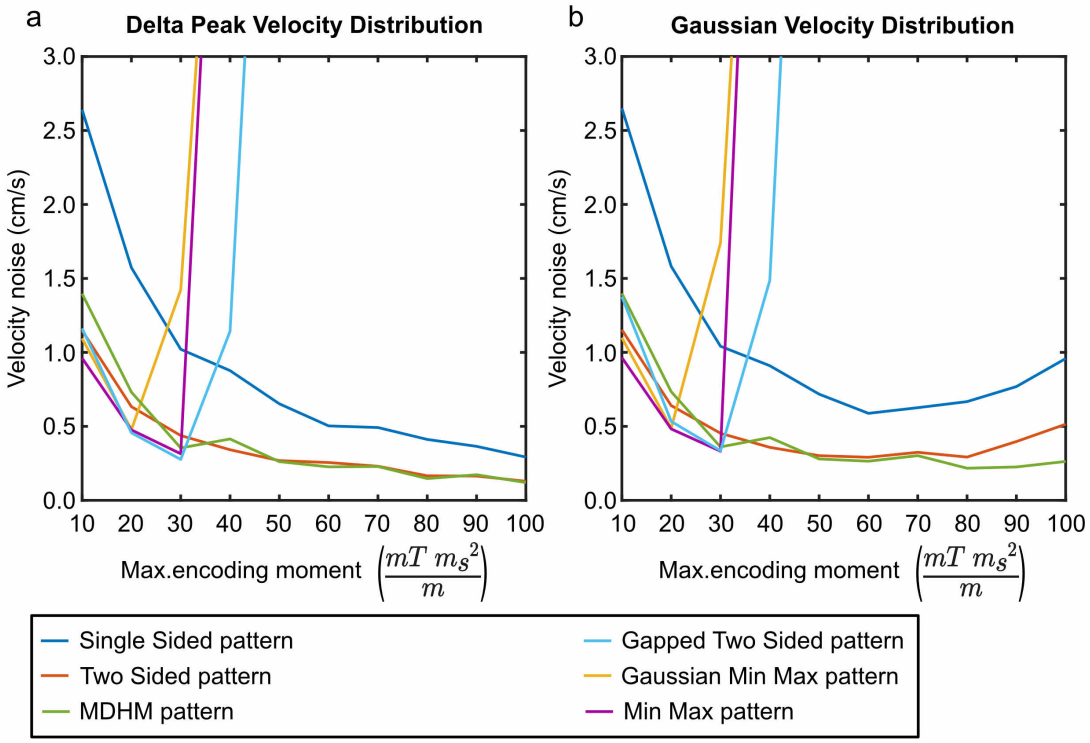

Figure 4.26: Velocity noise in an ROI of the numerical phantom is shown as a function of the maximal encoding moment $m_{1,max}$ for the different patterns. Tested for *delta peak* velocity distribution and for a Gaussian velocity distribution with 15 cm/s full width half maximum.

Considering first the plot in fig. 4.26a: As indicated by the width of the correlation in fig. 4.25a, the *Single Sided pattern* has the highest velocity noise, approximately 2.3-fold higher then the noise for the *Two Sided pattern*.
All three patterns optimized for accuracy display a similar trend. They have the lowest velocity noise for maximal encoding moments below $30\,\mathrm{mT/m \cdot ms^2}$, except for the *Gaussian Min Max pattern* for which the velocity quantification already fails at $30\,\mathrm{mT/m \cdot ms^2}$. The other two patterns fail at encoding moments of $40\,\mathrm{mT/m \cdot ms^2}$, seen by the steep increase in their velocity noise. The *Min Max pattern* for example, has a 20-30 % smaller velocity noise than the *Two Sided pattern* in the range of $10\,\mathrm{mT/m \cdot ms^2} \leq m_{1,max} \leq 40\,\mathrm{mT/m \cdot ms^2}$.
The performance of the *Two Sided pattern* and the *MDHM pattern* is similar, as suggested by the correlation plots in fig. 4.25. Both patterns display a good to moderate performance in the velocity noise while allowing a robust velocity quantification up to $100\,\mathrm{mT/m \cdot ms^2}$, which corresponds to an encoding velocity of 6 cm/s. The expected inverse scaling of the velocity noise with $m_{1,max}$ can be seen for the first three patterns.
The results with a finite width of the simulated velocity distribution revealed a similar noise behavior as for the delta peak distribution. The key difference here is that a constant or increasing velocity noise can be observed once the $m_{1,max}$ exceeds $50\,\mathrm{mT/m \cdot ms^2}$. due to intravoxel signal dephasing.
Given these results, the *Two Sided pattern* or the *MDHM pattern* are preferable to the other investigated patterns. They provide low velocity noise while allowing a stable velocity quantification. Further, increasing the maximal encoding moment beyond $30\,\mathrm{mT/m \cdot ms^2}$ has significantly diminishing returns in the velocity noise, while increasing the TE. This investigation lead the use of the *Two Sided pattern* with a maximal encoding moment of $30\,\mathrm{mT/m \cdot ms^2}$ throughout this work, which was already introduced in section 4.2.1.

4.5 Reynolds Stress Tensor Quantification

Up to this point, the potential for Flow-MRF to simultaneously quantify velocities and relaxation constants has been thoroughly investigated. Inherently, this process quantifies the mean velocity over a voxel and a finite period, which is useful in laminar flow conditions. In a turbulent flow regime, however, the spatiotemporal mean of the velocity is insufficient to describe the flow accurately. The method by which the Reynolds stress tensor can be quantified is described in section 3.2.3. The velocity encoding of Flow-MRF inherently encodes more than the minimum of 6 non-coplanar velocity encodings. The Reynolds-stress information is thus inherently encoded within the Flow-MRF data. Further the large velocity encoding moments achievable in Flow-MRF sample the signal dephasing curve (see fig. 2.13d) more accurately than conventional Reynolds-stress tensor encoding schemes. The possibility to quantify the relaxation constants, the mean velocity, and the Reynolds-stress would increase the relative efficiency of Flow-MRF and might provide higher clinical value.

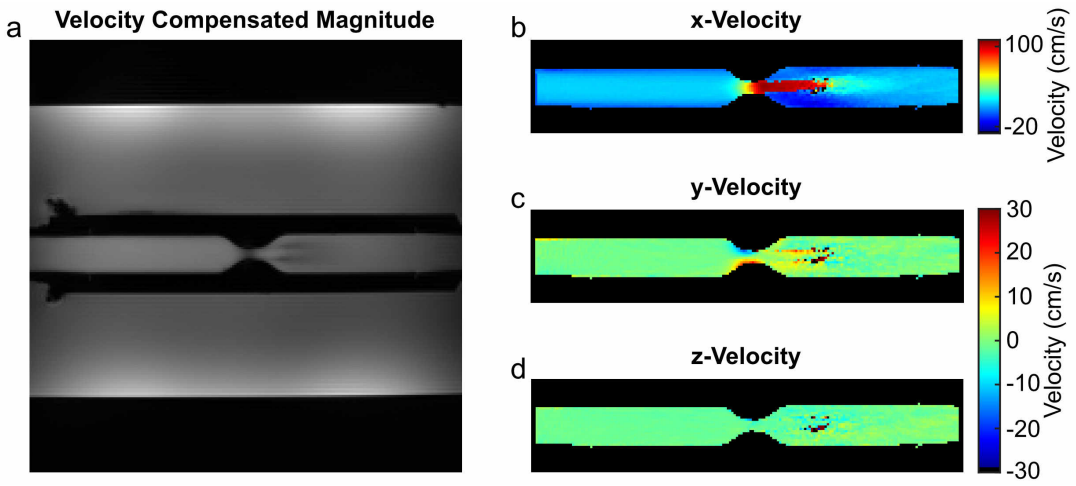

Figure 4.27: A magnitude overview of the stenosis experiment is shown in (a). The corresponding velocity maps determined by Flow-MRF are shown in (b-d). The velocity quantification fails in some pixels at the distal part of the velocity jet in this cardiac phase.

The challenge with the Reynolds stress quantification in Flow-MRF is that the broadening of the velocity distribution solely affects the signal magnitude and the signal magnitude evolution of flowing regions is a priori unknown in Flow-MRF. Sophisticated modeling of flow path while assuming knowledge of the relaxation constants of the fluid and the proton density might allow an estimate of the signal magnitude during the Flow-MRF experiment. Robust modeling, however, has not yet been achieved.

The FA pattern was set to a constant value for all TRs, to demonstrate the potential of Flow-MRF to quantify both velocity and Reynolds stress. This change prohibits the quantification of relaxation constants, but the signal magnitude of flowing regions becomes a pure function of the in-flow, which is periodic with the heartbeat. This periodicity allows the influence of in-flow to be eliminated by quantifying the Reynolds stress tensor in a time-resolved manner.
The reconstruction of the RST for Flow-MRF with constant FA is similar to the conventional reconstruction presented in section 3.2.3. The following linear system of equations is solved numerically:

$$\begin{pmatrix} k_{x,1}^2 & k_{y,1}^2 & k_{z,1}^2 & k_{x,1}k_{y,1} & k_{x,1}k_{z,1} & k_{y,1}k_{z,1} \\ k_{x,2}^2 & k_{y,2}^2 & k_{z,2}^2 & k_{x,2}k_{y,2} & k_{x,2}k_{z,2} & k_{y,2}k_{z,2} \\ \vdots & \vdots & \vdots & \vdots & \vdots & \vdots \\ k_{x,N}^2 & k_{y,N}^2 & k_{z,N}^2 & k_{x,N}k_{y,N} & k_{x,N}k_{z,N} & k_{y,N}k_{z,N} \end{pmatrix} \begin{pmatrix} \tau_{xx} \\ \tau_{yy} \\ \tau_{zz} \\ \tau_{xy} \\ \tau_{xz} \\ \tau_{yz} \end{pmatrix} = \begin{pmatrix} -2\ln(|S(\vec{k}_1)|) + 2\ln(|S_0|) \\ -2\ln(|S(\vec{k}_2)|) + 2\ln(|S_0|) \\ \vdots \\ -2\ln(|S(\vec{k}_N)|) + 2\ln(|S_0|) \end{pmatrix}. \tag{4.12}$$

Here, $k_{x,N}$ represent the N velocity encodings for a given direction, with N being the number of time frames used for the quantification. $S(\vec{k}_N)$ is the signal in a voxel during the N^{th} time frame and S_0 is the signal for a velocity compensated measurement, meaning no dephasing due to velocity. The only difference between eq. (4.12) and eq. (3.15), which describes the conventional RST problem, is that S_0 is unknow in the reconstruction and is estimated alongside τ. This set of equations is also solved by a Moore-Penrose pseudoinverse.

Figure 4.27 shows the velocity maps and a magnitude overview of the Flow-MRF experiment. The velocity maps show the expected 9-fold velocity increase from the mean x-velocity of 11.9 cm/s upstream of the stenosis to 103.9 cm/s. This increase is caused by the reduction of the diameter of the tube from 15 mm to 5 mm in the stenosis. In all three velocity components, some pixels display erroneous velocities at the end of the jet, potentially caused by a high signal dephasing. The magnitude image in fig. 4.27a shows changes in signal intensity in the stenosis and beyond, despite being velocity compensated ($\vec{m}_1 = 0$). Here, influences of higher moments cannot be excluded due to the rapid change in velocity and the large encoding gradients used.

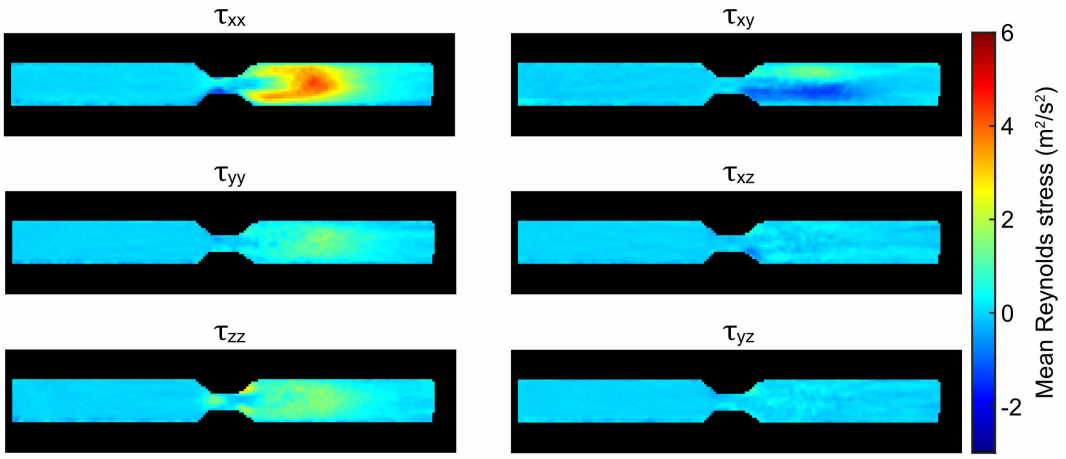

Figure 4.28: The individual components of the Reynolds stress tensor are displayed. These were quantified by the proposed Flow-MRF method.

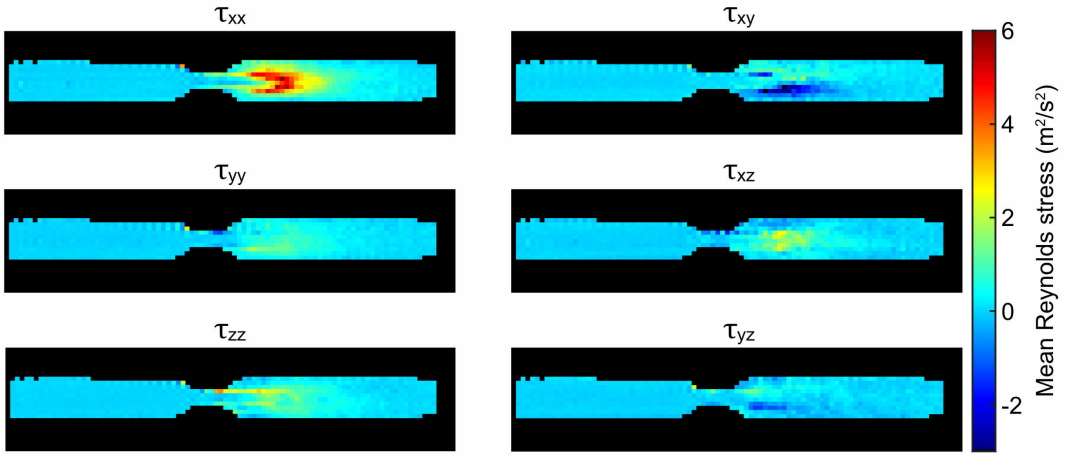

Figure 4.29: This figure displays the reference values of all Reynolds stress tensor components acquired by a conventional 3D PC-cine with 7 velocity encoding as described in section 3.2.3.

All Reynolds stress components maps quantified with Flow-MRF in the stenosis phantom are shown in fig. 4.28. Here the temporal average is shown to increase the SNR and to allow a better comparison with the reference measurement. Further, the temporal information of all 4 neighboring pixels are combined for the quantification also to reduce the noise level but at the cost of spatial resolution. The difficulty to quantify the Reynolds stress components is shown in fig. 4.29 where the results of a

conventional experiment are shown. A good agreement in both shape and amplitude between Flow-MRF and the reference can be observed, even though the peak stress is quantified to be 14 % lower for Flow-MRF.

5 Discussion

This work demonstrated the potential of MRF to quantify relaxation constants and time-resolved velocities at ultra-high fields simultaneously. The quantification of the three-dimensional velocity vector with MRF in humans hinges on the decoupling between relaxometry and velocimetry. This decoupling allows a temporal reordering of acquired projections for the velocity quantification, which is required due to the inter-beat variability of the heart-rate. Lastly, the capability to quantify all components of the Reynolds stress tensor with Flow-MRF was investigated.

The influence of a variable TR in a FISP-MRF sequences on the signal phase was studied in the beginning of this work. It was shown that the non-FID signal paths create a variable signal phase throughout the MRF-pattern, despite the use of a constant TE and gradient spoiling. This observation seems to contradict the claim made by the authors of the FISP-MRF paper [8], as they clearly state independence of FISP-MRF on local changes in resonance frequency. The independence of FISP-MRF with respect to off-resonance is not because of a constant influence on the signal but rather because every atom in the dictionary displays a temporally constant phase. The identical signal phase behavior of every atom means that the measured variable signal phase only reduces the overall correlation, but the atom with the highest correlation is unchanged. This creates seeming robustness against ΔB_0 variations as only the highest correlating atom determines the relaxation times.

The phase modulation due to the variable TR, generally appear to be below 1 rad and thus the influence on the mapping of relaxation constants is negligible, unless large distributions of off-resonances are present within a single voxel. This, theoretically, is a disadvantage of the variable TR, but a large spread of ΔB_0, in the order of 10-100 Hz, is needed to create a severe effect. The effect might only be noticeable at ultra high field and in tissues with a large difference between T_2 and T_2^*, such as in the liver. The iron content of the liver is known to result in short T_2^* constants [54]. Setting the TR to a constant value results in a constant phase throughout the MRF sequence, without reducing the encoding capability of the MRF-pattern. No claim is made that in a general case a variable TR is not beneficial to the encoding capability of MRF. For fully balanced MRF sequences, for example, the variability of the TR is certainly of central importance [55]. The MRF pattern used in this work does not benefit from this variability, and the non-constant phase would hinder a phase based velocity

quantification. These observations motivate the use of a constant TR in the Flow-MRF sequence.

The velocity sensitivity of Flow-MRF was achieved by adding bipolar gradients on all three gradient axes between the excitation and the readout, modulating the first gradient moment from one TR to the next. This additionally imparted phase, proportional to velocity, allows the reconstruction of the three-dimensional velocity vector. The gradients are updated in real time based on the feedback of an ECG. This allows synchronous velocity encoding with the cardiac cycle, needed to cope with the variability of the HR. Periodic flow is assumed in the reconstruction to reduce the temporal velocity resolution from approximately 500 ms to 45 ms. This reduction is achieved by combining data from multiple cardiac cycles into the reconstruction of a single cardiac phase. Here, as in conventional PC MRI, the periodicity of the velocities with the ECG-signal is assumed. Even though changes in the RR-interval of a volunteer between 716 ms and 1281 ms were observed during a measurement, identical velocities are assumed during the first 700 ms of each heartbeat. The flow velocities in a vessel can change as a function of the heart rate, but the observed variability in the RR-interval is not caused by an increase of the mean HR, such as under exercise, but due to stochastic variations. Significant artifacts would be observed in conventional PC cine and Flow-MRF sequences if the assumption of periodic flow is violated.

A defining features of Flow-MRF is the use of high velocity encoding moments while maintaining a large range of correctly quantifiable velocities. The spread of velocity encoding moments for all phantom and in-vivo experiments was $60\,\mathrm{mT/m \cdot ms^2}$. This exceeds the encoding moments of the reference measurement more then five-fold. The velocity noise is inversely proportional to the spread of encoding moments. Simulations determined the range of reliably quantifiable velocities to be between 3 cm/s and 840 cm/s. The upper limit exceeds even the peak velocities found in patients with severe aortic stenosis [12], which present some of the highest flow velocities in the human body. The maximum velocity observed in a healthy person is around 150 cm/s. Flow in severe aortic stenosis is highly turbulent, reducing the signal in flowing regions as a function of the velocity encoding moment. Thus, the turbulence might require the use of smaller encoding moments.
Both of the above-mentioned features of Flow-MRF are possible because a reconstruction was developed, which allows any number of phase warps in the measured data. A dictionary based reconstruction was chosen, but a dictionary covering the range of velocities in healthy humans with a velocity resolution of 0.1 cm/s would require 20 terabytes of computational memory. The reconstruction of velocities is thus performed in two separate steps, firstly an exhaustive search is evaluated on a coarse dictionary with a velocity resolution of 5 cm/s. Then secondly, a local gradient ascent

optimization of the correlation between the synthetic signal evolution and the measured signal is performed. The starting points of the optimization were determined by the previous reconstruction step. The highest correlating synthetic signal evolution determines the best estimate of the velocity for each pixel. This reconstruction is slow, taking in the order of 2-10 min per cardiac phase but determines the global maximum in the search-range reliably. The reconstruction time could be reduced by efficient parallel computing, *through dictionary fitting* [32], or deep learning.

The phantom experiments determined a good agreement between Flow-MRF and a vendor provided PC cine sequence. The average deviation throughout a pulsed velocity profile was determined as (-1.7 ± 2.3) cm/s for an experiment with flow in z-direction. Double oblique slice positioning allowed the measurement of finite velocities in all three spatial components, here a mean deviation was quantified as (0.17 ± 1.16) cm/s. The measurement time in both experiments was 84 s for Flow-MRF. This, however, includes 40 s of pauses between shots, to allow the magnetization to approximate the thermal equilibrium. These pauses can be shortened [56] or be used to acquire different slices. The effective measurement time per slice is thus 44 s. Therefore, Flow-MRF has fourfold shorter acquisition time than the vendor provided clinical standard for velocity quantification with closely matched spatiotemporal resolutions, while additionally providing quantitative T_1 and T_2 maps. The measurement time reduction of PC cine sequences has been extensively investigated [57, 58, 59, 60]. These methods often allow acquisition time reductions greater then the factor of 4 between Flow-MRF and the PC-cine but often result in spatial or temporal blurring of velocities. In Flow-MRF the reconstruction between temporal bins is completely independent. In theory, Flow-MRF could also be accelerated by compressed sensing techniques or temporal data sharing.
The in-vivo measurements showed good agreement in the velocity quantification, but a peak deviation of 18.4 cm/s was measured during the systole of the first volunteer. This is potentially caused by the inherently different velocity encoding schemes between Flow-MRF and the reference. Flow-MRF determines the temporal mean of all three velocity components throughout the cardiac phase (45 ms). The reference, on the other hand, measures a velocity component at a single time point and then proceeds to measure the two other velocity components. As a result, the same velocity component is also measured with a temporal resolution of 45 ms, but the measured velocity corresponds to a discrete point in time within these 45 ms. This difference in the velocity encoding can lead to different results in rapidly changing flow conditions, such as the systole.

Post-processing of conventional phase-based cine sequences includes a linear or quadratic correction of background velocities to remove effects of eddy currents and concomitant fields [11]. In Flow-MRF, however, the background velocities cannot be

approximated as linear as can be seen in fig. 4.9, due to the non-Cartesian readouts. The effect of concomitant fields is assumed to be small due to the central position of the investigated targets and the high main magnetic field. Eddy currents might have a measurable influence on the quantified velocities, especially since larger bipolar encoding gradients are used than in conventional PC sequences. In theory, given a model of eddy current behavior, their influence can be included in the reconstruction eliminating the eddy current induced velocity-bias. Such an eddy current model could be constructed based on the measurement of cross terms and higher orders of the gradient impulse response function [61].

The challenge of variable RR-intervals in humans was tackled by eliminating the influence of the MRF pattern on the signal phase. This change allows the reordering of projections combined into a single time frame used for the velocity quantification. Only the velocity encoding gradients are updated based on the ECG signal, the FA remains unchanged. The choice not to update the FA pattern was made to avoid the calculation of a relaxometric dictionary for each volunteer. The calculation of such a dictionary for 7 T takes approximately 118 hours or almost 5 days. Further, the encoding capability for T_1 and T_2 would depend on the specific HR of the volunteer, making the mapping potentially unreliable. The reordering for the velocity combination requires projections acquired with different FA to be combined into a single time frame, as a consequence of not updating the FA-pattern. This reordering causes a suboptimal interference of undersampling artifacts and a subsequent increase in the velocity noise. The presented simulation, investigating this effect, used 15 projections instead of 5 to emphasize the increase in undersampling noise. For the same reason, thermal noise was omitted. The two-fold velocity noise increase due to the variability of the HR, indicates an upper limit for healthy subjects. The influence for patients with cardiac arrhythmias remains to be investigated.

The phase information of time frames separated up to 9 s within the MRF readout train are combined for the velocity quantification. Phase drifts during measurements are not uncommon in MRI [62]. These drifts, even though rare in modern MRI systems, can be induced by an unstable RF-phase, gradient coil heating or other effects. Whether Flow-MRF is susceptible to phase drifts was investigated by simulating the effect of an additional linear phase contribution. The additional phase was assumed zero after the 8 s pause for relaxation, followed by a linear increase to a maximum phase of θ_{max}. This parasitic phase only caused a systematic velocity error of $-0.34\,\mathrm{cm/s/rad}$. However, if the phase increase exceeded 4 rad then a complete failure of the velocity quantification was observed. A phase increase of this magnitude would create significant artifacts in almost all MRI sequences. The small influence of the phase drift on the velocity quantification can be explained by reconsidering the velocity reconstruction for

Flow-MRF. The reconstruction is effectively searching for the highest correlation in a predefined set of phase evolution, termed a dictionary. None of the dictionary atoms present a phase evolution similar to the additional parasitic phase. The parasitic phase contributions and the phase created by flow are highly uncorrelated, thus only a small shift in the quantified velocities is observed.

Besides the velocimetry, the quantification of correct relaxation constants with Flow-MRF is of central importance. The aim was to maintain the quality of the relaxometric mapping relative to the original FISP-MRF pattern. As a consequence, a simulation study investigating the influence of the constant TR on the encoding capability of MRF was performed. Further, the effects of the bipolar velocity encoding gradients on the relaxation time quantification were measured in a phantom study and lastly, the relaxation constants determined with Flow-MRF were correlated to reference measurements in a phantom.
Eliminating the variability of the TR throughout the acquisition train resulted in a signal level reduction of 5 % or less. The constancy of the signal level allowed a relative comparison of the encoding capability via the mean of autocorrelation matrices. These displayed minor improvements in the encoding capability of 0.961 to 0.954 for T_1 and 0.986 to 0.985 for T_2. Overall an identical performance in the mapping of T_1 and T_2 is expected, whether the TR is constant or variable. The constant TR results in a shorter measurement time, a constant signal phase over the whole MRF pattern and robustness against intravoxel dephasing. The constant TR is therefore used in Flow-MRF.
The use of bipolar gradients resulted in small changes in the quantified relaxation constants in the relaxometric phantom. Here, a mean bias of 0.4 ms for T_1 and -2.2 ms for T_2 was determined. These deviations are below the in-vivo noise levels of 75 ms and 4 ms for T_1 and T_2 respectively. Nevertheless, a finite underestimation of T_2 by the MRF sequence with bipolar gradients can be observed. This is potentially caused by an increased diffusion influence due to the added gradient lobes. In general, diffusion might bias the quantification of relaxation constants in MRF. The simultaneous quantification of diffusion, as demonstrated by Jiang et al. [9], could eliminate the diffusion bias in MRF.
A strong influence of diffusion, however, is unlikely as the T_2 values determined by Flow-MRF correlate highly with the spin echo based values. The mean difference between both methods is (0.8 ± 2.5) ms. The reference measurement can also be biased by diffusion, as was previously shown [63]. Multi-spin echo sequences, designed to reduce the effect of diffusion, perform poorly at 7 T due to the B_1-field inhomogeneity. For T_1, the mean deviations between Flow-MRF and the reference are larger than for T_2. This deviation is quantified as (-89 ± 25) ms, with a peak underestimation by Flow-MRF of -133 ms. These deviations can potentially be explained by the modeling of the adiabatic inversion pulse. The inversion preparation has a strong influence on

the quantified T_1. This pulse was modeled as a 175 ° pulse for all isochromates, as more realistic modeling requires knowledge of B_1 and ΔB_0. ΔB_0 was not mapped during the measurement, causing the simple modeling of the adiabatic inversion. Likely, a more accurate simulation of this pulse would improve the mapping accuracy of T_1. Despite the simplistic modeling of the inversion pulse, a good agreement with the literature values of the relaxation constants in muscle at 7 T was reached. The literature values were determined by single voxel spectroscopy, making them potentially more susceptible to partial volume effects with vessels or other tissues.

The new degree of freedom in the design of the MRF pattern was explored in a simulation study where the performance of multiple m_1 patterns was investigated. Both a study of the correlation matrix and the velocity noise in the numerical phantom were used to evaluate the accuracy and stability of the velocity quantification.
The investigation concluded that the *Two Sided pattern* or the *MDHM pattern* with maximum encoding moments of $30\,\mathrm{mT/m \cdot ms^2}$ provide good stability in the quantification and a low velocity noise. The *MDHM pattern* requires the encoding moments to be spread equally over a spherical surface, while the *Two Sided pattern* can be realized by random draw. The latter was thus preferred for its ease of implementation on the MR system. Nevertheless, the simulation also indicated that a 30 % reduction in the velocity noise could be possible by choosing the *Min Max pattern* with a maximum encoding moment of $30\,\mathrm{mT/m \cdot ms^2}$. This reduction in velocity noise is substantial and might solicit further investigation for specific applications. For the applications shown, however, the stability of the *Two Sided pattern* was favored. Potentially, a pattern can be found, which better trades off the advantages and disadvantages between the stable and accurate patterns design.

Measuring the signal loss due to intravoxel dephasing for different velocity encoding directions can allow the estimations of the Reynolds stress tensor, which describes the stochastic distribution of velocities. In this work, the velocity distribution was assumed Gaussian. This assumption allows the quantification of the RST to be formulated as a linear problem, solvable through a Moore-Penrose pseudoinverse.
Through the use of high encoding moments, Flow-MRF is uniquely suited for the simultaneous quantification of both velocity and the RST. The large number of observation points of the signal dephasing can, in theory, allow a more accurate estimate of the Fourier-transform of the velocity distribution. On the other hand, the effective SNR in each time frame is low for Flow-MRF compared to conventional methods. The large number of data points could allow an estimate of higher central moments of the velocity distribution, such as the skewness or kurtosis. Although, the determination of only the second central moment under the assumption of a multivariate normal distribution is already a difficult problem. The dephasing solely affects the image magnitude, which is less robust than the signal phase with high spatial undersampling.

Nevertheless, the quantified shape and magnitude of the RST component maps match those determined by the reference method of Haraldsson et. al [37]. The characteristic changes in both τ_{xz} and τ_{yz} seen in the reference method, are not seen in the maps of Flow-MRF. This effect might be linked to the coarser z-resolution of the Flow-MRF experiment. Especially for RST mapping, isotropic voxel size is important for the quantification. The use of high encoding moments in the RST quantification needs to be evaluated thoroughly in many flow conditions. Dyverfeldt et al. could show that large encoding moments can create a stronger bias in the determination of the second central moments if higher moments are present but neglected in the reconstruction [41].
The dependence of the RST quantification on the signal magnitude complicates the use of variable FA in Flow-MRF because the formulation of a general model for the magnitude signal evolution has not yet been achieved. In principle, the signal evolution could be calculated if both the relaxation constants and the path of the fluid through the slice were known. The relaxation constants for blood could be measured ex-vivo and potentially a linear approximation of the path could be deduced from the velocity information. If these assumptions suffice to describe the signal evolution has not been tested yet. The lack of a complete signal model enforced the use of a constant FA, such that changes in the magnitude can be linked to inflow or changes in the turbulence. The constant FAs prohibited the quantification of T_1 and T_2, but the simultaneous quantification of the RST and velocities was successfully demonstrated.

Summary

Flow-MRF is the first method allowing the simultaneous time-resolved velocity quantification, while also mapping relaxation times in static tissues. This was achieved by formulating the combined problem in the MR Fingerprinting framework. Both mapping problems were designed, through the choice of the MRF pattern, such that the encoding of either set of parameters creates minimal coupling between them. To this end, the phase modulations for finite off-resonances were eliminated through the use of a constant TR. Further, the phase based velocity encoding is realized by modulating m_1 pseudo-randomly from TR to TR, which does not influence the signal evolution of static tissue.
It was shown in simulations, phantom and in-vivo experiments that the proposed encoding strategy of Flow-MRF allows highly accurate and robust quantification of relaxation constants and velocities in a measurement time 4-fold shorter than conventional MRI based velocimetry. Velocity quantification is part of routine clinical MRI examinations for certain diseases, despite the usually long acquisition times. Flow-MRF could provide a novel approach to shorten the acquisition times, while maintaining high quality in the velocity quantification, and additionally determining relaxometric information of the surrounding static tissue. This joint information could be especially helpful in the assessment of arteriosclerosis.

Bibliography

[1] OECD, *Health at a Glance 2017.* 2017.

[2] J. Thompson, P. Van Leeuwen, D. Moses, R. Shnier, P. Brenner, W. Delprado, M. Pulbrook, M. Böhm, A. Haynes, A. Hayen, and P. Stricker, "The Diagnostic Performance of Multiparametric Magnetic Resonance Imaging to Detect Significant Prostate Cancer," *Journal of Urology*, vol. 195, no. 5, pp. 1428–1435, 2016.

[3] F. Visser, J. J. M. Zwanenburg, J. M. Hoogduin, and P. R. Luijten, "High-resolution magnetization-prepared 3D-FLAIR imaging at 7.0 Tesla," *Magnetic Resonance in Medicine*, vol. 64, no. 1, pp. 194–202, 2010.

[4] P.-F. Van de Moortele, C. Akgun, G. Adriany, S. Moeller, J. Ritter, C. M. Collins, M. B. Smith, J. T. Vaughan, and K. Uğurbil, "B1 destructive interferences and spatial phase patterns at 7 T with a head transceiver array coil," *Magnetic Resonance in Medicine*, vol. 54, no. 6, 2005.

[5] S. C. Deoni, "High-resolution T1 mapping of the brain at 3T with driven equilibrium single pulse observation of T1 with high-speed incorporation of RF field inhomogeneities (DESPOT1-HIFI)," *Journal of Magnetic Resonance Imaging*, vol. 26, no. 4, pp. 1106–1111, 2007.

[6] M. A. Cloos, F. Knoll, T. Hoogduin, Zhao, K. T. Block, M. Bruno, G. C. Wiggins, and D. K. Sodickson, "Multiparametric imaging with heterogeneous radiofrequency fields," *Nature Communications*, vol. 7, 2016.

[7] D. Ma, V. Gulani, N. Seiberlich, K. Liu, J. L. Sunshine, Duerk, J. L., and M. A. Griswold, "Magnetic resonance fingerprinting," *Nature*, vol. 495, no. 187, 2013.

[8] Y. Jiang, D. Ma, N. Seiberlich, V. Gulani, and M. A. Griswold, "MR fingerprinting using fast imaging with steady state precession (FISP) with spiral readout," *Magnetic Resonance in Medicine*, vol. 74, no. 6, 2015.

[9] Y. Jiang, D. Ma, K. Wright, N. Seiberlich, V. Gulani, and M. A. Griswold, "Simultaneous T1, T2, Diffusion and Proton Density Quantification with MR Fingerprinting," *In Proc. 22nd Annual Meeting of ISMRM*, 2014.

[10] S. C. Deoni, B. K. Rutt, and T. M. Peters, "Rapid combined T1 and T2 mapping using gradient recalled acquisition in the steady state," *Magnetic Resonance in Medicine*, vol. 49, 2003.

[11] P. Dyverfeldt, M. Bissell, A. J. Barker, A. F. Bolger, C.-J. Carlhäll, T. Ebbers, C. J. Francios, A. Frydrychowicz, J. Geiger, D. Giese, M. D. Hope, P. J. Kilner, S. Kozerke, S. Myerson, S. Neubauer, O. Wieben, and M. Markl, "4D flow cardiovascular magnetic resonance consensus statement," *Journal of Cardiovascular Magnetic Resonance*, vol. 17, no. 1, 2015.

[12] P. van Ooij, W. V. Potters, A. J. Nederveen, B. D. Allen, J. Collins, J. Carr, S. C. Malaisrie, M. Markl, and A. J. Barker, "A methodology to detect abnormal relative wall shear stress on the full surface of the thoracic aorta using four-dimensional flow MRI," *Magnetic Resonance in Medicine*, vol. 73, no. 3, 2015.

[13] National Heart, Lung, and Blood Institute, "Atherosclerosis." `https://www.nhlbi.nih.gov/health-topics/atherosclerosis#Signs,-Symptoms,-and-Complications`. Accessed: 2019-02-24.

[14] H. R. Underhill, T. S. Hatsukami, Z. A. Fayad, V. Fuster, and C. Yuan, "MRI of carotid atherosclerosis: clinical implications and future directions," *Nature Reviews Cardiology*, vol. 7, no. 165, 2010.

[15] R. L. Vanninen, H. I. Manninen, P. L. Partanen, P. A. Vainio, and S. Soimakallio, "Carotid artery stenosis: clinical efficacy of MR phase-contrast flow quantification as an adjunct to MR angiography.," *Radiology*, vol. 194, no. 2, 1995.

[16] M. Cibis, W. V. Potters, M. Selwaness, F. J. Gijsen, O. H. Franco, M. Arias Lorza, Andres M.and de Bruijne, A. A. van der Lugt, A. J. Nederveen, and J. J. Wentzel, "Relation between wall shear stress and carotid artery wall thickening MRI versus CFD," *Journal of Biomechanics*, vol. 49, no. 5, 2016.

[17] W. Gerlach and O. Stern, "Der experimentelle Nachweis der Richtungsquantelung im Magnetfeld," *Zeitschrift für Physik*, 1922.

[18] F. Bloch, "Nuclear Induction," *Phys. Rev.*, vol. 70, 1946.

[19] N. Bloembergen, E. M. Purcell, and R. V. Pound, "Relaxation Effects in Nuclear Magnetic Resonance Absorption," *Phys. Rev.*, vol. 73, 1948.

[20] J. A. Fessler, "On NUFFT-based gridding for non-Cartesian MRI," *Journal of Magnetic Resonance*, vol. 188, 2007.

[21] J. Pauly, D. Nishimura, and A. Macovski, "A k-space analysis of small-tip-angle excitation," *Journal of Magnetic Resonance (1969), volume = [81*, no. 1, 1989.

[22] O. P. Simonetti, R. E. Wendt III, and J. L. Duerk, "Significance of the point of expansion in interpretation of gradient moments and motion sensitivity," *Journal of Magnetic Resonance Imaging*, vol. 1, no. 5, 1991.

[23] S. Schmidt, S. Flassbeck, M. E. Ladd, and S. Schmitter, "On the Point of Gradient Moment Expansion for Multi-Spoke RF Pulses," *In Proc. Joint Annual Meeting of ISMRM-ESMRMB*, 2018.

[24] M. Weigel, "Extended phase graphs: Dephasing, RF pulses, and echoes - pure and simple," *Journal of Magnetic Resonance Imaging*, vol. 41, no. 2, 2015.

[25] R. Kaiser, E. Bartholdi, and R. R. Ernst, "Diffusion and field-gradient effects in NMR Fourier spectroscopy," *The Journal of Chemical Physics*, vol. 60, no. 8, 1974.

[26] Y. Zur, M. L. Wood, and L. J. Neuringer, "Spoiling of transverse magnetization in steady-state sequences," *Magnetic Resonance in Medicine*, vol. 21, 1991.

[27] B. Rieger, F. Zimmer, J. Zapp, S. Weingärtner, and L. R. Schad, "Magnetic resonance fingerprinting using echo-planar imaging: Joint quantification of t1 and relaxation times," *Magnetic Resonance in Medicine*, vol. 78, 2017.

[28] S. Aja-Fernández and G. Vegas Sánchez-Ferrero, *Statistical Analysis of Noise in MRI.* Springer, 2016.

[29] R. Lattanzi, B. Zhang, F. Knoll, J. Assländer, and M. A. Cloos, "Phase unwinding for dictionary compression with multiple channel transmission in magnetic resonance fingerprinting," *Magnetic Resonance Imaging*, vol. 49, 2018.

[30] O. Cohen, B. Zhu, and M. S. Rosen, "MR fingerprinting Deep RecOnstruction NEtwork (DRONE)," *Magnetic Resonance in Medicine*, vol. 80, no. 3, 2018.

[31] N. Pannetier and N. Schuff, "Kd-tree for Dictionary Matching in Magnetic Resonance Fingerprinting," *In Proc. 23th Annual Meeting of ISMRM*, 2015.

[32] M. Yang, D. Ma, Y. Jiang, J. Hamilton, N. Seiberlich, M. A. Griswold, and D. McGivney, "Low rank approximation methods for MR fingerprinting with large scale dictionaries," *Magnetic Resonance in Medicine*, vol. 79, no. 4, 2018.

[33] M. Yang, Y. Jiang, D. Ma, B. B. Mehta, and M. A. Griswold, "Game of Learning Bloch Equation Simulations for MR Fingerprinting," *In Proc. Joint Annual Meeting of ISMRM-ESMRMB*, 2018.

[34] P. R. Moran, "A flow velocity zeugmatographic interlace for NMR imaging in humans," *Magnetic Resonance Imaging*, vol. 1, 1982.

[35] F. Durst, *Grundlagen der Strömungsmechanik*. Springer, 2006.

[36] S. Schmidt, S. Flassbeck, M. E. Ladd, and S. Schmitter, "On the Influence of Intravoxel Velocity Distributions on the Noise of Phase Contrast Velocimetry," *In Proc. Joint Annual Meeting of ISMRM-ESMRMB*, 2018.

[37] H. Haraldsson, S. Kefayati, S. Ahn, P. Dyverfeldt, J. Lantz, M. Karlsson, G. Laub, T. Ebbers, and D. Saloner, "Assessment of Reynolds stress components and turbulent pressure loss using 4D flow MRI with extended motion encoding," *Magnetic Resonance in Medicine*, vol. 79, no. 4, 2018.

[38] P. Dyverfeldt, A. Sigfridsson, J.-P. E. Kvitting, and T. Ebbers, "Quantification of intravoxel velocity standard deviation and turbulence intensity by generalizing phase-contrast MRI," *Magnetic Resonance in Medicine*, vol. 56, no. 4, 2006.

[39] P. Dyverfeldt, J.-P. E. Kvitting, A. Sigfridsson, J. Engvall, A. F. Bolger, and T. Ebbers, "Assessment of fluctuating velocities in disturbed cardiovascular blood flow: In vivo feasibility of generalized phase-contrast MRI," *Journal of Magnetic Resonance Imaging*, vol. 28, no. 3, 2008.

[40] P. Dyverfeldt, R. Gårdhagen, A. Sigfridsson, M. Karlsson, and T. Ebbers, "On mri turbulence quantification," *Magnetic Resonance Imaging*, vol. 27, no. 7, 2009.

[41] P. Dyverfeldt, A. Sigfridsson, H. Knutsson, and T. Ebbers, "A novel MRI framework for the quantification of any moment of arbitrary velocity distributions," *Magnetic Resonance in Medicine*, vol. 65, no. 3, 2011.

[42] V. L. Yarnykh, "Actual flip-angle imaging in the pulsed steady state: A method for rapid three-dimensional mapping of the transmitted radiofrequency field," *Magnetic Resonance in Medicine*, vol. 57, no. 1, 2007.

[43] S. Gavazzi, C. A. van den Berg, A. Sbrizzi, H. P. Kok, L. J. A. Stalpers, J. J. Lagendijk, H. Crezee, and A. L. H. M. W. van Lier, "Accuracy and precision of electrical permittivity mapping at 3T: the impact of three mapping techniques," *Magnetic Resonance in Medicine*, 2019.

[44] N. J. Pelc, M. A. Bernstein, A. Shimakawa, and G. H. Glover, "Encoding strategies for three-direction phase-contrast MR imaging of flow," *Journal of Magnetic Resonance Imaging*, vol. 1, no. 4, 1991.

[45] J. M. Hollas, *Modern Spectroscopy*. John Wiley & Sons, 2004.

[46] B. Zhao, J. P. Haldar, K. Setsompop, and L. L. Wald, "Optimal experiment design for magnetic resonance fingerprinting," *2016 38th Annual International Conference of the IEEE Engineering in Medicine and Biology Society (EMBC)*, 2016.

[47] J. Assländer, D. Sodickson, R. Lattanzi, and M. Cloos, "Hybrid-State Free Precession for Measuring Magnetic Resonance Relaxation Times," *In Proc. Joint Annual Meeting of ISMRM-ESMRMB*, 2018.

[48] J. I. Hamilton, K. L. Wright, Y. Jiang, L. Hernandez-Garcia, D. Ma, M. Griswold, and N. Seiberlich, "Pulse Sequence Optimization for Improved MRF Scan Efficiency," *In Proc. 23rd Annual Meeting of ISMRM*, 2015.

[49] D. Kara, M. Fan, J. I. Hamilton, N. Seiberlich, M. Griswold, and R. Brown, "Quality Factors for Efficient and Precise MRF Imaging," *In Proc. 25rd Annual Meeting of ISMRM*, 2017.

[50] O. Cohen, M. Sarracanie, B. D. Armstrong, J. L. A. Ackerman, and M. S. Rosen, "Magnetic Resonance Fingerprinting Trajectory Optimization," *In Proc. 22nd Annual Meeting of ISMRM*, 2014.

[51] G. Körzdörfer, Y. Jiang, P. Speier, J. Pang, D. Ma, J. Pfeuffer, B. Hensel, V. Gulani, M. Griswold, and M. Nittka, "Magnetic resonance field fingerprinting," *Magnetic Resonance in Medicine*, vol. 81, no. 4, 2019.

[52] G. Buonincontri and S. J. Sawiak, "Mr fingerprinting with simultaneous b1 estimation," *Magnetic Resonance in Medicine*, vol. 76, no. 4, 2016.

[53] N. R. Zwart and J. G. Pipe, "Multidirectional high-moment encoding in phase contrast MRI," *Magnetic Resonance in Medicine*, vol. 69, no. 6, 2013.

[54] P. Storey, A. A. Thompson, C. L. Carqueville, J. C. Wood, R. A. de Freitas, and C. K. Rigsby, "R2* imaging of transfusional iron burden at 3T and comparison with 1.5T," *Journal of Magnetic Resonance Imaging*, vol. 25, no. 3, pp. 540–547, 2007.

[55] J. Assländer, S. J. Glaser, and J. Hennig, "Pseudo Steady-State Free Precession for MR-Fingerprinting," *Magnetic Resonance in Medicine*, vol. 77, no. 3, pp. 1151–1161, 2017.

[56] T. Amthor, P. Koken, K. Sommer, M. Doneva, and P. Börnert, "Steady-State Magnetic Resonance Fingerprinting," *In Proc. 24th Annual Meeting of ISMRM*, 2016.

[57] S. Schmitter, S. Schnell, K. Uğurbil, M. Markl, and P.-F. Van de Moortele, "Towards high-resolution 4D flow MRI in the human aorta using kt-GRAPPA and B1+ shimming at 7T," *Journal of Magnetic Resonance Imaging*, vol. 44, no. 2, 2016.

[58] C. Santelli, M. Loecher, J. Busch, O. Wieben, T. Schaeffter, and S. Kozerke, "Accelerating 4D flow MRI by exploiting vector field divergence regularization," *Magnetic Resonance in Medicine*, vol. 75, 2016.

[59] V. Mazzoli, L. M. Gottwald, E. S. Peper, M. Froeling, B. F. Coolen, N. Verdonschot, A. M. Sprengers, P. van Ooij, G. J. Strijkers, and A. J. Nederveen, "Accelerated 4D phase contrast MRI in skeletal muscle contraction," *Magnetic Resonance in Medicine*, vol. 80, no. 5, 2018.

[60] G. Pagé, J. Bettoni, A.-V. Salsac, and O. Balédent, "Influence of principal component analysis acceleration factor on velocity measurement in 2D and 4D PC-MRI," *Magnetic Resonance Materials in Physics, Biology and Medicine*, 2018.

[61] R. Jürgen, P. Mazurkewitz, P. Börnert, and T. Nielsen, "Cross Term and Higher Order Gradient Impulse Response Function Characterization using a Phantom-based Measurement," *In Proc. Joint Annual Meeting of ISMRM-ESMRMB*, 2018.

[62] C. Bing, C. Mougenot, R. Staruch, E. Ramsay, A. Schmitt, J. Kortelainen, J. Koskela, and R. Chopra, "The importance of phase drift correction for accurate MR thermometry in long duration MR-HIFU exposures," *Journal of Therapeutic Ultrasound*, vol. 3, 2014.

[63] H. Y. Carr and E. M. Purcell, "Effects of Diffusion on Free Precession in Nuclear Magnetic Resonance Experiments," *Phys. Rev.*, vol. 94, 1954.

List of scientific contributions

Parts of this work appear in the following list of publications:

Journal Publications

S. Flassbeck, S. Schmidt, P. Bachert, M.E. Ladd, S. Schmitter, "Flow MR Fingerprinting.", *Magnetic Resonance in Medicine*, 2018.

Conference Contributions

S. Flassbeck, S. Schmidt, M.E. Ladd, S. Schmitter, "Quantification of Flow by Magnetic Resonance Fingerprinting", *In Proc. 25th Annual Meeting of ISMRM*, 2017.

S. Flassbeck, S. Schmidt, M.E. Ladd, S. Schmitter, "On the Influence of Intra-Voxel Dephasing in FISP-MRF with Variable Repetition Time", *In Proc. 25th Annual Meeting of ISMRM*, 2017.

S. Flassbeck, S. Schmidt, M.E. Ladd, S. Schmitter, "On the Impact of Heart Rate Variability in Flow-MRF", *In Proc. ISMRM MRF-Workshop*, 2017.

S. Flassbeck, S. Schmidt, M.E. Ladd, S. Schmitter, "Optimization of the Flow Encoding Pattern under Consideration of Spatio-Temporal Velocity Gradients in Flow-MR Fingerprinting", *In Proc. Joint Annual Meeting of ISMRM-ESMRMB*, 2018.

S. Flassbeck, S. Schmidt, M.E. Ladd, S. Schmitter, "Flow-MRF: a novel way of quantifying blood velocities in combination with tissue relaxation parameters", *In Proc. 30th Annual International Conference, SMRA*, 2018.

S. Flassbeck, S. Schmidt, M.E. Ladd, S. Schmitter, "Reynolds Stress Tensor Quantification using a Flow-MRF Approach", *In Proc. 26th Annual Meeting of ISMRM*, 2019.

Further contributions are listed below:

Journal Publications

J.M. Lommen, **S. Flassbeck**, N.G.R. Behl, S. Niesporek, P. Bachert, M.E. Ladd, A.M. Nagel, "Probing the microscopic environment of ^{23}Na ions in brain tissue by MRI: On the accuracy of different sampling schemes for the determination of rapid, biexponential math formula decay at low signal-to-noise ratio.", *Magnetic Resonance in Medicine*, 2018.

J. Emmerich, **S. Flassbeck**, S. Schmidt, P. Bachert, M.E. Ladd, S. Straub, "Rapid and accurate dictionary-based T_2 mapping from multi-echo turbo spin echo data at 7 Tesla", *Journal of Magnetic Resonance Imaging*, 2018.

S. Schmidt, **S. Flassbeck**, P. Bachert, M.E. Ladd, S. Schmitter, "Flow encoding gradient waveform designs for standard and multi-spoke RF excitation", *Currently under review.*

Conference Contributions

S. Schmidt, **S. Flassbeck**, M. Breithaupt, M.E. Ladd, S. Schmitter, "On the performance of multi-spoke RF pulses in the presence of laminar flow – a simulation study", *In Proc. ESMRMB Annual Scientific Meeting 2016*, 2016.

P. Schygulla, **S. Flassbeck**, M. Breithaupt, M.E. Ladd, S. Schmitter, "On the Impact of Flow on B1+ Mapping in UHF MRI", *In Proc. ESMRMB Annual Scientific Meeting 2016*, 2016.

M. Breithaupt, **S. Flassbeck**, M.E. Ladd, "On Optimizations of MRF Patterns Based on Generalized MRI Sequence Schemes", *In Proc. 25th Annual Meeting of ISMRM*, 2017.

J.M. Lommen, **S. Flassbeck**, N.G.R. Behl, P. Bachert, M.E. Ladd, A.M. Nagel, "Optimizing the precision and accuracy of sampling schemes for T2* quantification of the fast biexponential decay of sodium MRI", *In Proc. 25th Annual Meeting of ISMRM*, 2017.

S. Schmidt, **S. Flassbeck**, M.E. Ladd, S. Schmitter, "Simultaneous Multi-VENC Imaging", *In Proc. 25th Annual Meeting of ISMRM*, 2017.

S. Schmidt, **S. Flassbeck**, M.E. Ladd, S. Schmitter, "Velocity Encoded and Compensated Multi-Spoke RF Pulses for Flow Quantification at Ultra-High Fields", *In Proc. 25th Annual Meeting of ISMRM*, 2017.

F. Friedrich, **S. Flassbeck**, N.G.R. Behl, P. Bachert, M.E. Ladd, F. Maier, "Self-Adapting Dynamic Temporal Resolution for Optimized Reconstruction of Free-Breathing Radial Real-Time MRI", *In Proc. ESMRMB Annual Scientific Meeting 2017*, 2017.

S. Schmidt, **S. Flassbeck**, M.E. Ladd, S. Schmitter, "On the Point of Gradient Moment Expansion for Multi-Spoke RF Pulses", *In Proc. Joint Annual Meeting of ISMRM-ESMRMB*, 2018.

S. Schmidt, **S. Flassbeck**, M.E. Ladd, S. Schmitter, "On the Influence of Intravoxel Velocity Distributions on the Noise of Phase Contrast Velocimetry", *In Proc. Joint Annual Meeting of ISMRM-ESMRMB*, 2018.

F.J. Kratzer, **S. Flassbeck**, S. Schmidt, A.M. Nagel, P. Bachert, M.E. Ladd, N.G.R. Behl, "Density Adapted Stack of Stars Sequence for ^{2}3Na Imaging at 7T", *Proc. ISMRM X-Nuc. Workshop*, 2018.

F. Friedrich, **S. Flassbeck**, N.G.R. Behl, B.Knowles, P. Bachert, M.E.Ladd, F. Maier, "Selbstadaptierende radiale Echtzeit-MRT mit dynamischer Zeitauflösung für die Bewegungserfassung unter freier Atmung", *In Proc. 21. Jahrestagung der ISMRM-DS*, 2018.

F.J. Kratzer, **S. Flassbeck**, A.M. Nagel, P. Bachert, M.E. Ladd , N.G.R. Behl, "Optimierung einer dichteangepassten Stack-of-Stars-Sequenz zur 23Na Bildgebung bei 7T", *In Proc. 21. Jahrestagung der ISMRM-DS*, 2018.

S. Schmidt, **S. Flassbeck**, M.E. Ladd, S. Schmitter, "Simultaneous Multi-VENC Imaging with Dual-Echo Acquisition", *In Proc. 30th Annual International Conference, SMRA*, 2018.

F.J. Kratzer, **S. Flassbeck**, A.M. Nagel, P. Bachert, M.E. Ladd, N.G.R. Behl, "Density Adapted Stack of Stars Sequence for ^{23}Na using Dictionary Learning Compressed Sensing Reconstruction", *In Proc. 26th Annual Meeting of ISMRM*, 2019.

F.J. Kratzer, **S. Flassbeck**, A.M. Nagel, S. Schmitter, P. Bachert, M.E. Ladd, N.G.R. Behl, "^{23}Na Imaging using VERSE Pulses in a Density Adapted Stack of Stars Sequence at 7T", *In Proc. ISMRM UHF-Workshop*, 2019.

T. Theis, N.G.R. Behl, E.N.K. Cressman, A.M. Nagel, **S. Flassbeck**, A. Kujawa, P. Bachert, M.E. Ladd, and F. Maier, "Quantitative Evaluation of Thermochemical Ablation Injections in Bovine Liver Phantoms using ^{2}3Na MRI", *In Proc. 25th Annual Meeting of ISMRM*, 2017.

C. Wink, G. Ferrazzi1, J.P. Bassenge1, **S. Flassbeck**, S. Schmidt, T. Schaeffter, and S. Schmitter, "4D Flow Imaging with Reduced Field-of-Excitation", *In Proc. Joint Annual Meeting of ISMRM-ESMRMB*, 2018.

F.J. Kratzer, R. Umathum, **S. Flassbeck**, T.M. Fiedler, A K. Bitz, M.E. Ladd, G. Adriany, S. Schmitter, "A Neck Adapted 4-Channel Saddle-Shaped pTx Transceive Coil for Carotid Imaging at 7T", *In Proc. Joint Annual Meeting of ISMRM-ESMRMB*, 2018.

C. Wink, G. Ferrazzi, J.P. Bassenge, **S. Flassbeck**, S. Schmidt, T. Schaeffter, and S. Schmitter, "4D Flow Imaging with Reduced Field-Of-Excitation", *In Proc. 30th Annual International Conference, SMRA*, 2018.

Acknowledgments

An dieser Stelle möchte ich mich bei allen bedanken die mich auf dem Weg zu meiner Promotion unterstützt haben.

Zuerst möchte ich mich herzlich bei Herrn Prof. Dr. Bachert bedanken, dass Sie meine Promotion vor der Fakultät vertreten und meine Arbeit begutachtet haben. Zudem möchte ich mich für die vielen lehrreichen Seminaren und Vorlesung die ich im Laufe meines Studiums bei Ihm absolvieren durfte bedanken. Diese haben mich schlussendlich für die medizinische Physik begeistert.

Prof. Dr. Schad danke ich, dass er das Zweitgutachten übernommen hat.

Des Weitern möchte ich mich bei Herrn Prof. Dr. Ladd bedanken, dass ich meine Doktorarbeit in seiner Abteilung durchführen konnte.

Großer Dank geht an die gesamte 7T-Gruppe die ich jetzt schon lange mein Zuhause nennen darf! Die tolle Atmosphäre, die social events und die Kaffeepausen wäre meine Promotion sehr viel lustiger gemacht.

Mein ganz besonderer Dank geht an Sebastian Schmitter. Ob von Heidelberg oder von Berlin aus, die Betreuung war absolut Spitze! Ohne deine Ideen, Rat und Hilfe würde diese Arbeit nur ein Schatten von dem sein was sie jetzt ist. Zudem ist es immer eine Freude mit dir zusammenzuarbeiten und das was ich von dir gelernt habe wird meine berufliche Laufbahn noch lange prägen.

Ein riesen Dank geht auch an Tanja für das Führen der Kaffeekasse. Das Angebot der Kaffeekasse hat mich durch viele Wochenenden gerettet
Ein Eckpfeiler meiner Promotion ist ganz sicher auch die Kaffeemaschine! Ohne dich, meine liebe Kaffeemaschine, hätte ich die Promotion sicher nicht überstanden.

Ich möchte noch explizit Mathies und Moritz danken. Was ich von euch beiden über MR und die Welt gelernt habe, hat diese Arbeit erst möglich gemacht!

Sebastian N., Fabian und Simon möchte ich speziell für das Korrekturlesen meiner Arbeit danken aber auch für die vielen 7T-Feiern die durch euch viel amüsanter waren.

Simon gilt noch besonderer Dank für die vielen Diskussionen zu Fluss und Flusskodierung. Wenn ich nicht so viel Code und so viele Slides von dir hätte *borgen* dürfen, dann wäre ich nur halb so weit gekommen mit meiner Arbeit.

Bei Jens, Nadine und Ines möchte ich ganz besonders für den regelmäßen sportlichen Ausgleich und die vielen lustigen Abende bedanken. Besser als mit euch kann man eigentlich nach der Arbeit nicht abschalten.
Chris will ich danken dass du ein astreiner Mitbewohner warst. Ich hätte so manches Meeting verpennt wenn du mich nicht gelegentlich geweckt hättest.

Melanie, dir möchte ich danken dass du ein Ort der Freude und guten Laune in meinem Leben bist! Damit hast du mir die Schreibphase viel leichter gemacht.

Letztlich möchte ich meinem Bruder und meinen Eltern danken! Thomas, du bist immer jemand zu dem ich aufschaue, auch wenn ich das früher nicht realisiert habe. Mama & Papa euch habe ich mehr zu verdanken als hier in diese paar Zeilen passt, darum hier nur ein dickes fettes **DANKE**.